Advanced Integrated Silicon Photonic Devices and Circuits for Optical Interconnects

Jinsong Zhang

Department of Electrical & Computer Engineering
McGill University
Montréal, Québec, Canada

May 08, 2024

A thesis submitted to McGill University in partial fulfillment of the requirements of the degree of Doctor of Philosophy.

Abstract

The ever-increasing throughput of global networks has been driving the evolution of optical communication in the past decades. Optical transceivers are the key component in optical communication to transmit and receive data through optical fiber. Silicon photonics leverages its compatibility with the mature process of complementary metal-oxide-semiconductor (CMOS) fabrication to enable low-cost and high-yield mass production, making it a promising platform for optical transceivers.

In this thesis, we cover the design and characterization of advanced silicon photonic devices and circuits for optical interconnects. The thesis can be separated to two parts. In the first part, we demonstrate three designs of passive optical devices that utilize subwavelength gratings (SWG) to improve the devices in various aspects. In the first design, by inserting a SWG slot in the middle of a multimode interference (MMI) coupler to achieve 1310/1550 nm multiplexing, we managed to reduce the length of the device to 37 µm while achieving calculated 1-dB-IL bandwidths of 192 nm and 123 nm at the two target bands. The second design is a broadband all-silicon multi-band transverse-magnetic-pass (TM-pass) polarizer where we carefully utilize different regimes of Bragg gratings for both TE and TM modes. The device achieves 343-nm bandwidth with IL $<$ 0.4 dB and polarization extinction ratio (PER) $>$ 20 dB in simulation. In the third design, a broadband silicon photonic waveguide crossing enabled by SWG lateral cladding is proposed. The device achieves a calculated maximum IL of 0.229 dB and a maximum crosstalk of -35.6 dB over a 415-nm wavelength

range from 1260 nm to 1675 nm, which covers the whole band for optical communication. All three designs are tested experimentally and the results are shown to well match the simulation.

In the second part, we introduce two works about the co-design of silicon photonic circuits and optical communication systems. The first work is the development of two low-complexity digital signal processing (DSP) algorithms to improve the performance of the optical digital subcarrier multiplexing (DSCM) transmission system on a silicon photonic transmitter. In the experiment with 64 GBd 4-bit/s/Hz DSCM signal containing 8 subcarriers through 43.2 km of standard single-mode fiber (SSMF), the two algorithms combined bring a power budget increase of 4.159 dB at the HD-FEC threshold. For the second work, we propose a novel silicon photonic receiver with phase-retrieving capability based on the spectrally efficient silicon asymmetric self-coherent detection (ASCD). In 40-km transmission experiments, a record net electrical spectral efficiency (ESE) of 7.10 bit/s/Hz per wavelength and per polarization is achieved, where a net 208-Gb/s 32QAM transmission is demonstrated using 29.3-GHz electrical bandwidth.

Abrégé

L'augmentation constante du débit des réseaux mondiaux a stimulé l'évolution de la communication optique au cours des dernières décennies. Les émetteurs-récepteurs optiques sont l'élément clé de la communication optique pour transmettre et recevoir des données via la fibre optique. La photonique sur silicium tire parti de sa compatibilité avec le processus mature de fabrication de semi-conducteurs à oxyde métallique complémentaire (CMOS) pour permettre une production de masse à faible coût et à haut rendement, en faisant une plate-forme prometteuse pour les émetteurs-récepteurs optiques.

Dans cette thèse, nous couvrons la conception et la caractérisation de dispositifs photoniques et de circuits en silicium avancés pour les interconnexions optiques. La thèse peut être divisée en deux parties. Dans la première partie, nous présentons trois conceptions de dispositifs optiques passifs qui utilisent des réseaux de sous-longueur d'onde (SWG) pour améliorer les dispositifs dans divers aspects. Dans le premier design, en insérant une fente SWG au milieu d'un coupleur à interférence multimode (MMI) pour obtenir un multiplexage à 1310/1550 nm, nous avons réussi à réduire la longueur du dispositif à 37 µm tout en atteignant des largeurs de bande IL calculées de 1 dB de 192 nm et 123 nm aux deux bandes cibles. La deuxième conception est un polariseur à large bande passante multi-bande entièrement en silicium où nous utilisons soigneusement différents régimes de réseaux de Bragg pour les modes TE et TM. Le dispositif atteint une largeur de bande de 343 nm avec IL $<$ 0,4 dB et un rapport d'extinction de polarisation (PER) $>$ 20

dB en simulation. Dans la troisième conception, un croisement de guides d'ondes photoniques en silicium à large bande passante, rendu possible par un revêtement latéral SWG, est proposé. Le dispositif atteint un IL maximal calculé de 0,229 dB et un diaphonie maximale de -35,6 dB sur une plage de longueurs d'onde de 415 nm de 1260 nm à 1675 nm, couvrant toute la bande pour la communication optique. Les trois conceptions sont testées expérimentalement et les résultats sont montrés pour correspondre bien à la simulation.

Dans la deuxième partie, nous présentons deux travaux sur la co-conception de circuits photoniques en silicium et de systèmes de communication optique. Le premier travail est le développement de deux algorithmes de traitement numérique du signal (DSP) à faible complexité pour améliorer les performances du système de transmission de multiplexage de sous-porteuses numériques optiques (DSCM) sur un émetteur photonique en silicium. Dans l'expérience avec un signal DSCM de 64 GBd et 4 bits/s/Hz contenant 8 sous-porteuses à travers 43,2 km de fibre monomode standard (SSMF), les deux algorithmes combinés apportent une augmentation du budget de puissance de 4,159 dB au seuil HD-FEC. Pour le deuxième travail, nous proposons un nouveau récepteur photonique en silicium avec une capacité de récupération de phase basée sur la détection auto-cohérente asymétrique en silicium (ASCD) spectaculairement efficace. Dans des expériences de transmission sur 40 km, une efficacité spectrale électrique nette (ESE) record de 7,10 bit/s/Hz par longueur d'onde et par polarisation est atteinte, où une transmission 32QAM nette de 208 Gb/s est démontrée en utilisant une largeur de bande électrique de 29,3 GHz.

Acknowledgements

First of all, I would like to express my deepest gratitude to Prof. David V. Plant, my supervisor, for his constant help and support during my Ph.D. program. Dave is so patient with students that he gave me enough time at the start of my Ph.D. to explore the fields and discover what is my true research interest, with necessary guidance but minimum interference. He always treats me and all the other students with kindness, love, and respect, which just make me feel lucky to be a member of this group with such a delightful environment. “It is a privilege to work in this group”, he says to us all the time. The more I work in the lab, the more I understand this statement. Years of accumulation in equipment and skills make Photonics System Group a world-class lab, and I feel honored to be able to contribute to this group. Thank you Dave, for giving me the ticket six years ago to McGill PSG, and I’ll always cherish the time I had here.

I also want to thank the members of my supervisory committee, Prof. Benoit Champagne and Prof. Ioannis Psaromiligkos. They provided high-quality courses that help me build sold background in signal process. During our sessions, they gave me valuable comments and insights from a perspective outside the field of optics. Therefore, I really appreciate their help on the completion of my Ph.D. program.

I would like to thank my mentor and friend, Dr. Luhua Xu, for the guidance he gave me in the first few years. I still remember how unconfident I was when I first joined the group. It was the discussion with Luhua and the instruction he gave me on my first project that helped me get on the right track. Thank you so much, Luhua.

My gratitude also goes to another mentor of mine, Dr. Zhenping Xing. His insights of optical communication and silicon photonics inspire me so much that I decide to learn as much as possible in various aspects of this field, just as he does. Thank you Zhenping for such a positive influence you gave me. I'm also very grateful for the other senior students in our group, Dr. Xueyang Li, Dr. Deng Mao, and Dr. Md Samiul Alam, for all of their patient helping and instructing on all the ideas, simulations, and experiments I have done during my program.

I would like to express my profound gratitude to my colleague, collaborator, but mostly importantly a dear friend, Zixian Wei. He keep surprising and impressing me with his enthusiasm towards academia, excellent academic skills and background, and deep understanding of literatures. I'm very lucky that I get to work with one of the best peer researchers in this area, and I'll never forget your sincere help and constant encouragement to me. I truly believe someday you will climb to the peak of the academic mountains, and I wish you the best of luck in your future endeavors.

I'm so thankful that I have such excellent colleagues in this group. I always had fruitful yet fun conversations with Weijia Li. Yixiang Hu assisted me build complicated and important experimental setup. Dr. Essam berikaa is always willing to help me in every aspect. Prof. Ramon Gutierrez-Castrejon supported so much during the DSCM project that I cannot thank him enough. Dr. Yannick D'Mello carefully read my manuscripts on silicon photonic devices and give the most valuable feedback. Santiago Bernal and Charles St-Arnault make me laugh all the time and their creativity is amazing. I appreciate the good time I have with the newcomers Kaibo Zhang, Benton Qiu, and Aleksandar Nikic, and I wish them success here. I also thank Dr. Rui Li, Dr. Yun Wang, Dr. Meng Xiang, Dr. Maxime Jacques, Kh Arif Shahriar, James Skoric, Codey Nacke, and Adam Helmy for their help through my journey at PSG. Thank you all.

I have also received lots of help and kindness from outside the group. I'd like to express my gratitude to Dr. Hao Sun, Dr. Guowu Zhang and Yuxuan Xie at McGill for those helpful discussion we had. I also thank my collaborators, Stephen Misak, Aaron Wissing, Junqian Liu, and Prof. Clint Schow from UCSB. I'm so grateful to have worked in such a productive and smooth collaboration project, from which I learned a lot.

It would be a lot harder for me to survive this journey without friendships. To Enning Yang, Shichen Li, Guangyi Zhang, Zhonghao Zhao, Shiquan Zhang, Wuyang Zheng, and Xueqing Zhao, I'll always cherish our time spent together in Montreal. Special thanks to my A Cappella group, Yanbin Zhuang, Xinyi Wang, Xi Chen, Liuke Lu, Keyun Li, and Haotian Zhuang for the beautiful chorus we created together. My deepest gratitude goes to my dearest friends, Bangyuan Liu, Weilun Shi, Ningbo Zhu, Zhen Li, Kuangye Lu, Datong Zhou, Hanbo Shao, and Mingyu Zhu, for always standing by my side these years and supporting me through ups and downs. Last but not least, I'd like to thank Yitian Zhang for all the amazing adventures and experiences we share together. Your love and support means the world to me.

I would like to express the most profound appreciation to my family, especially my father Xiaobin Zhang and my mother Wenyuan Jia. They are always there for me when I'm lost, supporting me with love and patience. They taught me to be kind, independent, and passionate in my life. They have and will always be my role models. I'm very lucky because I have the best parents. Thank you for everything.

Associated Publication

The original contributions of the research work presented in this thesis resulted in the following 6 papers [1–6] (5 journal papers and 1 conference paper). The contribution of the coauthors is stated for each paper below. Also, I co-authored 11 journal papers [7–17] and 11 conference papers [18–28] through the collaboration with other members of the photonics systems group at McGill University and researchers in other research groups.

Journal Articles Directly Related to this Thesis

1. **Jinsong Zhang**, Xueyang Li, Yixiang Hu, Md Samiul Alam, David V. Plant, "Spectrally Efficient Integrated Silicon Photonic Phase-Diverse DD Receiver with Near-Ideal Phase Response for C-Band DWDM Transmission," *Laser & Photonics Reviews*, vol. 18, no. 3, 2024.
   I conceived the idea together with Xueyang Li, performed the simulation, generated layouts for fabrication, conducted the experiments, and wrote the paper. The other coauthors contributed in discussing the idea, building the experimental setup, and editing the paper. This work is presented in Chapter 7.

2. **Jinsong Zhang**, Luhua Xu, Deng Mao, Yannick D'Mello, Zixian Wei, Weijia Li, David V. Plant, "Temperature-insensitive and low-loss single-mode silicon waveguide crossing covering all optical communication bands enabled by curved anisotropic metamaterial," *Nanophotonics*, vol. 12, no. 21, pp. 4095-4107, 2023.

I conceived the idea, developed the theory, performed the simulation, generated layouts for fabrication, conducted the experiment, and wrote the paper. The coauthors contributed in discussing the idea and editing the paper. This work is presented in Chapter 5.

3. **Jinsong Zhang**, Essam Berikaa, Ramón Gutiérrez-Castrejón, Md Samiul Alam, Fabio Cavaliere, Stephane Lessard, Zixian Wei, Weijia Li, David V. Plant, "PAPR Reduction and Nonlinearity Mitigation of Optical Digital Subcarrier Multiplexing Systems With a Silicon Photonics Transmitter," *Journal of Lightwave Technology*, vol. 41, no. 22, pp. 6957-6969, 2023.
   I conceived the idea, developed the theory, performed the simulation, conducted the experiment, and wrote the paper. The coauthors contributed in discussing the idea, building the experimental setup, and editing the paper. This work is presented in Chapter 6.

4. **Jinsong Zhang**, Luhua Xu, Deng Mao, Zhenping Xing, Yannick D'Mello, Maxime Jacques, Yun Wang, Stephane Lessard, David V. Plant, "High-extinction-ratio and compact 1310/1550 nm wavelength diplexer on SOI platform based on an SWG-structured two-mode interference coupler," *IEEE Photonics Journal*, vol. 14, no. 2, pp. 1-6, 2022.
   I discussed the idea with Luhua Xu, developed the theory, performed the simulation, generated layouts for fabrication, conducted the experiment, and wrote the paper. The coauthors contributed in instructing me on simulations and experiments, building the experimental setup, and editing the paper. This work is presented in Chapter 3.

5. **Jinsong Zhang**, Luhua Xu, Deng Mao, Yannick D'Mello, Weijia Li, Stephane Lessard, David V. Plant, "All-silicon multi-band TM-pass polarizer on a 220 nm SOI enabled by multiplexing grating regimes," *Optics Express*, vol. 30, no. 1, pp. 326-335, 2022.

I conceived the idea, performed the simulation, generated layouts for fabrication, conducted the experiment, and wrote the paper. The coauthors contributed in discussing the idea, building the experimental setup, and editing the paper. This work is presented in Chapter 4.

Conference Article Directly Related to this Thesis

6. **Jinsong Zhang**, Weijia Li, Zixian Wei, David V. Plant, "Enhanced broadband silicon waveguide crossing based on PSO-processed SWG cladding,", in *IEEE Silicon Photonics Conference,*, 2024.

   I conceived the idea, performed the simulation, and wrote the paper. The coauthors contributed in discussing the idea and editing the paper. This work is not presented in this thesis, but it is an extended work based on Chapter 5.

Journal Articles Not Directly Related to this Thesis

7. Weijia Li, Luhua Xu, Zixian Wei, **Jinsong Zhang**, Deng Mao, Yannick D'Mello, David V. Plant, "Silicon photonic broadband polarization-insensitive switch based on polarization-mode diversity conversion," *Optics Letters*, vol. 48, no. 17, pp. 4661-4664, 2023.

8. Yixiang Hu, Xueyang Li, Deng Mao, Md Samiul Alam, Essam Berikaa, **Jinsong Zhang**, Santiago Bernal, Alireza Samani, Mohammad E Mousa-Pasandi, Maurice O'Sullivan, et al., "Silicon Photonic Phase-diverse Receiver Enabling Transmission of $>$ Net 250 Gbps/λ over 40 km for High-speed and Low-cost Short-Reach Optical Communications," *Journal of Lightwave Technology*, vol. 41, no. 12, pp. 3680 - 3687, 2023.

9. Zixian Wei, **Jinsong Zhang**, Weijia Li, David V. Plant, "Active Learning-aided CNN-based Entropytunable Automatic Modulation Identification for Rate-flexible Coherent

Optical System," *Journal of Lightwave Technology*, vol. 41, no. 14, pp. 4598 - 4608, 2023.

10. Zixian Wei, **Jinsong Zhang**, Weijia Li, David V. Plant, "400-Gbps/80-km rate-flexible PCS-64-QAM WDM-CPON with pseudo-m-QAM chaotic physical layer encryption," *Journal of Lightwave Technology*, vol. 41, no. 8, pp. 2413-2424, IEEE, 2023.

11. Weijia Li, Luhua Xu, **Jinsong Zhang**, Deng Mao, Yannick D'Mello, Zixian Wei, David V. Plant, "Broadband polarization-insensitive thermo-optic switches on a 220-nm silicon-on-insulator platform," *IEEE Photonics Journal*, vol. 14, no. 6, pp. 1-7, 2022.

12. Zixian Wei, **Jinsong Zhang**, Weijia Li, David V. Plant, "Time-variant entropy regulated multiple access for flexible coherent PON," *Optics Letters*, vol. 47, no. 19, pp. 5148-5151, 2022.

13. Deng Mao, Yun Wang, Luhua Xu, **Jinsong Zhang**, Eslam El-Fiky, Md Samiul Alam, Yannick D'Mello, Stephane Lessard, David V. Plant, "CMOS-compatible and temperature insensitive C-band wavelength (de-) multiplexer," *IEEE Photonics Technology Letters*, vol. 34, no. 14, pp. 769-772, 2022.

14. Deng Mao, Yun Wang, Luhua Xu, Eslam El-Fiky, Maxime Jacques, **Jinsong Zhang**, Md Samiul Alam, Amar Kumar, Yannick D'Mello, David V. Plant, "Adiabatic coupler with nonlinearly tapered mode-evolution region," *IEEE Photonics Technology Letters*, vol. 33, no. 16, pp. 840-843, 2021.

15. Xueyang Li, Maurice O'Sullivan, Zhenping Xing, Md Samiul Alam, Thang Hoang, Meng Xiang, Mingyue Zhu, **Jinsong Zhang**, Eslam Elfiky, David V. Plant, "Asymmetric direct detection of orthogonal offset carriers assisted polarization

multiplexed single-sideband signals," *Optics Express*, vol. 28, no. 3, pp. 3226-3236, 2020.

16. Deng Mao, Yun Wang, Eslam El-Fiky, Luhua Xu, Amar Kumar, Maxime Jaques, Alireza Samani, Olivier Carpentier, Santiago Bernal, Md Samiul Alam, **Jinsong Zhang**, et al., "Adiabatic coupler with design-intended splitting ratio," *Journal of Lightwave Technology*, vol. 37, no. 24, pp. 6147-6155, 2019.

17. Luhua Xu, Yun Wang, Deng Mao, **Jinsong Zhang**, Zhenping Xing, Eslam El-Fiky, Md Ghulam Saber, Amar Kumar, Yannick D'Mello, Maxime Jacques, et al., "Ultra-broadband and compact two-mode multiplexer based on subwavelength-grating-slot-assisted adiabatic coupler for the silicon-on-insulator platform," *Journal of Lightwave Technology*, vol. 37, no. 23, pp. 5790-5800, 2019.

Conference Articles Not Directly Related to this Thesis

18. **Jinsong Zhang**, Zixian Wei, Stephen Misak, Aaron Wissing, Junqian Liu, Hector Andrade, Aaron Maharry, Giovanni Gilardi, Ranjeet Kumar, Guan-Lin Su, Ansheng Liu, Yuliya Akulova, James F. Buckwalter, Adel A. M. Saleh, Larry Coldren, Clint L. Schow, and David V. Plant, "First demonstration of 200-G coherent PON at O-band with heterogeneously-integrated SiP Tx and Rx with lasers," in *Optical Fiber Communication Conference*, post-deadline paper, 2024.

19. Stephen Misak, Aaron Wissing, **Jinsong Zhang**, Zixian Wei, Junqian Liu, Hector Andrade, Aaron Maharry, Giovanni Gilardi, Ranjeet Kumar, Guan-Lin Su, Ansheng Liu, Yuliya Akulova, James F. Buckwalter, Adel A. M. Saleh, Larry Coldren, David V. Plant, and Clint L. Schow, "400 Gbps/λ DP-16QAM O-band link with SiP TX and RX PICs using only heterogeneously integrated lasers and SOAs for optical gain," in *Optical Fiber Communication Conference*, post-deadline paper, 2024.

20. Charles St-Arnault, Santiago Bernal, Essam Berikaa, Zixian Wei, Ramon Gutierrez-Castrejon, **Jinsong Zhang**, Md Samiul Alam, Aleksandar Nikic, Benjamin Krueger, Fabio Pittala, and David V. Plant, "Net 1.6 Tbps (4x400Gbps/λ) O-Band IM/DD transmission over 2 km using uncooled DFB lasers on the LAN-WDM grid and sub-1V drive TFLN modulators," in *Optical Fiber Communication Conference*, post-deadline paper, 2024.

21. Yixiang Hu, Mohammad E. Mousa-Pasandi, Ramon Gutiérrez-Castrejón, Maurice O'Sullivan, Fanqi Kong, Brandon Buscaino, **Jinsong Zhang**, Santiago Bernal, Charles St-Arnault, and David V. Plant, "Digital Vibration Detection and Localization using Carrier Laser Phase Noise Retrieval in a Conventional Coherent Transponder," in *Optical Fiber Communication Conference*, 2024.

22. Luhua Xu, Weijia Li, **Jinsong Zhang**, Deng Mao, Md Samiul Alam, Yannick D'Mello, Santiago Bernal, Zixian Wei, David V. Plant, "Broadband High-Performance 2×2 MMI 3-dB Coupler Enabled by SWG Lateral Cladding for the Silicon-on-Insulator Platform," in *Optical Fiber Communications Conference*, 2023.

23. Zixian Wei, **Jinsong Zhang**, Weijia Li, David V. Plant, "TDMA Frame Design and Demonstration of Encrypted Coherent Fronthaul with Flexible and Monitored Rate," in *CLEO: Science and Innovations*, 2023.

24. Weijia Li, Luhua Xu, Zixian Wei, **Jinsong Zhang**, Deng Mao, Yannick D'Mello, David V. Plant, "2×2 Broadband Thermo-optic Polarization-insensitive Switch on the SOI Platform," in *CLEO: Science and Innovations*, 2023.

25. Yixiang Hu, Xueyang Li, Deng Mao, Md Samiul Alam, Essam Berikaa, **Jinsong Zhang**, Alireza Samani, Mohammad E Mousa-Pasandi, Maurice O'Sullivan, Charles Laperle, et al., "Transmission of net 200 Gbps/λ over 40 km of SSMF using an

integrated SiP phase-diverse receiver," in *European Conference and Exhibition on Optical Communication*, 2022.

26. Luhua Xu, Deng Mao, **Jinsong Zhang**, Yun Wang, Zhenping Xing, Md Samiul Alam, Maxime Jacques, Yannick D'Mello, Santiago Bernal, David V. Plant, "Broadband polarization beam splitters based on MMI couplers with internal photonic crystals fabricated using 193 nm photolithography," in *Optical Fiber Communications Conference and Exhibition*, 2021.

27. Deng Mao, Yun Wang, Luhua Xu, Eslam El-Fiky, Maxime Jacques, **Jinsong Zhang**, Yannick D'Mello, Stephane Lessard, David V. Plant, "Nonlinearly tapered 3-dB adiabatic coupler," in *IEEE Photonics Conference*, 2020.

28. Luhua Xu, Yun Wang, Deng Mao, **Jinsong Zhang**, Md Samiul Alam, Zhenping Xing, Maxime Jacques, Yannick D'Mello, Santiago Bernal, Stephane Lessard, et al., "Broadband 2×2 adiabatic 3-dB coupler with inversely-tapered mode-evolution region for the silicon-on-insulator platform," in *IEEE Photonics Conference*, 2020.

Contents

List of Figures

List of Tables

List of Acronyms

ADC	analog-to-digital converter.
AMF	Advanced Micro Foundry.
ASCD	asymmetric self-coherent detection.
ASE	amplified spontaneous emission.
AWG	arbitrary waveform generator.
AWGN	additive white Gaussian noise.
B2B	back-to-back.
BER	bit error rate.
BOX	buried oxide.
BPD	balanced photodetector.
BPSK	binary phase-shift keying.
BW	bandwidth.
CADD	carrier-assisted direct detection.
CD	chromatic dispersion.
CDC	chromatic dispersion compensation.
CMOS	complementary metal oxide semiconductor.
CSPR	carrier-to-signal power ratio.
CT	crosstalk.
CW	continuous-wave.

DAC	digital-to-analog converter.
DC	directional coupler.
DD	direct detection.
DD-LMS	decision-directed least mean square.
DFT	discrete Fourier transform.
DSB	double sideband.
DSCM	digital subcarrier multiplexing.
DSP	digital signal processing.
DUT	device-under-test.
DWDM	dense wavelength-division multiplexing.
E/O	electrical to optical.
ECL	external cavity laser.
EDFA	erbium-doped fiber amplifier.
EEPN	equalization enhanced phase noise.
ER	extinction ratio.
ESE	electrical spectral efficiency.
FAU	fiber array unit.
FDE	finite-difference eigenmode.
FDTD	finite-difference time-domain.
FEC	forward error correction.
FFT	fast Fourier transform.
FIR	finite impulse response.
FO	frequency offset.
FOC	frequency offset compensation.
FOM	figure of merit.
FSR	free spectral range.

FWM	four-wave mixing.
GC	grating coupler.
HD-FEC	hard-decision forward error correction.
I/O	input and output.
IDFT	inverse discrete Fourier transform.
IL	insertion loss.
IM/DD	intensity-modulation-direct-detection.
InP	Indium Phosphide.
IQ	in-phase and quadrature.
ISI	intersymbol interference.
ITU	International Telecommunication Union.
LIDAR	light detection and ranging.
LO	local oscillator.
LPF	low-pass filter.
LUT	look-up table.
MIMO	multiple-input-multiple-output.
MMI	multimode interference.
MPW	multi-project wafer.
MZI	Mach-Zehnder interferometer.
MZM	Mach-Zehnder modulator.
NGDC	narrow-gap direction coupler.
NIR	near infrared.
O/E	optical to electrical.
OFDM	orthogonal frequency-division multiplexing.
OSA	optical spectrum analyzer.
OSNR	optical signal-to-noise ratio.

P/S parallel to serial.

PAM pulse amplitude modulation.

PAPR peak-to-average power ratio.

PBS polarization beam splitter.

PC polarization controller.

PCS probabilistic constellation shaping.

PD photodetector.

PDK process design kit.

PER polarization extinction ratio.

PIC photonic integrated circuit.

PMD polarization mode dispersion.

PMF probability mass function.

PRBS pseudorandom binary sequence.

PSO particle swarm optimization.

PSR polarization splitter and rotator.

QAM quadrature amplitude modulation.

RF radio frequency.

ROP received optical power.

RRC root raised cosine.

RTO real-time oscilloscope.

S/P serial to parallel.

SCD self-coherent detection.

SD-FEC soft-decision forward error correction.

SEM scanning electron microscope.

SNR signal-to-noise ratio.

SOI silicon-on-insulator.

SOP state of polarization.

SPM self-phase modulation.

SPP series-push-pull.

SSB single sideband.

SSBI signal-signal beating interference.

SSMF standard single-mode fiber.

SWG subwavelength grating.

TDCM tunable dispersion compensation module.

TE transverse electric.

TM transverse magnetic.

TMI two-mode interference.

TWMZM traveling-wave Mach-Zehnder modulator.

VOA variable optical attenuator.

WDM wavelength-division multiplexing.

XPM cross-phase modulation.

ZGDC zero-gap direction coupler.

Chapter 1

Introduction

1.1 Motivation

The past decade has witnessed the rapid growth of the Internet industry and consequently, the requirement for communication capacity has gone up fast. According to the 2021 annual report of DE-CIX [32], one of the largest Internet exchange points in the world, its global connected capacity increased by more than 30% to 96.2 terabits, while the total data throughput grew about 20% to 38 exabytes in 2021. With optical transmission systems being the backbone infrastructure of modern telecommunication networks, the capacity of optical transceivers has been evolving exponentially. According to the Cisco white paper titled 'Open Optical Network' in November 2022 [29], the data rate of a single high-speed coherent optical module has increased from 100G in 2012 to 400G in 2017, and then to 800G in 2020.

However, with the ever-growing speed comes the issue of cost. A larger capacity requires more power to process the data. Furthermore, high-bandwidth optical modulators utilizing materials such as indium phosphide are not suitable for mass production, therefore raising the cost. That is the reason why silicon photonics has captured the

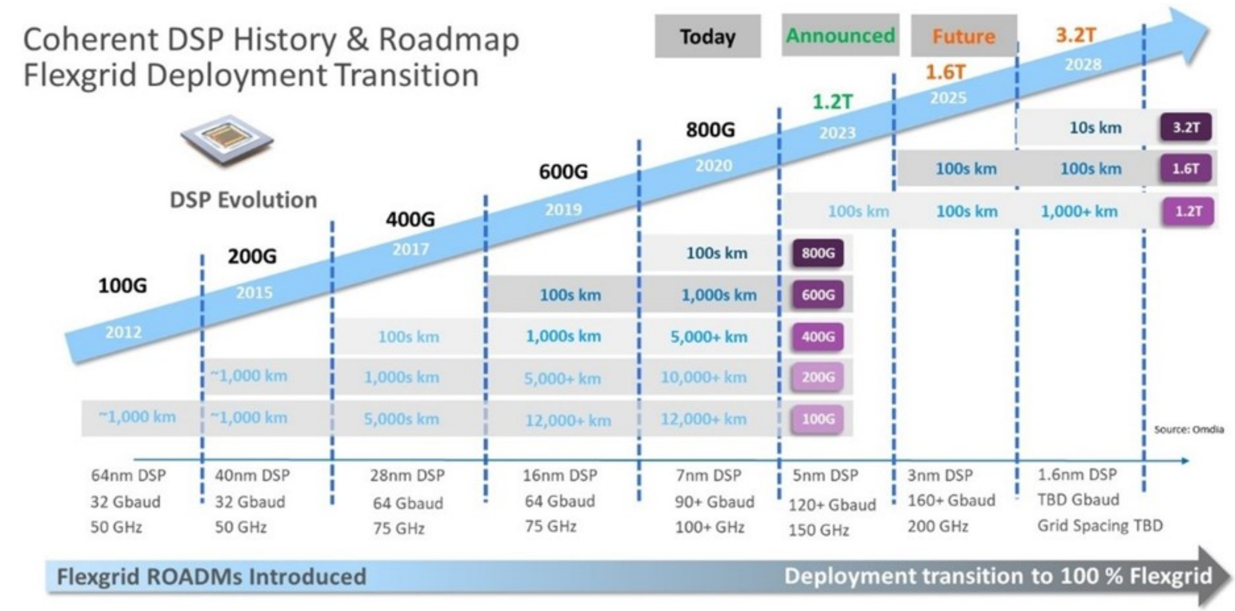

Figure 1.1: The development and roadmap of the coherent optical transceiver from 2012 to 2028. [29]

attention of both academia and industry. Due to the compatibility between silicon photonics technology and the well-developed complementary metal-oxide-semiconductor (CMOS) fabrication process, the cost can be brought down, while high-speed silicon-based electro-optic components such as modulators and photodetectors make it possible to produce large-capacity optical transceivers for next-generation networks.

An integrated photonics transceiver generally consists of the electronic part and the photonic part and the photonics mainly includes active and passive components. For silicon-based transceivers, the photonics part is usually a photonic integrated circuit (PIC) based on the silicon-on-insulator (SOI) platform. As shown in Fig. 1.2, after the signal is generated and amplified, it is applied on the modulator that transfers the signal to the optics domain. After the transmission, the signal is captured by the receiver, where the photodiode translates the optical signal to the electrical domain and sends it to the electronic circuit. The circuit then processes the data and extracts the transmitted

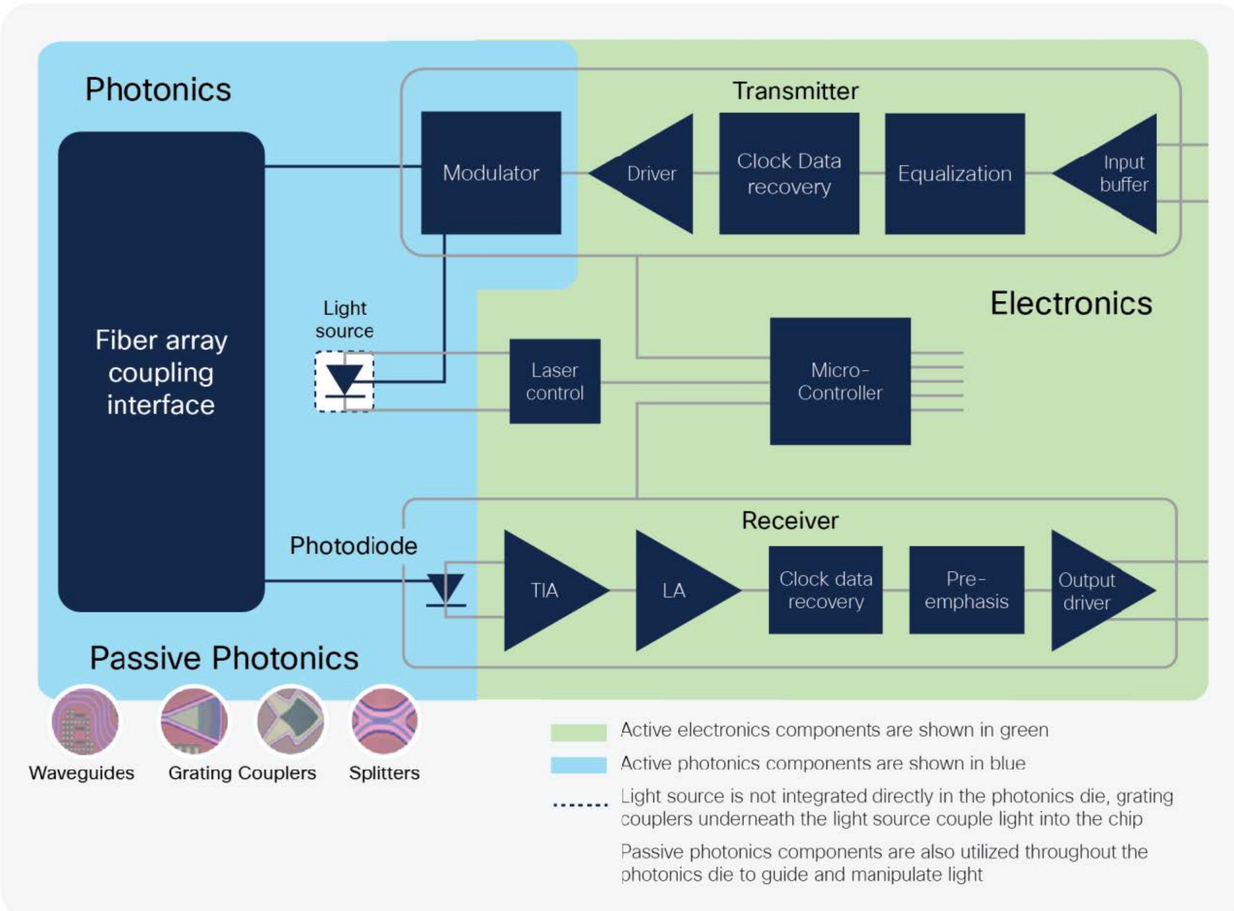

Figure 1.2: Schematic of a silicon photonics transceiver. [30]

information, completing the communication process. Besides these active devices (modulators and photodiodes) acting as the interface between the electronics and the photonics, the passive devices are also key components of the silicon photonics circuits. Integrated optical waveguides are used to route the optical signal, wavelength multiplexers and demultiplexers are applied to achieve wavelength-division multiplexing (WDM) communication system, whilst devices such as polarization beam splitter (PBS), polarization splitter and rotator (PSR), polarizers are employed to manipulate the state of polarization (SOP) of the on-chip light.

Although silicon photonic transceivers are already prototyped and commercialized in the industry, there exists a constant motivation to develop circuits with higher performance. Specifically, we desire passive devices with lower loss, lower crosstalk, smaller footprint, and broader operation bandwidth. For active devices and transceiver circuits, our targets are higher speed, lower power consumption, and simplicity. In this thesis, we propose various solutions within the scale of devices, circuits, and systems to address these challenges for silicon photonic transceivers.

1.2 Organization of the thesis

In this thesis, various silicon photonic devices and circuits are proposed to overcome the issues and improve silicon photonic transceivers from different perspectives. After a background introduction about silicon photonic transceivers in Chapter 2, Chapters 3,4,5 will introduce three passive silicon photonic devices, and the following Chapters 6 and 7 will be about advanced circuits and systems designs on silicon.

Specifically, Chapter 3 illustrates a high-performance 1310/1550 nm wavelength diplexer based on subwavelength grating (SWG) that is proposed to minimize the device length and improve performance. In Chapter 4, a multi-band transverse magnetic (TM) polarizer based on multiplexing the regimes of Bragg gratings is introduced. Chapter 5 is about an ultra-broadband waveguide crossing that covers all the optical communication bands. The broadband feature of the waveguide crossing is enabled by a novel curved SWG. Chapter 6 demonstrates two simple yet effective transmitter DSP algorithms targeting at digital subcarrier multiplexing (DSCM) systems to mitigate its performance degradation on a silicon photonics transmitter. Chapter 7 is about the design of a silicon-based simplified coherent transceiver, in which the transmission performance is dependent on the design of a key integrated passive device. Finally, we conclude the thesis in Chapter 8.

1.3 Contributions to Original Knowledge

The original contribution of this thesis is summarized in this section.

High-performance silicon 1310/1550 nm wavelength diplexer

- We propose the first experimental demonstration of a compact 1310/1550 nm wavelength diplexer based on a two-mode interference (TMI) coupler. We thoroughly analyzed the working principle of the proposed device. We discovered that the insertion of SWG slot into an MMI enables us to tune the beat length ratio between the two target wavelengths through index engineering, which reduces the device length. With TM mode, the device achieves the ideal beat length ratio of 2:1 between 1310/1550 nm, whilst the best ratio shown in previous literature is 3:2.

- We discover that the taper design from the single-mode waveguide to the multimode waveguide is key in this structure. A wide access port to the coupling region avoids the excitation of high-order modes, fundamentally changing the scheme of mode interference from multi-mode to two-mode. This further reduces the length of the device to 37 µm.

- Simulation results show that the calculated 1-dB-IL bandwidths are 192/123 nm at O/C-bands, which satisfies the ITU standard. The 192-nm bandwidth at O-band is also a record among existing literature. As for ER, the calculated ERs at 1310 nm and 1550 nm reach 28.05 and 42.54 dB. In experiments, we show that the measured 15-dB-ER bandwidths of 82 nm and 56 nm are accomplished in the O-band and the C-band, respectively, and the ER reaches 19.58 dB at $\lambda = 1310$ nm and 26.56 dB at $\lambda = 1550$ nm.

- We analyze the tolerance of our proposed design to fabrication errors. We prove that the proposed structure is insensitive to the changes of the SWG fill factor, which eases the requirement for the fabrication process.

Broadband all-silicon photonics TM-pass polarizer on 220 nm SOI

- We propose an all-silicon multi-band TM-pass polarizer based on one-dimensional gratings. The device is designed on 220 nm SOI with a careful selection of parameters, the grating operates under the subwavelength regime over all the optical telecommunication bands for TM mode, while it works as a Bragg reflector for TE mode over S-, C- and L- bands. Furthermore, we discover that the O-band TE-polarized light will diffract if taper gratings are inserted between the strip waveguide and the center grating. Hence, a tapered structure is employed to multiplex the various regimes and consequently extend the operation wavelength range.

- We characterize our design by both simulation and experiments. We show that our proposed device achieves IL < 0.4 dB and PER > 20 dB over a 343 nm band in total in simulation. Measured spectra of the fabricated device also exhibit IL < 1.6 dB and PER > 20 dB over the ranges [1265 nm, 1360 nm] and [1500 nm, 1617 nm], which cover most measurable wavelengths.

Silicon waveguide crossing covering all optical communication bands

- We propose two designs of ultra-broadband single-mode waveguide crossing, namely the initial design and the improved design. In the initial, we propose for the first time, to add straight SWG structures as lateral cladding of the waveguides near the intersection area of the crossing. We analyze theoretically that such a design reduces the index contrast of the waveguide profile, thus weakening the diffraction when it meets the other perpendicular waveguide.

- We find that the performance of the initial design is limited by an unavoidable 45° interface. Hence, we propose the improve design where we replace the straight SWG cladding by ring-shaped curved SWG cladding. We show that this modification helps improve the overall performance of the crossing.

- We develop a 3-step optimization process for the improved design. Firstly, particle swarm optimization (PSO) is conducted to quickly converge to a decent starting set of parameters. Then we conduct 3D parametric sweep with finer simulation to optimize the key parameters. The first and the second step aims at finding the geometry that has the lowest IL. Lastly, we select a number of best parameter sets and use other criteria such as crosstalk and reflection to finalize the parameters. By this methodology, the optimized crossing demonstrates a calculated maximum IL of 0.229 dB and maximum crosstalk of -35.6 dB from 1260 nm to 1675 nm, which covers all the optical communication bands.

- We characterize the fabricated device with measurement. A maximum IL of 0.264 dB and maximum crosstalk of -30.9 dB is achieved within the measurable 230-nm wavelength range that includes O-, C-, and L-bands.

- We analyze the tolerance of our proposed device to fabrication errors and temperature fluctuations. Since such designs do not involve multi-mode interference or coupling, which makes the device insensitive to temperature changes. We prove that our design has a low temperature sensitivity with both simulations and experiments.

Transmitter DSP for optical DSCM transmission on a silicon photonic modulator

- We propose and demonstrate analytically, in simulations, and in experiments the effectiveness of two transmitter DSP techniques that are simple to implement. The first one, never used before in the context of DSCM systems, is an encoding process based on a discrete Fourier transform (DFT) using the symbols in all subcarriers.

Since DFT is usually implemented by fast Fourier transform (FFT), this technique is named FFT encoding. Such encoding is designed to reduce the peak-to-average power ratio (PAPR) of the DSCM system and improve the tolerance to link loss. The second algorithm is a nonlinear signal pre-mapping method, which effectively reduces the effect of the transmitter nonlinearity.

- We first develop the theory of both algorithms and then test them in a simulated coherent transmission system. Moreover, the DSP blocks are evaluated in C-band transmission experiments using a silicon photonic in-phase/quadrature (IQ) modulator. Transmitting a 64 GBd 4-bit/s/Hz DSCM signal composed of 8 subcarriers over a 43.2-km fiber link, applying both the FFT encoding and the nonlinear pre-mapping provides a gain of 4.159 dB in terms of link loss, compared to the raw DSCM system without the proposed DSP blocks. This demonstrates the advantage of employing the proposed algorithms despite introducing minimum computational overhead. Moreover, a gain enhancement effect of the two proposed methods is also observed. The gains provided by each algorithm alone, are 3.458 dB from the FFT encoding and 0.486 dB from the nonlinear pre-mapping. The addition of these two values is lower than the combined gain of 4.159 dB.

- For a fair comparison, we also consider and analyze the case where the capacity of raw DSCM system is improved by manual bit-loading. We price that even compared with the bit-loaded system, the two proposed DSP blocks acting together still outperform by a gain of 1.919 dB.

Silicon photonic asymmetric self-coherent recevier

- We propose an integrated silicon photonics phase-diverse direction detection (DD) receiver with >200G net capacity. The receiver is based on non-interferometric asymmetric self-coherent detection (ASCD), and an integrated racetrack resonator is designed as the optical filter. With the co-optimization of the resonator and the carrier frequency, a nearly-ideal phase response is produced to minimize the performance penalty and improve the electrical spectral efficiency (ESE).

- The circuit is fabricated. We test the circuit in a carrier-assisted double sideband (DSB) transmission system through 40 km of standard single-mode fiber (SSMF). As a result, our proposed receiver shows a record net ESE of 7.10 bit/s/Hz in a net 208-Gb/s 32QAM transmission using 25% soft-decision forward-error-correction (SD-FEC) with a 4e-2 pre-FEC bit-error-rate (BER) threshold.

- We prove that the racetrack resonator provides periodicity in the response, which enables the receiver to operate in dense wavelength-division multiplexing (DWDM) communication systems. In experiments, we show that the prototype receiver circuit supports net 220-Gb/s/λ 16QAM transmissions over 14 channels with 205-GHz grids from 1527 nm to 1550 nm, using a general 20% SD-FEC with a 2e-2 pre-FEC BER threshold. The maximum capacity reaches net 240 Gb/s at one of the best channels. Note that in this experiment, we only apply standard coherent DSP including all-linear equalization, which further reduces the complexity since no extra DSP is needed. Our prototype is shown to be a cost-effective solution to high-speed datacenter optical interconnection.

Chapter 2

Background

2.1 An overview of the silicon photonic platform

The basic motivation of silicon photonics is to leverage the advantages of CMOS fabrication. The CMOS process has been well-developed in the semiconductor industry to achieve low cost, high robustness, and high yield. Therefore the fabrication of integrated photonic devices and circuits on the silicon platform becomes cost-effective and does not require further significant investment on infrastructure.

The functions of silicon photonics include the routing, processing, modulation, and detection of the light with integrated devices, according to Fig. 2.1. In Fig. 2.2, we show the specific processes of integrated devices on the SOI platform by Advanced Micro Foundry (AMF) as an example. The platform is based on a silicon substrate and the buried oxide (BOX) layer on top of the substrate. The silicon layer on the BOX layer is the main layer to form waveguides and couplers. Due to the high refractive index contrast between silicon and silicon oxide, the devices on the SOI platform are generally compact. There is a layer for metal deposition for thermal-optic phase shifters. For electro-optic modulators, the process applies P-type and N-type doping in the silicon. As for the photodetectors (PD), other materials can be integrated on silicon such as Germanium, targeting the detection of wavelengths in the near-infrared (NIR) range.

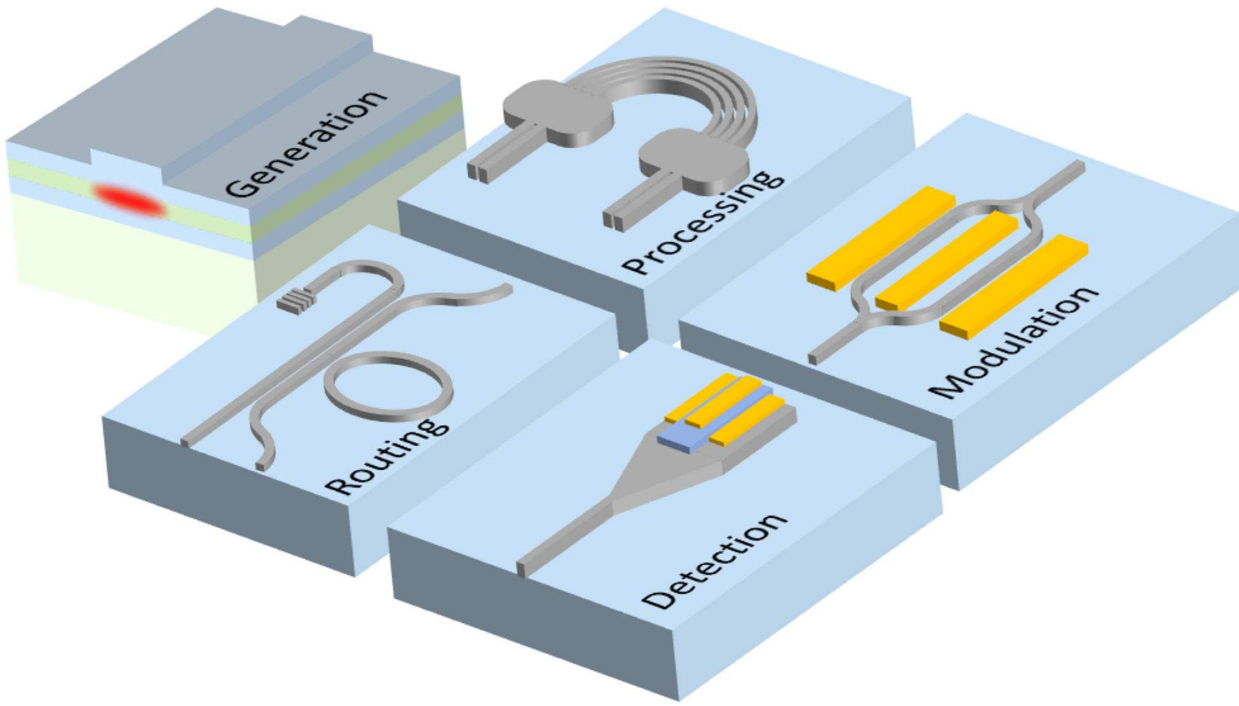

Figure 2.1: Typical components and functions of the silicon photonic platform. [31]

Silicon photonic devices and circuits can be utilized for multiple applications, including but not limited to communication [33], sensing [34], LIDAR [35], gyroscope [36] In this paper, we focus on one of the most important end uses: optical communication, which leads us to the concept of silicon photonic transceiver.

A silicon photonic transceiver is a product of multidisciplinary engineering that involves different levels of design. Therefore, the background section will be split into 3 parts. The first part addresses the basic passive components of silicon photonics that are purely optical. The second part introduces the active devices that conduct the optical-to-electrical (O/E) and electrical-to-optical (E/O) conversion on the silicon platform. Transceiver circuit designs based on those active devices are also mentioned. The third part covers the schematics of

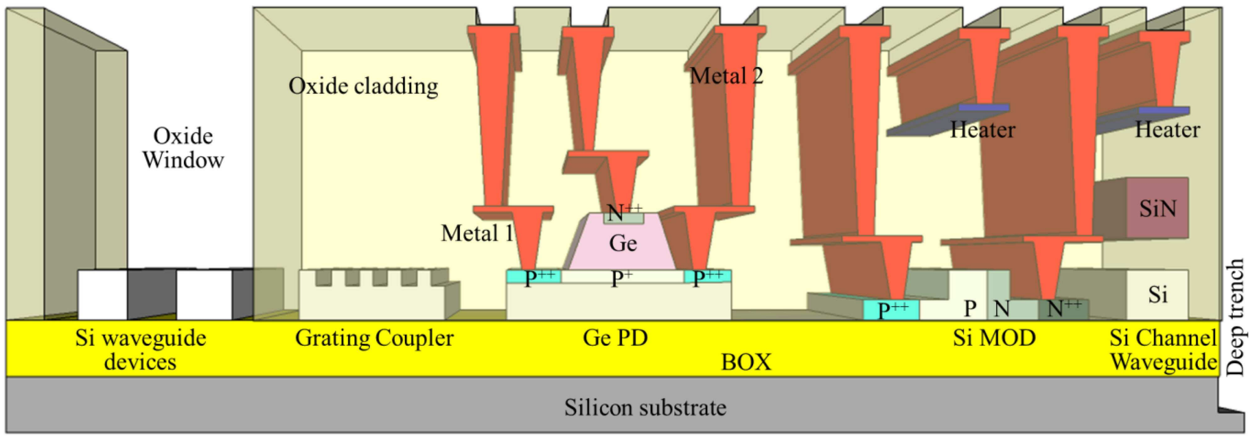

Figure 2.2: Cross-sectional process overview of the multi-project wafer (MPW) of AMF, including different types of silicon photonic structures and devices. [31]

silicon-based optical transceiver circuits.

2.2 Passive silicon photonic structures and devices

2.2.1 Waveguides

Waveguides are an essential component of integrated photonics platforms. In silicon photonics, the sizes of the waveguide cross-section are within the nanometer scale due to the high index contrast between silicon and the BOX layer. At ~1550 nm, the refractive index of silicon is 3.476 [37], and the index of the oxide layer is 1.444 [38].

We calculate the mode profiles for a typical SOI single-mode strip waveguide for C-band (1530 - 1565 nm) operation, with a width of 500 nm and a height of 220 nm. We use the finite-difference eigenmode (FDE) mode of the Ansys Lumerical simulation suite.

According to Fig. 2.3 and 2.4, the strip waveguide supports two orthogonal modes: the quasi-TE and quasi-TM modes. For simplicity, we denote them as the TE mode and TM mode. The electrical field of the quasi-TE mode is mainly distributed inside the waveguide region. For the quasi-TM mode, the electrical field is distributed more in the outside cladding

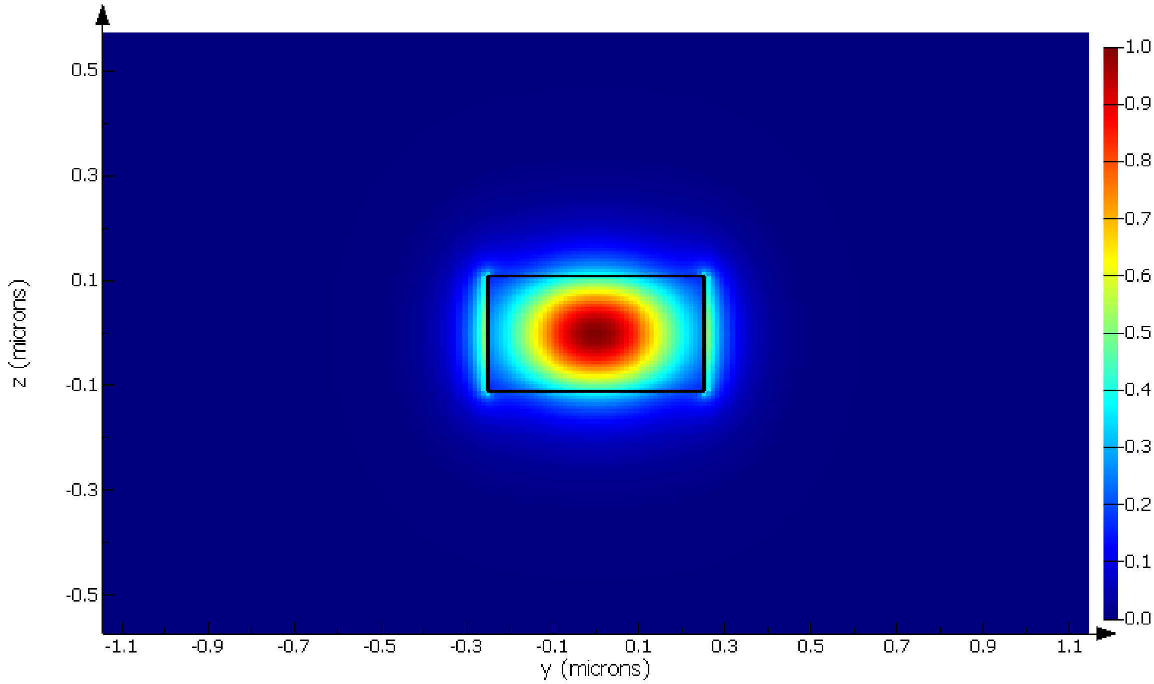

Figure 2.3: Electric field intensity distribution of the fundamental TE mode in a 500 nm * 220 nm SOI waveguide at the wavelength of 1550 nm.

surrounding the boundaries of the index profile.

The simulation for an ideal waveguide profile cannot reflect the real loss of the waveguide, since the main source of loss for fabricated waveguides is side-wall roughness. Currently, the typical propagation loss of a standard 500 nm * 220 nm rib SOI waveguide can reach 1.4 dB/cm [31], low enough for millimeter-scale on-chip routing.

2.2.2 Couplers

Directional Coupler

Directional couplers (DC) are one of the basic passive components in integrated photonic platforms. A conventional silicon photonic symmetric DC consists of two parallel waveguides

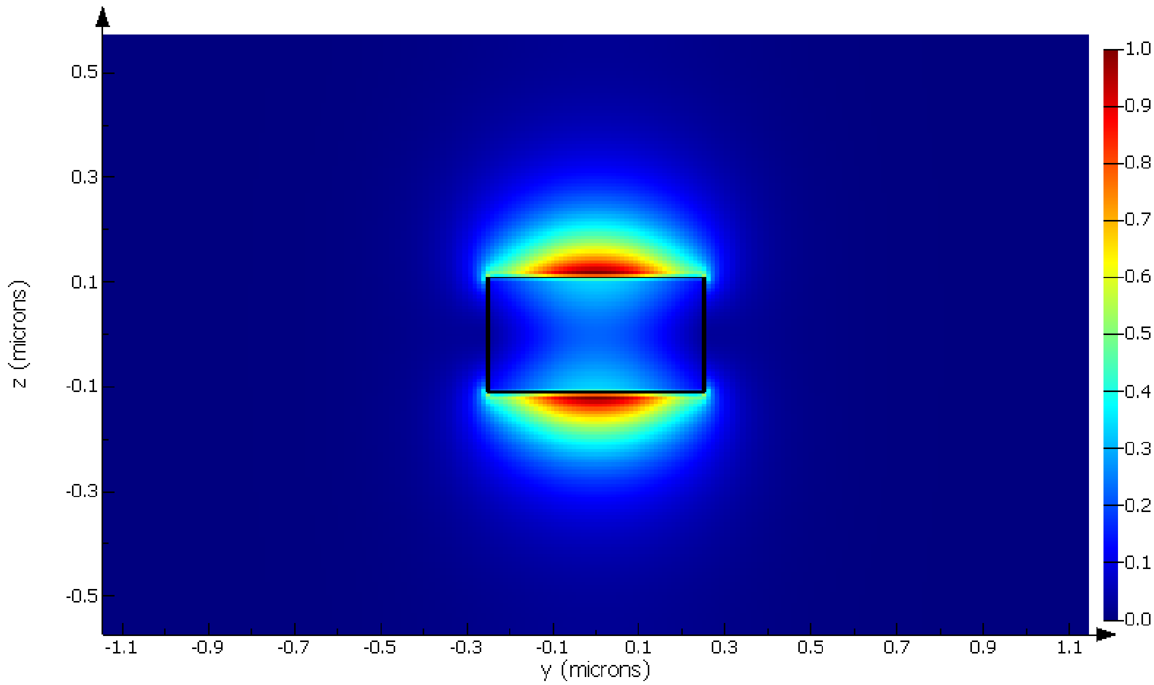

Figure 2.4: Electric field intensity distribution of the fundamental TM mode in a 500 nm * 220 nm SOI waveguide at the wavelength of 1550 nm.

placed close enough to each other. The optical power can then be coupled between the two adjacent waveguides due to the evanescent waves of the waveguide modes outside the silicon core as shown in Fig. 2.3 and 2.4.

An example device schematic is shown in Fig. 2.5. In Fig. 2.6, we simulate the light propagation of TE and TM modes in a DC with a waveguide width of $W_{\mathrm{wg}} = 500$ nm and a waveguide gap of $G = 180$ nm, using 2.5-dimensional (2.5D) finite-difference time-domain (FDTD) simulation. At different positions along the direction of light propagation, the power ratio between the two waveguides varies. That enables the DC to function as a power splitter. Comparing the propagation of TE and TM modes in Fig. 2.6 (a) and (b), we see that the coupling lengths of the two modes are different. Therefore, DC can also be utilized to achieve polarization handling devices on silicon such as PBS [39–41] and polarizers [42].

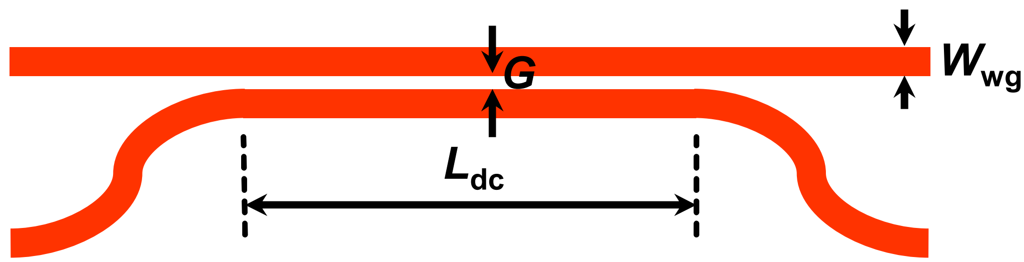

Figure 2.5: Schematic of an integrated directional coupler.

The principle of DC can be explained from another perspective. If we calculate the supported TE modes of the two waveguides together in the coupling region of DC, we will get two mode profiles, namely the even and the odd modes. These modes are denoted as super-modes. In the super-mode theory, the light excites the two super-modes when entering the coupling region. Since the two modes have different effective indexes and propagation constants, their superposed mode distribution varies along the propagation, thus reflecting different power-splitting ratios. Under this theory, we can calculate the beat length of DC with $L_\pi = \lambda/2/(n_{\text{eff0}} - n_{\text{eff1}})$, where n_{eff0} and n_{eff1} are the effective indexes of two super-modes. If the coupling length equals the beat length, the light will be completely coupled to the other waveguide.

MMI Coupler - from two modes to multiple modes

A limitation of DC is that the device is a 2-input-2-output device at most. Therefore in this section, we introduce another type of coupler, the MMI coupler that enables multi-port operation.

MMI stands for multimode interference. In an MMI coupler, the light in a single-mode waveguide is guided to a much wider waveguide that supports multiple modes under the same polarization. The key principle of the MMI is the self-imaging principle [43], which

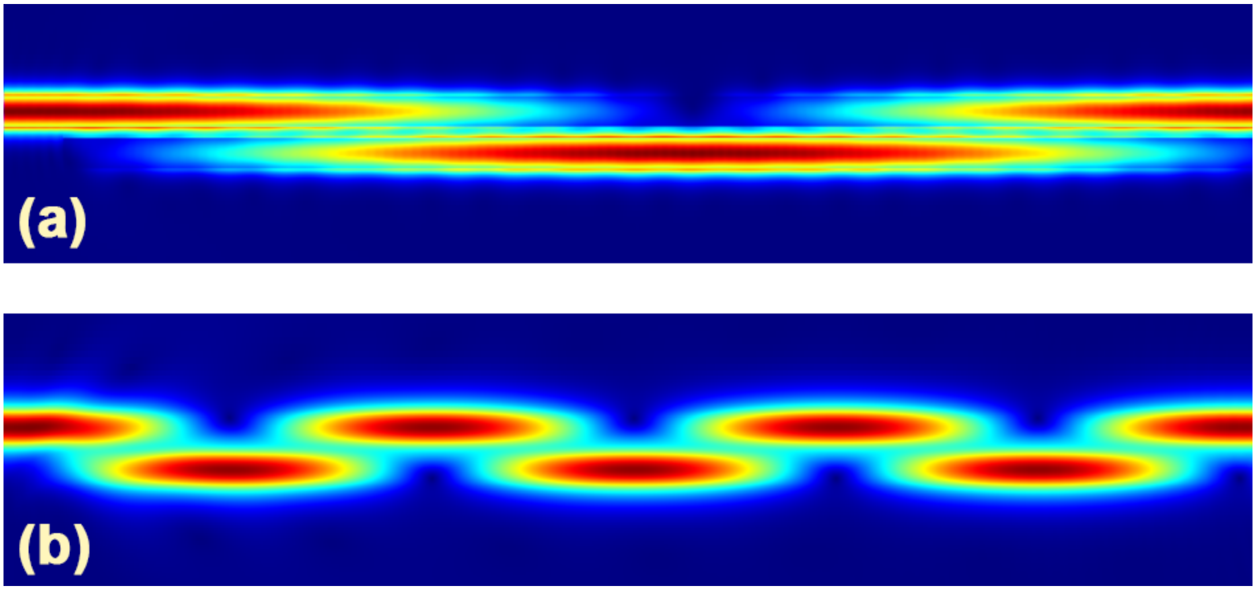

Figure 2.6: Electric field intensity distribution of light propagation in a DC. (a) TE mode. (b) TM mode.

reveals that the input field profile can be reproduced in single or multiple images along the propagation direction in a multimode waveguide. Therefore the MMI naturally functions as a multi-port power splitter. The minimum length of the multimode region for a general-interference MMI to achieve 1*N power splitting is calculated as [43]:

$$L_{\mathrm{mmi}} = \frac{3L_\pi}{N}, \tag{2.1}$$

where the beat length is defined by $L_\pi = \lambda/2/(n_{\mathrm{eff0}} - n_{\mathrm{eff1}})$, but unlike DC, here the n_{eff0} and n_{eff1} denote the effective indexes of the fundamental and first-order mode in the multimode region.

General-interference MMI does not limit the location of the input port. Nevertheless, there exist other mechanisms of interference that reduce the coupling length of self-imaging but restrict the number and the locations of the input waveguides. For example, locating only one input port at the center will induce symmetric interference, where the length of a

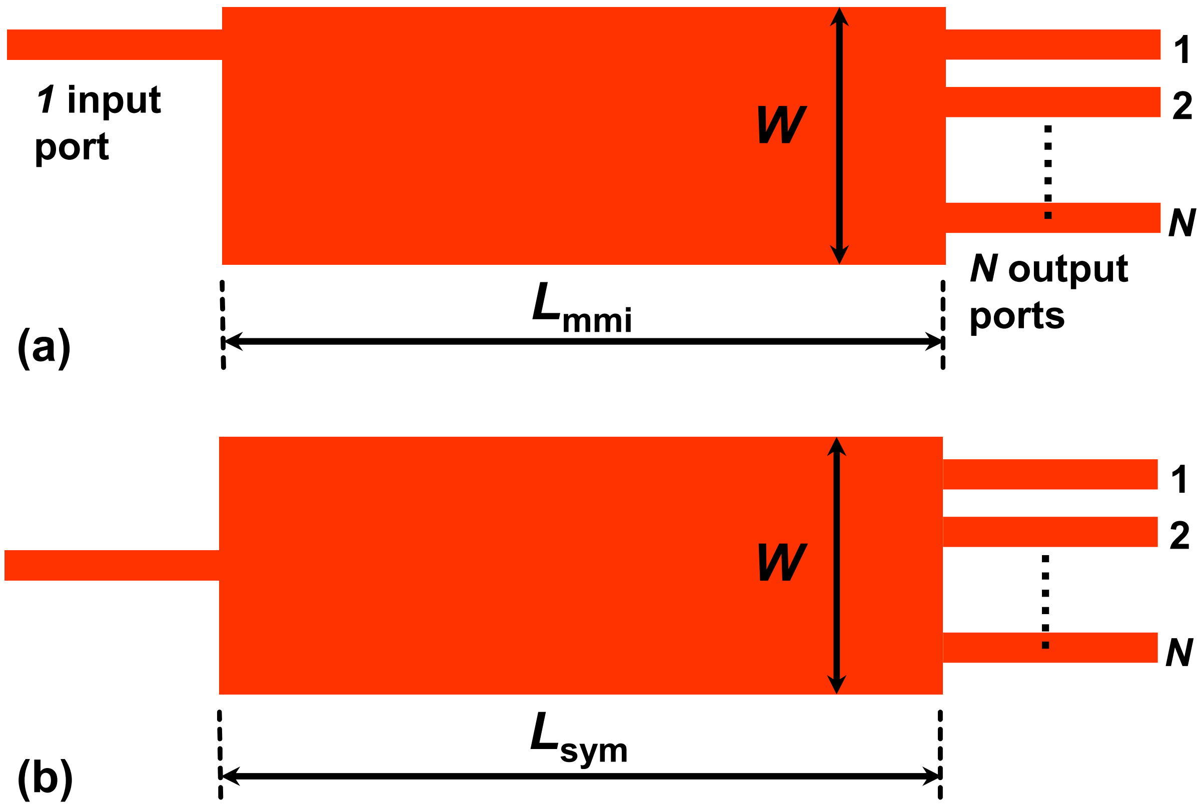

Figure 2.7: Schematic of integrated MMI couplers. (a) General-interference MMI. (b) Symmetric-interference MMI.

1*N splitter can be reduced to:

$$L_{\text{sym}} = \frac{3L_\pi}{4N}, \tag{2.2}$$

which is a 4-fold decrease compared to the general interference in Equation 2.1. However, only 1 input port is allowed under symmetric interference.

In Fig. 2.7, we show two example schematics of MMI, one with general interference and one with symmetric interference, both have a 3 µm wide multimode region. Fig. 2.8 then shows the calculated mode profile evolution using (a) general interference and (b) symmetric

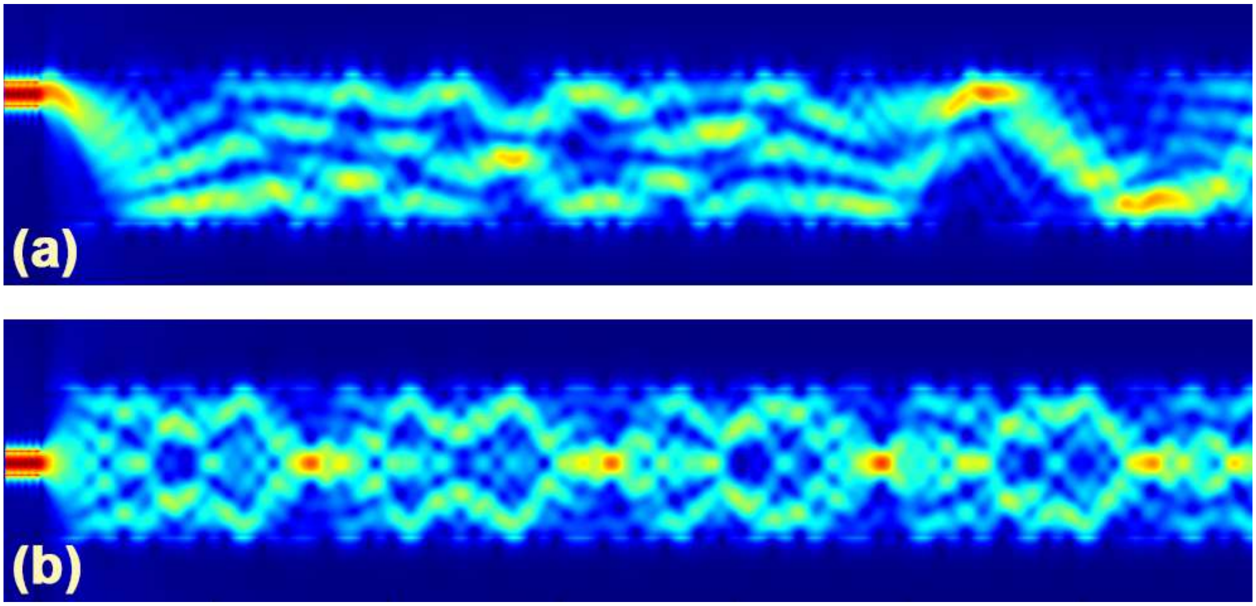

Figure 2.8: Electric field intensity distribution of light propagation in two types of silicon photonic MMI. (a) General-interference MMI. (b) Symmetric-interference MMI.

interference.

MMI couplers are widely used in silicon photonics for various types of devices, including power splitters [44], PBS [45], wavelength multiplexers [46], and optical 90° hybrids [47].

2.3 Active silicon photonic devices

2.3.1 Modulators

Electro-optic modulators are crucial active devices for optical communication systems. They convert the high-speed electrical signal to the optical domain in the transmitter. On silicon, the high-speed phase modulation is mainly achieved by the plasma dispersion effect and the operation frequency can go up to tens of GHz [33]. P-type and N-type doping can be applied to silicon rib waveguides as shown in Fig. 2.2. After the PN junction is formed, applying a voltage results in carrier injection or depletion that changes the refractive index of the materials, forming a phase shifter.

Based on phase shifters, intensity or amplitude modulation can be achieved by leveraging certain interferometric or resonant structures. Typical high-speed silicon photonic modulators are based on Mach-Zehnder interferometers (MZI) where the two arms both contain an electro-optic phase shifter. By phase modulation on both arms but with opposite phase-changing directions, we can create constructive or destructive interference with MZI structures, outputting different levels of optical intensity. With optimized electrode designs, the 3-dB bandwidth of silicon traveling-wave Mach-Zehnder modulators (TWMZM) can reach > 40 GHz [48]. It has been reported that silicon photonic IQ TWMZM can support up to net 1.0 Tb/s coherent transmission per channel. [49].

Another type of silicon photonic modulator is the ring modulator. Ring modulators utilize the response of all-pass ring resonators and are usually more compact than TWMZMs. However, ring modulators suffer from high sensitivity to temperature and chirp penalties [50]. Still, with advanced designs, net 1.0 Tb/s coherent transmission has also been demonstrated with ring-based silicon photonic modulators [51].

2.3.2 Photodetectors

At the receiver of the optical communication system, photodetectors are the key components to convert optical signals back to the electrical domain for them to be further processed and decoded. Although silicon is a proper material for the detection of visible light, it does not absorb NIR wavelengths where optical communication bands are located. Therefore, Germanium (Ge) can be integrated on top of the silicon layer as shown in Fig. 2.2 as the material for PD of the NIR wavelength range. Such integration methodology has been demonstrated in various works [52] and it is widely accepted as a standard of achieving on-chip photonic detection on silicon.

2.4 Silicon photonic transceivers

Optical transceivers, consisting of transmitters and receivers, are crucial components for optical communication systems where the signal is converted between electrical and optical domains. In this section, we will introduce the basic schematics of the two typical optical transceivers, namely the intensity-modulation direct detection (IM/DD) transceivers and the coherent transceivers. The DSP techniques used in both transceivers will also be covered since DSP is one of the enabling technologies to achieve high-performance transmission in modern optical interconnects.

2.4.1 IM/DD transceivers

IM/DD optical communication is a simple and cost-effective system architecture. IM/DD transmission systems are now widely adopted in short-reach interconnections such as intra-datacenter communication. A typical schematic of IM/DD systems is shown in Fig. 2.9.

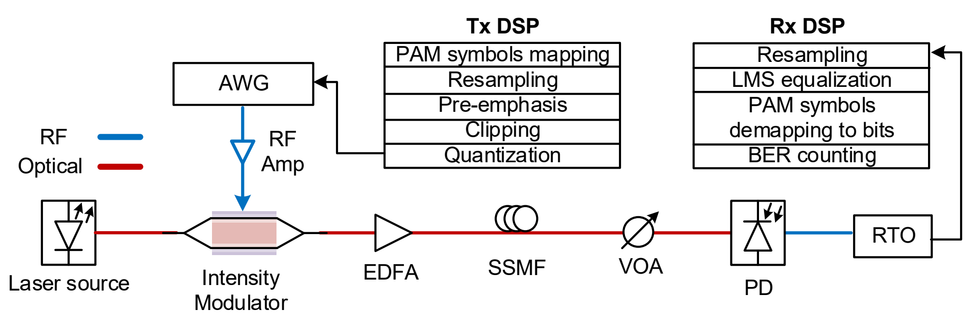

Figure 2.9: Schematic of IM/DD optical communication system.

The information is encoded on the intensity domain by a single intensity modulator. At the receiver, a single-ended PD detects the optical signal to convert it to the electrical domain. The DSP is relatively simple. Transmitter DSP includes pulse amplitude modulation (PAM) symbol generation, resampling, pre-emphasis, clipping, and quantization. Receiver DSP includes resampling, equalization, symbol decision, and BER counting. Pulse shaping at the transmitter and matched filtering are not necessary.

Silicon photonics transceivers for IM/DD systems integrate the modulators and the PDs on the same die. As IM/DD systems are simple, low-cost, and energy-effective, such transceivers usually integrate multiple channels of transmission to maximize the total capacity. Therefore the transceivers also integrate wavelength multiplexers and demultiplexers.

Despite its simplicity in both hardware and software, the IM/DD system is limited in terms of capacity. Meanwhile, fiber impairments such as chromatic dispersion (CD) cannot be compensated in IM/DD systems due to the loss of phase information in direct detection.

2.4.2 Coherent transceivers

Coherent optical communication is commonly used in long-haul transmission, metro networks, and inter-datacenter interconnection. Compared to direction detection, coherent detection can largely improve the receiver sensitivity with the help of a local oscillator (LO). Moreover, coherent detection can retrieve amplitude and phase information. With the help of DSP, such a scheme enables the compensation for CD, polarization mode dispersion (PMD), frequency offset (FO), linear phase noise, and even fiber nonlinearity [53]. Such capability largely increases the reach limit of coherent transmission systems.

An example schematic of a single-polarization coherent transmission system is shown in Fig. 2.10.

The signal is modulated on the optical field by an IQ modulator, rather than the intensity. The IQ modulator consists of two amplitude modulators biased at the null point, one of which is followed by a 90° phase shifter. At the receiver, the LO beats with the signal in the 90° hybrid. Two balanced photodetectors (BPD) converted the received I and Q signals

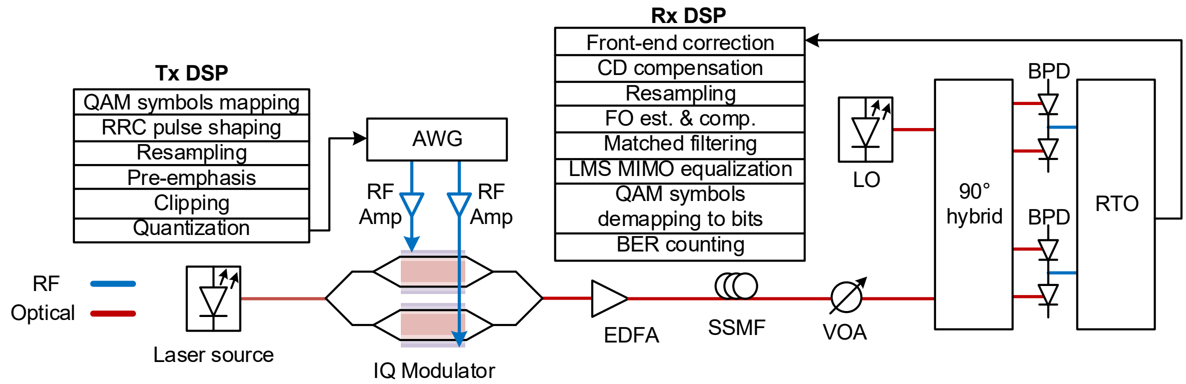

Figure 2.10: Schematic of coherent optical communication system.

to the electrical domain. The DSP takes care of the compensation of various sources of distortion, including CD and FO. Channel intersymbol interference (ISI), phase noise, and PMD (in a dual-polarization system) can be jointly compensated by a decision-directed least mean square (DD-LMS) adaptive multiple-input-multiple-output (MIMO) equalizer. Root-raised-cosine (RRC) pulse shaping and matched filtering are usually needed to maximize the signal-to-noise ratio (SNR).

Silicon photonic coherent transceivers integrate IQ modulators, 90° hybrids, and BPDs. Dual polarization transmission is usually adopted to double the capacity of a single wavelength channel. Therefore, on-chip polarization-manipulating devices such as PSRs need integration as well.

Chapter 3

SWG-assisted high-performance 1310/1550 nm wavelength diplexer

3.1 Motivation

1310/1550 nm wavelength diplexers are essential in modern passive optical networks which utilize these two wavelengths simultaneously. Different structures have been proposed for this device, mainly including multimode interference (MMI) couplers [54–56], directional couplers (DCs) [57–59], and grating couplers [60, 61]. Diplexers based on advanced optimization techniques such as inverse design [62, 63] and particle swarm optimization (PSO) [64] were demonstrated as well.

Among all the designs mentioned above, the MMI coupler stands out because of its low insertion loss (IL) and broad bandwidth [43]. Nevertheless, to realize wavelength multiplexing, the length of the multimode interference section must be a common multiple of the first self-imaging length of both wavelengths. Limited by this requirement, a 1310/1550 nm diplexer based on the MMI usually comes with a large footprint. Efforts have been made to make MMI-based wavelength diplexers more compact, utilizing novel structures such as Bragg gratings [65], photonic crystals [66], and SWG [67]. The SWG, which can be regarded as a homogeneous material when its pitch is small enough [68], enables more flexible design for integrated photonic devices fabricated using a single etch step. Benefiting from advancing fabrication technologies, the SWG has shown its powerful functionality in various silicon photonic devices over the past decade, such as power splitters [69], microring resonators [70], polarization beam splitters [71], and waveguide crossings [72]. In [67], an SWG slot was introduced in the middle of an MMI coupler to shrink the device length to ~30% of previously reported designs. A more recent work [73] applied the similar idea to add double SWG slots to the MMI coupler, further reducing the device length. However, both designs were only verified by simulation, and the extinction ratios (ER) are relatively low.

In this chapter, we propose a compact 1310/1550 nm wavelength diplexer design based on a two-mode interference (TMI) coupler. Despite the small footprint, this design is still shown to have high ER, low IL, and relatively large bandwidth.

3.2 Design and analysis

The device schematic is displayed in Fig. 3.1. The mode interference section has a length of L and a width of W. Compared with regular MMI/TMI couplers, our device has an SWG slot along the direction of light propagation. This slot is placed in the middle with a width of W_{swg}. As a periodic structure, the SWG is described with a pitch Λ and a fill factor ff, so that the lengths of a ridge (Si) and a groove (oxide cladding) in one period are $\Lambda * ff$ and $\Lambda * (1 - ff)$, respectively. Since the gratings need to operate in the subwavelength regime, $\Lambda < \lambda/2n_{eff}$ should be fulfilled at all operating wavelengths. The upper bound of the pitch is about 218 nm at $\lambda = 1310$ nm, thus Λ is preset to 200 nm. In addition, a taper with a length of L_t is utilized to connect the MMI/TMI access port of width W_a to the interconnecting waveguide of width W_g. To minimize the crosstalk at the output ports, we introduce an offset Δ between the centers of the access port and the strip waveguide, as shown in Fig. 3.1.

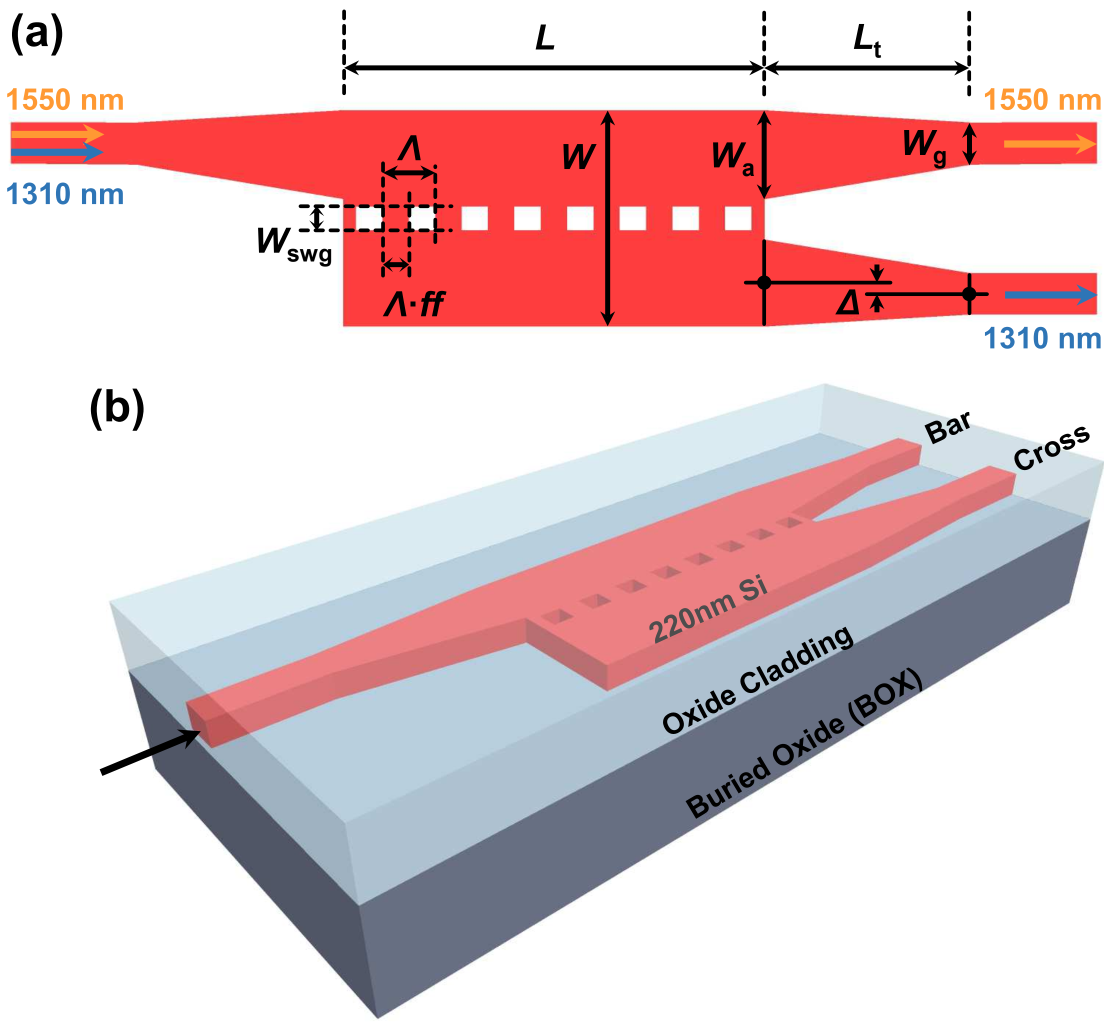

Figure 3.1: (a) 2D and (b) 3D schematics of the proposed device.

In any coupler implementing a mode interference scheme (MMI, DC, TMI), a key step in the design process is to calculate the beat length of the two lowest order modes. This beat length is defined as $L_\pi = \lambda/2/(n_{eff0} - n_{eff1})$. In order to separate the two wavelengths 1310 nm and 1550 nm, the following equation should be satisfied:

$$L_{lcm} = n * L_{\pi,1310} = m * L_{\pi,1550}, \tag{3.1}$$

where L_{lcm} is the least common multiple of the beat lengths at 1310 nm and 1550 nm, and integers n and m should have different parity (either even and odd, or odd and even). Here we define a beat length ratio $R = L_{\pi,1310}/L_{\pi,1550}$.

Next, the device length L can be determined as:

$$L = a * L_{lcm}, \tag{3.2}$$

where a is a constant depending on the type of device. a equals 3 for MMI couplers (general interference) [74] whereas the value becomes 1 for DCs and TMI couplers.

To minimize the device length, the values of n and m in (1) should be as small as possible. However, in conventional MMI couplers it is hard to tune the beat length ratio R and achieve certain values of n and m, since the coupler width is the only parameter to adjust. This is illustrated in Fig. 3.2(a), where we change the width of a conventional MMI coupler without any slot and calculate the corresponding beat length ratio for both the TE and TM modes. Here we use the FDE solver for the mode effective index calculation. The result indicates that the ratio hardly changes near 1.25 with the TE mode so that $m = 5, n = 4$, leading to a long interference section. In the case of the TM mode, the ratio is close to 1.33 implying $m = 4, n = 3$, which are still large values.

Therefore we insert an SWG slot in an MMI coupler to adjust the beat length ratio with more degrees of freedom. First, we replace the SWG with a homogeneous material with index n_{swg} based on the effective medium theory, so that the 2D analysis using the FDE solver is enabled. Initially, we conduct a parameter sweep on W_{swg}, assuming n_{swg} is 2.5 and W is 2.5 µm. Then we plot the beat lengths at $\lambda = 1310$ nm, as well as the ratio R in Fig. 3.2(b). The

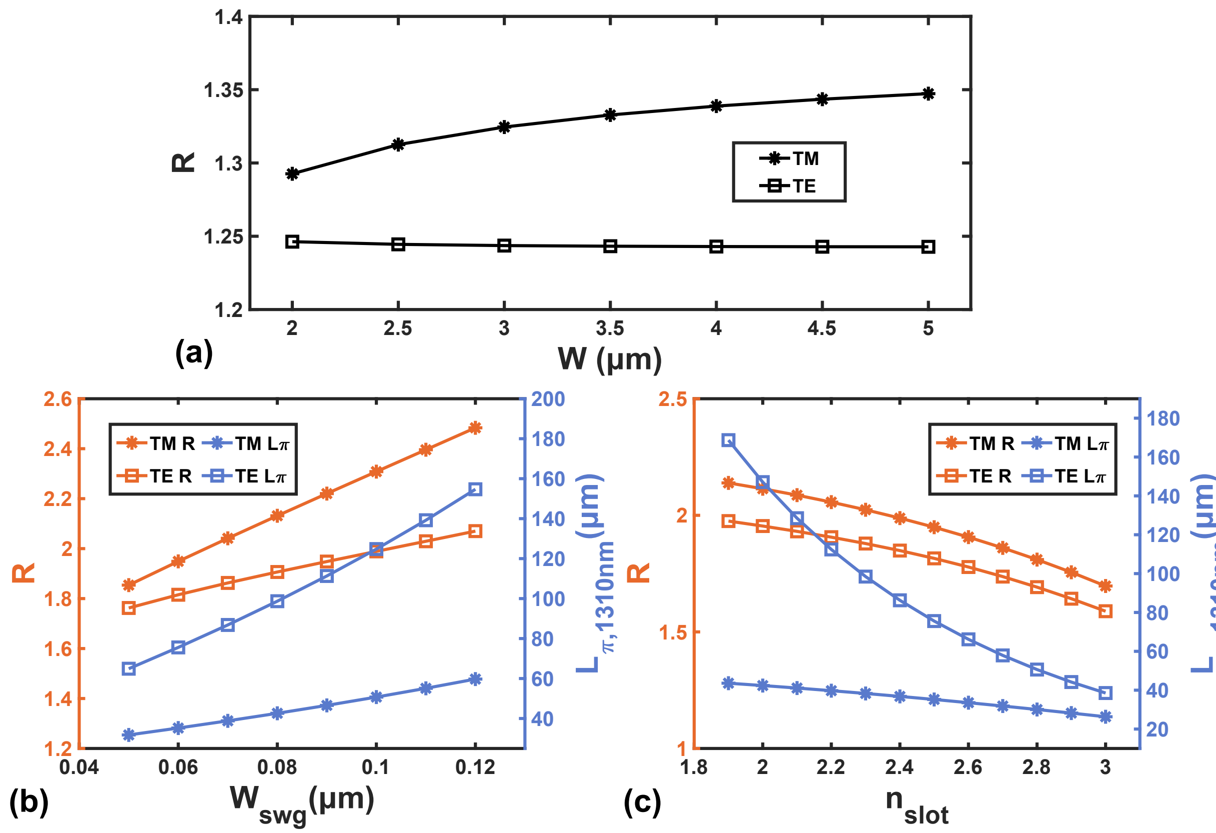

Figure 3.2: Calculated beat length ratio, and beat length at $\lambda = 1310$ nm for both the TM and TE modes, as functions of (a) width of the MMI coupler (without the SWG slot), (b) width of the SWG slot and (c) equivalent refractive index of the SWG slot.

reason we select $W = 2.5$ µm is that W should be large enough to avoid crosstalk between the two output single-mode waveguides, whilst on the other hand, W should be as small as possible so that the coupler length is minimized. Hence, $W = 2.5$ µm is a proper choice. As a result, $R_{TM} \approx 2$ is achieved at $W_{swg} = 0.06$ µm, whereas $R_{TE} \approx 1.8$. With $R = 2$ the values of m, n are actually minimized to $m = 2, n = 1$, which is the ideal case. Although we can realize this target ratio with the TE mode as well by increasing W_{swg}, the beat length almost triples compared with the TM mode. Meanwhile, since the minimum feature size of the fabrication process we plan to use is 0.06 µm, we fix $W_{swg} = 0.06$ µm because it provides the smallest beat length. Then we optimize n_{swg}. Similarly in Fig. 3.2(c) where the ratio is plotted as a function of n_{swg} with the fixed $W_{swg} = 0.06$ µm, $R_{TE} = 2$ can only be reached with $n_{swg} \approx 1.9$ at the cost of a large beat length. Thus, we choose the TM mode to be the operating mode for a more compact design. As shown in Fig. 3.2(c) the optimal value of n_{swg} is 2.4. This value will be used for estimating the fill factor ff in the 3D simulation analysis where we apply the actual SWG structures.

The next step is to design the taper. Normally the taper design rule for MMI couplers is simple, i.e. the access port should be wide enough and we need large intervals between ports to compress the crosstalk. However, the taper needs to be carefully examined in our device since it fundamentally affects its working principle. It is revealed that increasing the access port width W_a in a slotted MMI coupler reduces the excitation of higher-order modes, leaving only TM0 and TM1 modes. To verify this, we perform 3D FDTD simulations in which we set up a mode expansion monitor in the mode interference section to calculate the proportion of each excited mode in terms of power. The width of the interconnecting single-mode waveguide is set to $W_g = 350$ nm to meet the single-mode condition for the O-band. The offset Δ is set to 0 temporarily, and the taper length is preset to $L_t = 9$ µm, which is long enough to avoid the excitation of high-order TM modes at the access ports. As shown in Fig. 3.3(a) and (b), increasing the port width to $W_a = 1.2$ µm effectively reduces the excitation of TM2 and higher-order modes. With only TM0 and TM1 modes being equally excited, the device functions as a TMI coupler instead of an MMI coupler. Therefore, the value of a in equation (2) will be 1 rather than 3, resulting in a much smaller device length. We draw several bar port transmission spectra of a sample device with an arbitrary length in Fig. 3.3(c) as we change W_a, and we observe that a large value of W_a is the key to effective device performance. Such design result in the high ER of the proposed wavelength diplexer.

Since $L = a * n * L_{\pi,1310}$, our design reduces the coefficient $a * n$ by a factor of 9. Although the beat length of a regular MMI coupler with the same width at $\lambda = 1.31$ µm is ˜43% of that in our device, the device length is still shortened by a factor of 3.87.

There exists a similarity between TMI and DC. They both make use of the interference between the two lowest-order modes. The TMI in [75] is in fact regarded as a zero-gap directional coupler (ZGDC). Consequently, our device can be considered as a narrow-gap directional coupler (NGDC). This can be further explained by the mode profiles displayed in Fig. 3.4. Our proposed device shares a similar electric field magnitude distribution as regular DC, proving the analogy between TMI and DC.

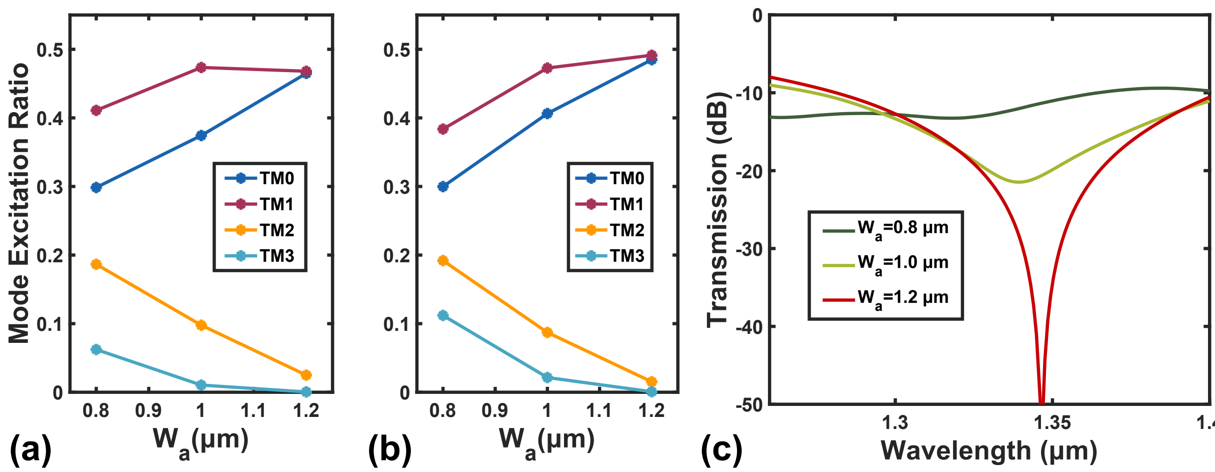

Figure 3.3: Calculated power distributions of the TM modes excitation under different access port widths W_a, at (a) λ = 1550 nm and (b) λ = 1310 nm. (c) Dependence of transmission spectra on W_a.

Since a much wider access port is applied, the crosstalk between the bar and the cross ports is no longer negligible, which will cause the transmission spectrum to shift. Our solution to this problem is to create an offset Δ for all the access waveguides on the y-axis, as illustrated in Fig. 3.1(a). 3D FDTD simulations are again performed to calculate the crosstalk with different Δ. However, the simulation model applied here is different, where the coupler part is removed and only the two output waveguides and tapers are considered. With the top interconnecting waveguide being the input port, we calculate the transmission through the bottom access port as the crosstalk. The results are shown in Fig.

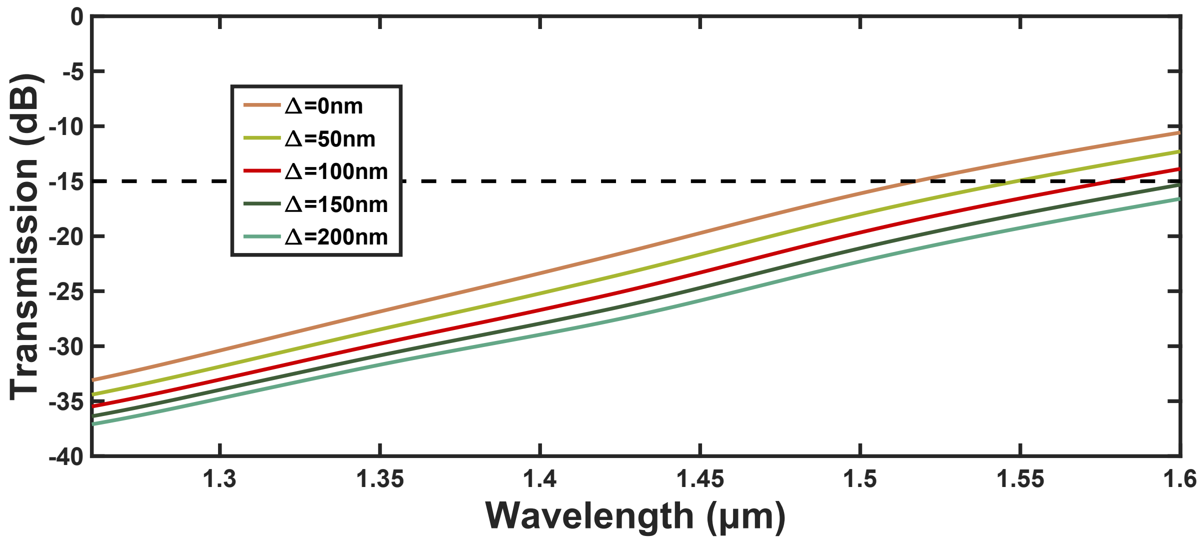

Figure 3.4: Calculated crosstalk between bar and cross ports as a function of wavelength, under various values of offset Δ.

3.4. The crosstalk cannot be fully eliminated due to the relatively large access port width. Nonetheless, since the TMI coupler works as a DC under this scheme, we can regard the TMI coupler and the taper section as two cascaded DCs. As long as we compress the crosstalk to an insignificant amount, we can always recover the intended transmission spectrum by slightly tuning the length of the TMI coupler. As a result, we set Δ to 0.1 µm so that the crosstalk at $\lambda = 1310$ nm and $\lambda = 1550$ nm are both below -15 dB, which is insignificant enough.

The other device geometries, including fill factor ff and TMI length L, are determined by performing a joint parameter sweep analysis using 3D FDTD simulations as mentioned above, where we replace the homogeneous material with a real SWG. We use Rytov's formulas [76] to estimate the ff that corresponds to the theoretical value of n_{swg} (2.4), as the start point of the joint sweep. Then we calculate $L = L_{\pi,1310}$ under each ff as the reference for choosing lengths in the sweep. In Fig. 3.5, we show the featured transmission spectra under 3 fill factors $ff = 0.30, ff = 0.37, ff = 0.44$, each with 5 different TMI lengths. According

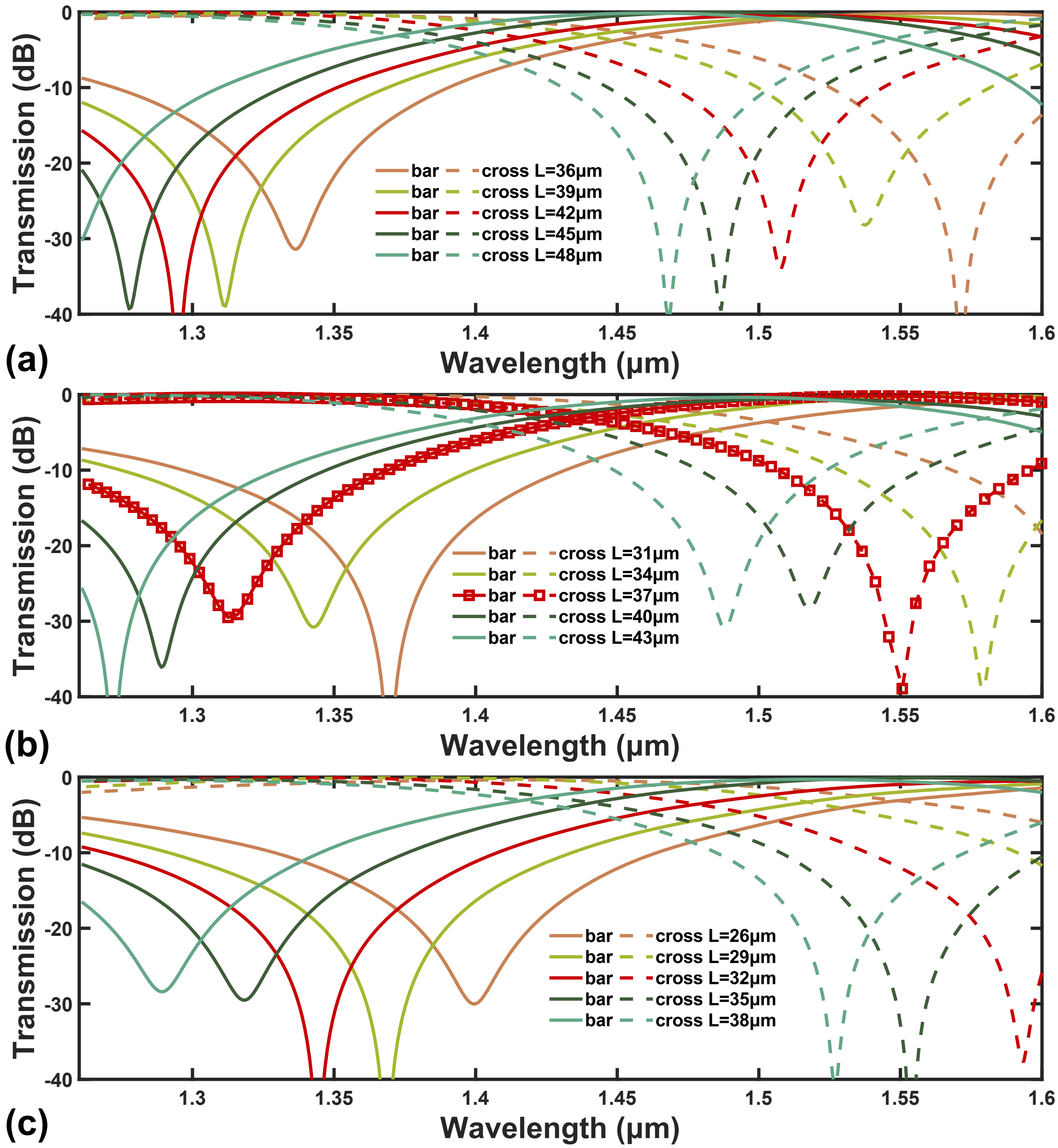

Figure 3.5: Simulated transmission spectra of both bar and cross ports under different TMI length L at (a) $ff = 0.30$, (b) $ff = 0.37$ and (c) $ff = 0.44$. The optimized spectrum is the emphasized red curve with markers in (b).

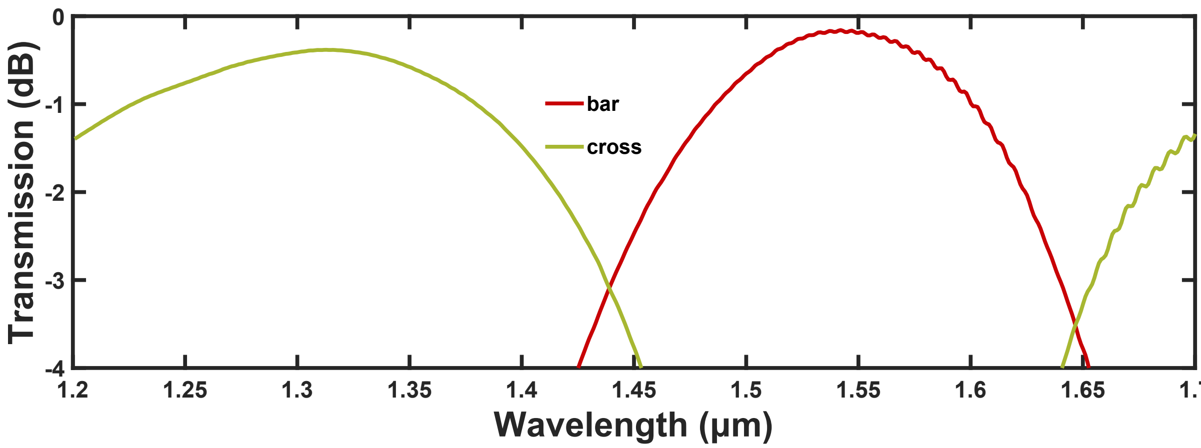

Figure 3.6: Magnified transmission spectra of the bar and cross ports with the optimal parameters. This figure illustrates the 1-dB-IL bandwidths at both ports.

to the results, the device length and fill factor of the SWG are determined as $L = 37$ µm and $ff = 0.37$, respectively, under which the transmission spectra of the two output ports have minimum points at the target wavelengths. Quantitatively analyzing, we define the figure of merit (FOM) of the optimization as the summation of the transmission (in dB) through the bar port at $\lambda = 1310$ nm and the transmission (in dB) through the cross port at $\lambda = 1550$ nm, and we need to minimize the FOM. With the combination of $L = 37$ µm and $ff = 0.37$, the FOM reaches -71.16 dB, which is the minimum value among all the parameter pairs shown in Fig. 3.5.

IL and ER are commonly used metrics for these types of devices, which are defined as:

$$\mathrm{IL} = 10 * \log_{10}(P_{in}/P_{out}), \tag{3.3}$$

$$\mathrm{ER} = 10 * \log_{10}(P_{out}/P'_{out}), \tag{3.4}$$

where P_{out} is the optical power of the corresponding output port for a particular wavelength (bar for 1550 nm and cross for 1310 nm), and P'_{out} is the power of the other output port

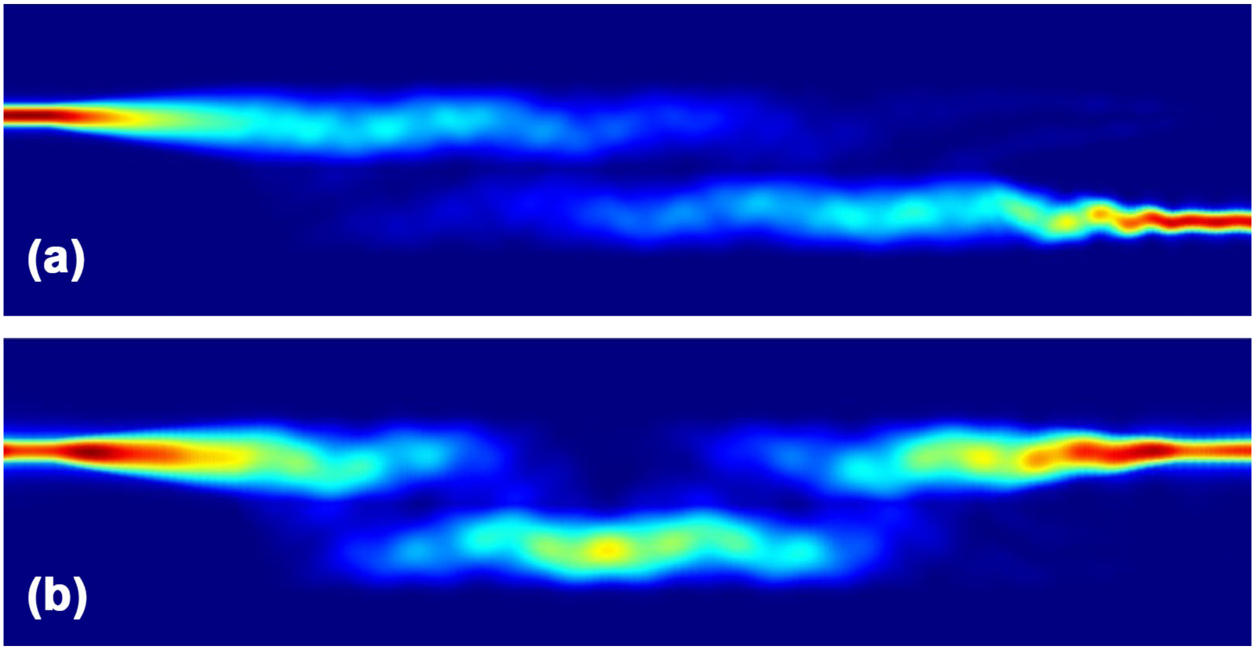

Figure 3.7: Calculated mode evolution (power density distribution) of the proposed device at (a) $\lambda = 1310$ nm and (b) $\lambda = 1550$ nm.

(cross for 1550 nm and bar for 1310 nm). P_{in} stands for the input power. The simulation results indicate that the values of IL and ER are 0.36 dB and 28.05 dB at $\lambda = 1310$ nm, respectively, and 0.21 dB and 42.54 dB at $\lambda = 1550$ nm, respectively. As illustrated in Fig. 3.6, the 1-dB-IL bandwidth at O-band is as wide as 192 nm from 1203 nm to 1395 nm. To the best of our knowledge, this is one of the largest values that are reported. Such a wide band may stem from the beat length ratio of 1:2, under which there is no spectral peak at shorter wavelengths than 1310 nm. Therefore the IL declines slowly around the O-band. As for the C-band, the 1-dB-IL bandwidth is 123 nm from 1482 nm to 1605 nm, which also meets the ITU standard. For the ER bandwidth, we use 15 dB as the criteria, which ensures that the signal at the unwanted wavelength can be attenuated to a level that will not severely distort the signal being transmitted. As a result, ER $>$ 15 dB is achieved within a 65 nm range and a 50 nm range in the O-band and the C-band respectively. Mode evolution at both wavelengths are demonstrated in Fig. 3.7, where we can clearly observe the ideal beat length ratio of $m/n = 2/1$.

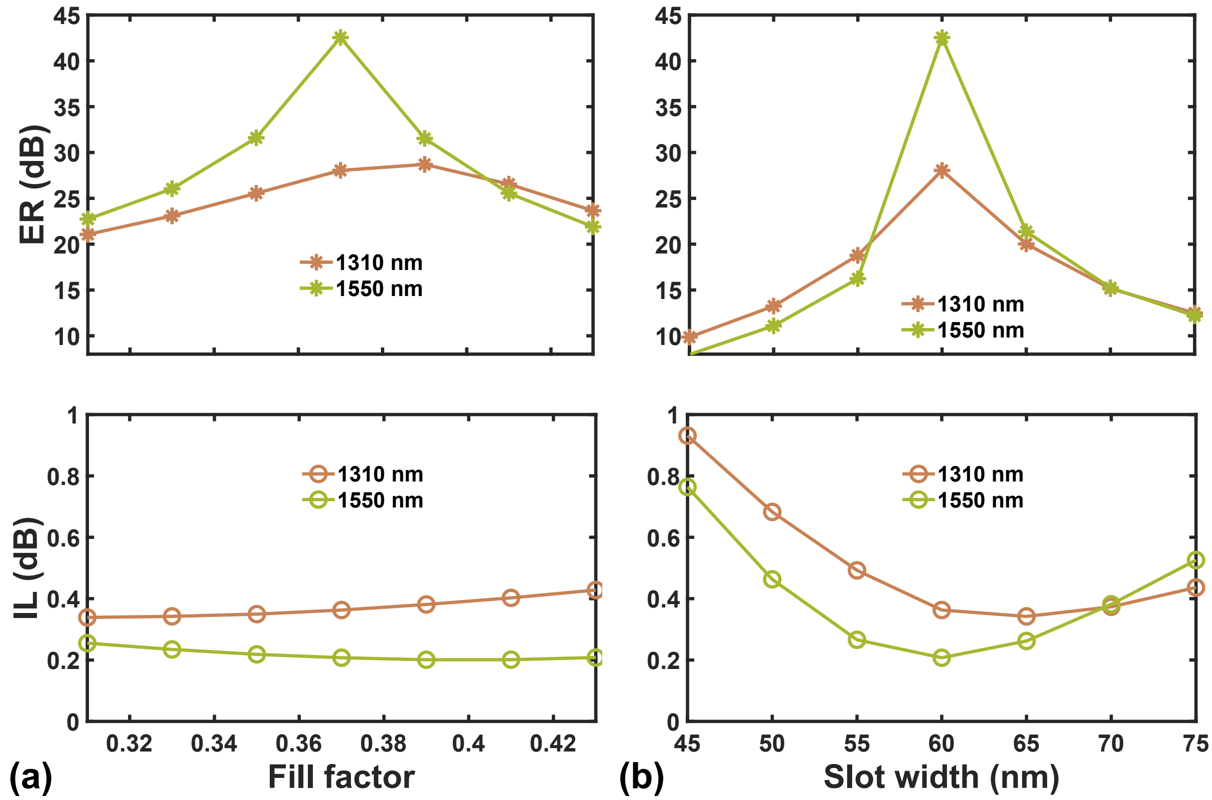

Figure 3.8: Dependence of the ILs and ERs on (a) the fill factor and (b) the SWG slot width.

Fabrication tolerance tends to be an problem for devices with fine features such as SWG. As for our proposed device, we analyze the impact of the slot width W_{swg} and the fill factor ff. As demonstrated in Fig. 3.8(a), even with a fill factor ranging from (0.31,0.43), the ILs at both ports do not exceed 0.45 dB, and the values of ER are maintained above 20 dB. Since the fill factors of gratings are likely to drift in fabrication, such results prove the robustness of our SWG-based design. Fig. 3.8(b) shows that the width change of the SWG slot from 60 nm to 45 nm reduces the ER to 9.85 dB at 1310 nm and 7.80 dB at 1550 nm, whereas the values of IL are kept below 1 dB at both ports. Hence, the SWG slot width should be the main parameter to be controlled in the tape-out process. On the other hand, The minuscule holes in the SWG slot may cause imperfect filling of the cladding. Therefore, we simulate the same structure without silica deposited into the holes to evaluate the influence of this effect. It is revealed by simulation that even with such an extreme model, the ILs and ERs at 1310/1550 nm achieve 0.33/0.23 dB and 21.31/25.72 dB, justifying that the impact is not fatal at all.

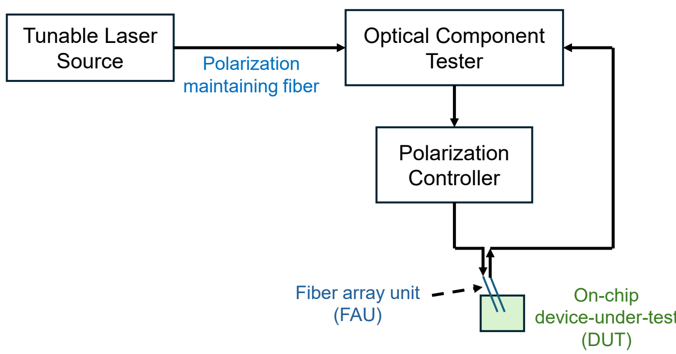

Figure 3.9: Schematic of the testing setup for passive integrated devices.

3.3 Fabrication and characterization

The device is fabricated using the NanoSOI fabrication process provided by Applied Nanotools Inc. The chip has a 220-nm-thick Si layer on a 2-µm-thick buried oxide layer, with a 2.2-µm-thick cladding oxide on top. The testing setup is shown in Fig. 3.9. We use grating couplers with a broadband design [77, 78] to guide the light between the chip and the fiber array. The light sources are the Yenista TUNICS T100S-HP O-band and C-band tunable lasers, assisted by a Yenista CT400 passive optical component tester to conduct efficient measurements. A polarization controller (PC) is inserted between the laser and the device to minimize the coupling loss. Since the grating couplers are designed only for either the O-band or the C-band, the proposed 1310/1550 nm diplexer is fabricated in pairs connected to different grating couplers, so that we can obtain the transmission spectra of both bands for the same structure. Grating coupler pairs that are connected directly are fabricated alongside the devices for data normalization. A polarization controller is inserted between the laser and the device to maximize the power of the TM-polarized light.

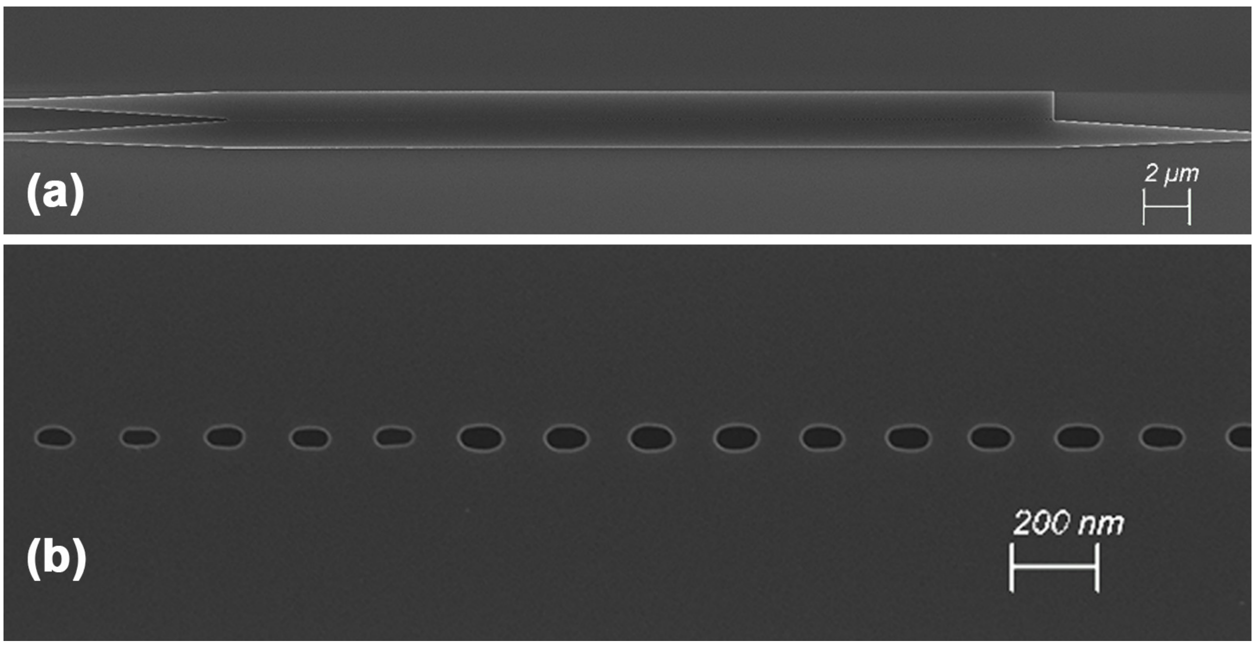

Figure 3.10: SEM images of (a) the wavelength diplexer and (b) the SWG slot.

The images from the scanning electron microscope (SEM) are displayed in Fig. 3.10, which shows that the on-chip SWG slot has been successfully constructed. The power transmission spectra in both the O-band and the C-band are displayed in Fig. 3.11. The measured IL and ER at $\lambda = 1310$ nm are 0.33 dB and 19.58 dB, respectively, whereas the values at $\lambda = 1550$ nm are 0.45 dB and 26.56 dB, respectively. The experimental results differ from the simulation results that the minimum point of the O-band transmission spectrum in the bar port is not located at 1310 nm (it is shifted by approximately 20 nm). However, the device still demonstrates excellent properties in terms of bandwidth. The

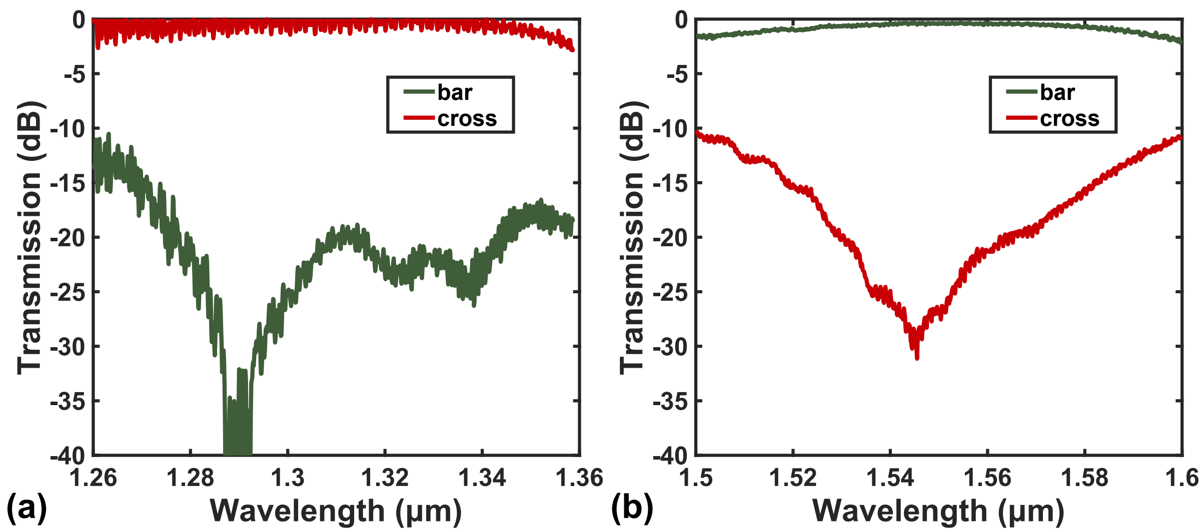

Figure 3.11: Measured transmission spectra in (a) the O-band (1260 nm - 1360 nm) and (b) the C-band (1500 nm - 1600 nm).

fabricated device achieves an ER higher than 15 dB over an 82-nm wavelength range in the O-band from 1277 nm to 1359 nm, and a 56-nm range in the C-band from 1525 nm to 1581 nm. Since oscillations are observed in the measured spectra, especially in the O-band, it is hard to characterize the 1-dB-IL bandwidth. Nevertheless, even with the defect, the measured IL is less than 2 dB within an 88-nm bandwidth in the O-band from 1266 nm to 1354 nm, and a 99-nm bandwidth in the C-band from 1500 nm to 1599 nm.

In Table 3.1, we compare the performances of various reported silicon 1310/1550 nm wavelength diplexers based on similar principles (DC, MMI). It is shown that our proposed design exhibits high ER and wide bandwidths in terms of both IL and ER. Furthermore, the device achieves one of the shortest lengths among experimentally verified counterparts.

Reference	Structure	1-dB-IL BW (nm)		ER (dB)		15-dB-ER BW (nm)	
		O-band	C-band	1310 nm	1550 nm	O-band	C-band
[57]	DC	/	/	25.67	14.89	˜40	˜35
[58]	DC	/	/	27.07	25.84	>80	˜70
[59]	DC	140	125	˜15	˜23	/	/
[66]	MMI	/	/	32.60	16.40	74	103
[67]	MMI	150	120	22.18	20.10	/	/
[73]	MMI	>90	>90	15.20	16.80	/	/
This work	TMI	192	123	28.05	42.54	65	50
This work	TMI	/	/	19.58	26.56	82	56
Reference	Length(µm)	Polarization		Method			
[57]	48.2	TE&TM		Simulation			
[58]	150	TE		Experiment			
[59]	13.5	TE		Simulation			
[66]	108.5	TE		Experiment			
[67]	43.4	TE		Simulation			
[73]	34.5	/		Simulation			
This work	37	TM		Simulation			
This work	37	TM		Experiment			

Table 3.1: Performance comparison with previously reported 1310/1550 nm wavelength diplexers on the SOI platform

3.4 Conclusion

In conclusion, we propose and experimentally verify a novel TMI-coupler-based high-performance 1310/1550 nm diplexer on a standard 220-nm SOI platform. It is shown that the insertion of an SWG and an appropriate design of the tapers make an MMI coupler operate in a two-mode interference scheme that reduces the device length while maintaining high ER. Meanwhile the device achieves an ideal beat length ratio of 2:1 for the two target wavelengths using the TM mode, which makes the device more compact with a TMI coupler length of only 37 µm. With 3D FDTD simulations, the proposed diplexer achieves 1-dB-IL bandwidths larger than 120 nm and 15-dB-ER bandwidths larger than 50 nm at both ports. As for the peak values, the calculated ERs at 1310 nm and 1550 nm reach 28.05 dB and 42.54 dB, respectively. The measured results of the fabricated device indicate that ILs at λ = 1310 nm and λ = 1550 nm are 0.33 dB and 0.45 dB, respectively. Measured 15-dB-ER bandwidths of 82 nm and 56 nm are accomplished in the O-band and the C-band, respectively, and the ER reaches 19.58 dB at λ = 1310 nm and 26.56 dB at λ = 1550 nm. Analysis of fabrication tolerance is conducted, and the results prove that the proposed structure is rather insensitive to the fluctuation of the SWG fill factor, which eases the optimization in the fabrication process.

Chapter 4

Broadband all-silicon photonics TM-pass polarizer on 220 nm SOI

4.1 Motivation

Due to the polarization-sensitive nature of the SOI, polarization-handling devices have played important roles in circuit design, including PBS [79–86], PSR [87–93], and polarizers. Among them, the polarizers are used to block the unwanted polarization and minimize the polarization crosstalk, thus are basic components for PICs that work with a single polarization.

Various types of polarizers have been reported using different principles. Metal-silicon hybrid TE-pass [94] and TM-pass [95–98] polarizers exhibit relatively high bandwidth with compact structures, but they tend to be lossy due to the absorption of metal. Chen et al. [59] demonstrated a low-loss hybrid plasmonic TM-pass polarizer by polarization-dependent mode conversion but it has a narrow operating bandwidth. Nevertheless, such hybrid designs require additional post-processing and consequently add complexity to fabrication. Therefore, there is an increased interest in all-silicon polarizers with high performances. TM-pass polarizers based on doped silicon waveguide have been proposed [99, 100]. These designs only involve silicon and silicon dioxide and are compatible with the CMOS process. However, they share similar working principles with metal-silicon polarizers, therefore having relatively high insertion losses (ILs). Periodic structures such as SWG [101–103] and photonics crystals [104–107] demonstrate polarization-sensitive band structures as explained in [108], hence can function as polarizers as well. However, those devices are usually designed for only one or two optical bands (~100 nm bandwidth). Consequently, they are not suitable for high-capacity multi-band silicon PICs that work with most or all optical wavelength bands (O-, E-, S-, C-, L-, and U-bands).

Efforts have been put to realize the broadband operation in all-silicon polarizers. Xu et al. [109] proposed a TE-pass polarizer with a 415 nm bandwidth enabled by the anisotropic nature of SWG, whilst Liu et al. [110] demonstrated a TE-pass polarizer that covers the same bands based on different mode properties of TE and TM in a shallow-etched silicon waveguide. Both devices maintain low ILs and high polarization extinction ratios (PERs) over all optical bands, but they both use air claddings that are not practical for packaging. As for the TM mode, Wang et al. [111] showed a high-performance Bragg-grating-based silicon TM-pass polarizer that covers a 264 nm bandwidth, but the device is designed on a sandwich-structured waveguide with two silicon layers and an oxide layer in the middle, vertically. Thus the device is not compatible with most device designs on the single-layer SOI platform, and it is only verified by simulation. A hyperuniform disordered silicon photonic TM-pass polarizer was demonstrated [112]. Such structures exhibit wide and isotropic bandgaps, enabling a 240 nm bandwidth (1440 - 1680 nm). However, the IL threshold over the operation bands is relatively high (~3 dB). A recent work [113] reported a high-performance all-silicon TM-pass polarizer that covers the 415 nm bandwidth by a double slot Euler waveguide bending. In spite of the ultra-broadband operation, the device depends on the index profile asymmetry realized by the air cladding, which introduces the same packaging issue as [109, 110].

To address the aforementioned challenges, in this chapter, we propose an all-silicon

TM-pass polarizer that operates in multiple optical telecommunication bands, enabled by multiplexing different regimes of the gratings.

4.2 Design and analysis

4.2.1 Theory

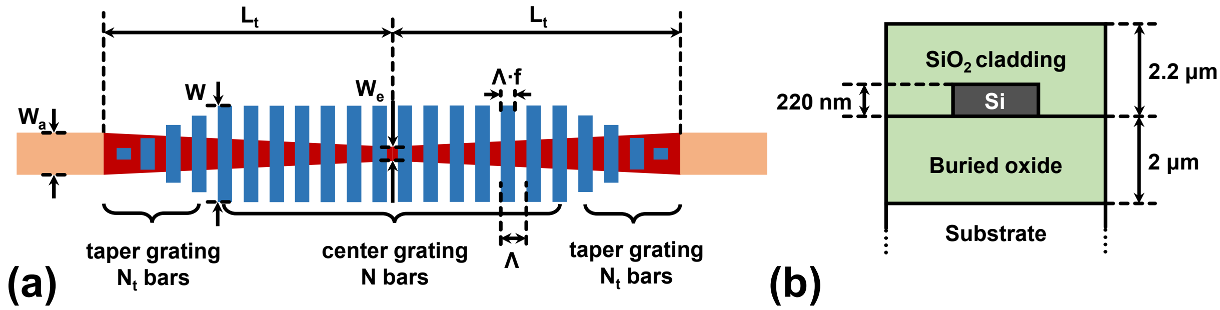

Figure 4.1: (a) Schematic of the proposed grating-based TM-pass polarizer. Note that different colors are used to distinguish the access waveguide, the tapered waveguide, and the gratings. They are all in the same silicon layer of the SOI platform. (b) Cross-section of the SOI waveguide. The device is designed on such a standard platform with a 220 nm silicon layer and a silicon oxide top cladding.

We design the TM-pass polarizer on a standard SOI platform with a 220-nm-thick silicon layer on a 2 μm BOX layer, with silicon dioxide cladding on top. The schematic of our proposed device is displayed in Fig. 4.1. Basically, the gratings-based TM-pass polarizer consists of tapered strip waveguides (red) and grating waveguides (blue). Starting at the end of the access waveguide with a width of W_a, the waveguide width is linearly tapered from W_a to W_e with a length of L_t. Then the width is symmetrically increased back to W_a at the other end of the device. Since the device is designed for all the optical telecommunication bands, the access width W_a is preset as 350 nm so that the single-mode condition is satisfied for all targeted wavelengths. The grating waveguides with the pitch Λ and the fill factor f are placed on where the strip waveguide is tapered. The gratings can be divided into three sections as indicated in Fig. 4.1. The center section is a grating waveguide containing N bars with a width of W. On both sides, we introduce a taper grating with N_t bars. The widths of the grating bars evolve linearly from 0 to $W(N_\mathrm{t}-1)/N_\mathrm{t}$ so that the adjacent bars maintain a constant width difference, W/N_t. Such taper designs ensure the adiabaticity of the grating waveguide and the confinement of the mode, therefore minimizing the coupling and propagating loss of the TM mode. Under such definitions, the taper length L_t becomes a function of the grating parameters rather than an arbitrary value. The device length L, which equals to $2L_\mathrm{t}$, can then be expressed as:

$$L = 2L_\mathrm{t} = (2N_\mathrm{t} + N - 1)\Lambda. \tag{4.1}$$

It is revealed in [68, 108] that 1-dimensional gratings can work under 3 types of regimes, namely diffraction, reflection and subwavelength. The operation regime of a certain grating depends on the ratio between the pitch (Λ) and the free space wavelength (λ_0) of the incident light. In order to make the device functional, the TE-polarized light has to be reflected by the grating as a Bragg reflector, while the grating is working under the subwavelength regime for TM mode. Specifically, the following two conditions should be satisfied simultaneously:

$$n_\mathrm{B}^\mathrm{TE}\Lambda = n_\mathrm{w}^\mathrm{TE}\Lambda f + n_\mathrm{n}^\mathrm{TE}\Lambda(1-f) = \lambda_0/2, \tag{4.2}$$

$$n_\mathrm{B}^\mathrm{TM}\Lambda = n_\mathrm{w}^\mathrm{TM}\Lambda f + n_\mathrm{n}^\mathrm{TM}\Lambda(1-f) < \lambda_0/2, \tag{4.3}$$

where n_B is the effective index of the Bloch mode, and n_w and n_n stand for the effective indices of the waveguide modes in the wide (W) and the narrow (W_e) sections. Note that Eqs. (4.2) and (4.3) are used only as a rough starting point in the design process since a tapered structure is applied. Still, it can be implied from the equations that the key to the design of broadband TM-pass polarizers is to expand the gap between the effective indices of TE and TM modes.

4.2.2 Geometries optimization

Since the TE mode effective index in a strip SOI waveguide is more sensitive to width change than that of the TM mode, we firstly study the dependence of operation bandwidth on W. W is swept from 700 nm to 1500 nm with a step of 200 nm. The other parameters are determined with rough estimations. $\Lambda = 320$ nm, $f = 0.6$, $W_{\mathrm{e}} = 110$ nm are chosen so that the center wavelength of the Bragg reflector is near 1500 nm. N_{t} and N are both temporarily set as 20. The performance is evaluated by 3-D FDTD simulation, where we extract the transmission and reflection spectra of both TE and TM modes covering a 500 nm wavelength range from 1200 nm to 1700 nm.

According to the TE mode reflection spectra shown in Fig. 4.2(b), the upper cutoff frequency (3 dB) of the Bragg reflection regime moves from 1494 nm to 1637 nm when W changes from 700 nm to 1500 nm. Meanwhile for the TM mode, the range of Bragg reflection is rather insensitive to the width variation. It can also be observed that the range of the bandgap (Bragg reflection regime) under the TE mode cannot be effectively expanded by the increase of W. If one only utilizes this bandgap, the polarizer will not achieve an ultra broadband operation.

However, it is interesting to see that the TE mode transmission on the left-hand side (shorter wavelengths) of the bandgap is also suppressed when W is increased. For example, when $W = 1300$ nm, the TE mode transmission is below -10 dB within the wavelength range [1200 nm, 1635 nm]. Judging by the TE mode reflection spectrum in Fig. 4.2(b), the Bragg reflection regime only covers [1371 nm, 1620 nm] (3 dB bandwidth). While in Fig. 4.2(a), the TM mode transmission with $W = 1300$ nm is higher than -1 dB within the band [1279 nm, 1700 nm]. Therefore, the device still functions as a TM-pass polarizer between

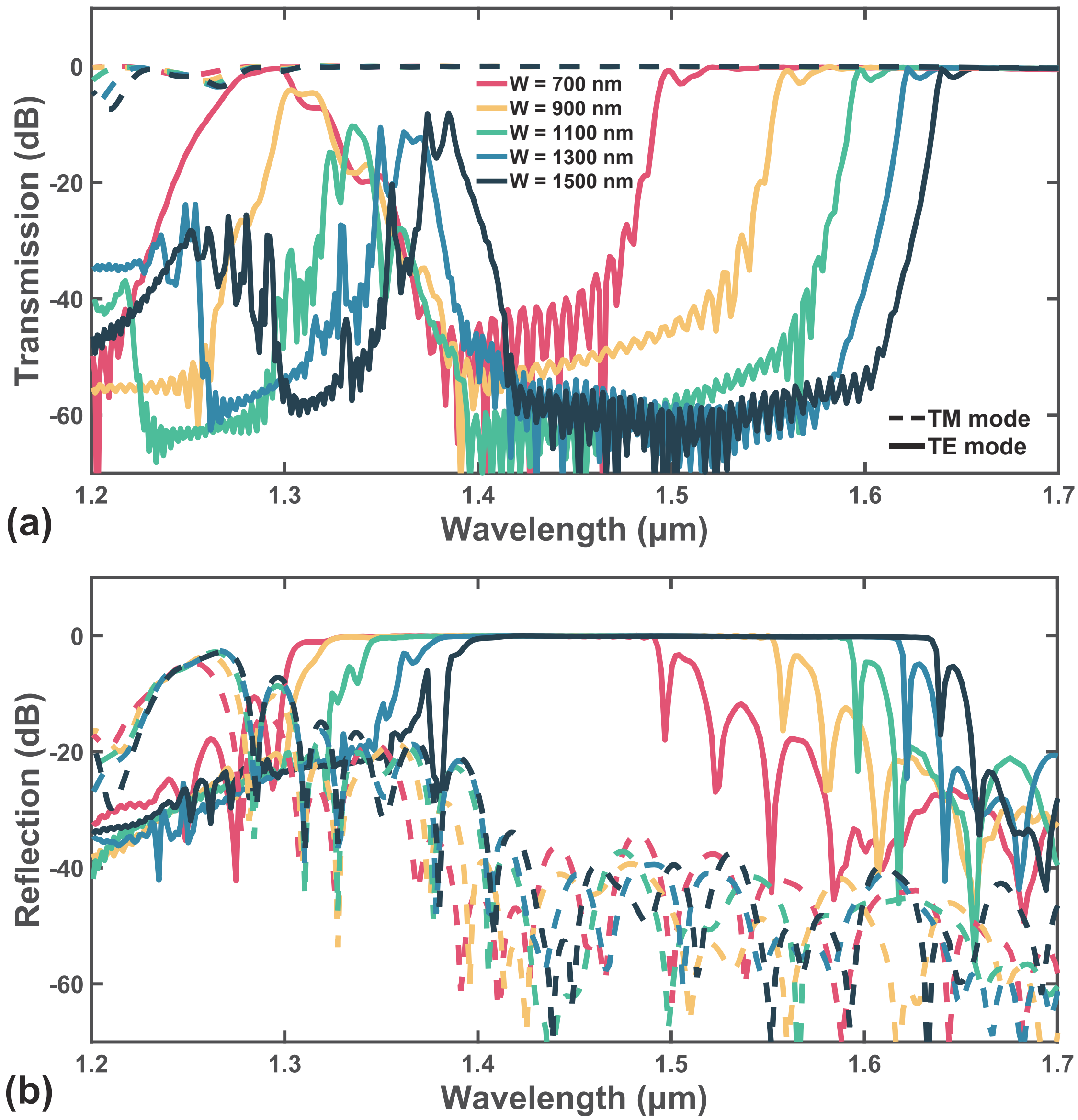

Figure 4.2: Calculated (a) transmission and (b) reflection spectra of both TE and TM modes with different grating widths.

$\lambda_0 = 1279$ nm and $\lambda_0 = 1371$ nm. Such bandwidth extension is the fundamental cause of the broader operation band compared with other reported TM-pass polarizers based on periodic structures. This will be explained with details later.

A problem with wide gratings is that the grating waveguide supports multi modes rather than a single mode. If we compare $W = 1300$ nm and $W = 1500$ nm, we will notice that the compression of TE mode transmission on the left-hand side of the reflection regime is slightly worse with $W = 1500$ nm. Since the length of the taper is the same, it is inferred that high order modes (TE1, TE2, ...) tend to be excited with a wider grating. Moreover, high order modes have smaller effective indices than the fundamental mode (TE0). Thus they can still go through the grating at shorter wavelengths according to equation (4.2). Consequently, we determine $W = 1300$ nm.

Following the analysis of the potential excitation of high order modes in the proposed device, one can see that the grating taper length, equivalently N_t, is an important parameter to optimize. Therefore the device performances are evaluated with 5 different N_t ranging from 10 to 30. Before the sweep, the geometries of the grating are marginally adjusted to achieve the desired operation bands. Specifically, the TM mode is required to work under the subwavelength regime with $\lambda_0 > 1260$ nm (the start of O-band), and the TE mode should be blocked with $\lambda_0 < 1625$ nm (the end of L-band). As a result, Λ is set to 318 nm and f is set to 0.675. Note that a larger fill factor f results in a redshift of the TE mode spectrum which extends the bandwidth. However, f cannot be too close to 1 as the gap size will be reduced, and it becomes harder to fabricate such small features. Thus, $f = 0.675$ is the result of this trade-off so that the minimum feature is still larger than 100 nm.

Figure 4.3 shows the calculated device performance with different taper lengths. Here we use IL and PER as the performance indicators, which are defined as follows:

$$\mathrm{IL} = -10 * \log_{10}(T^{\mathrm{TM}}), \tag{4.4}$$

$$\mathrm{PER} = 10 * \log_{10}(T^{\mathrm{TM}}/T^{\mathrm{TE}}), \tag{4.5}$$

where T^{TM} and T^{TE} are the transmission of TM and TE mode through the device, respectively.

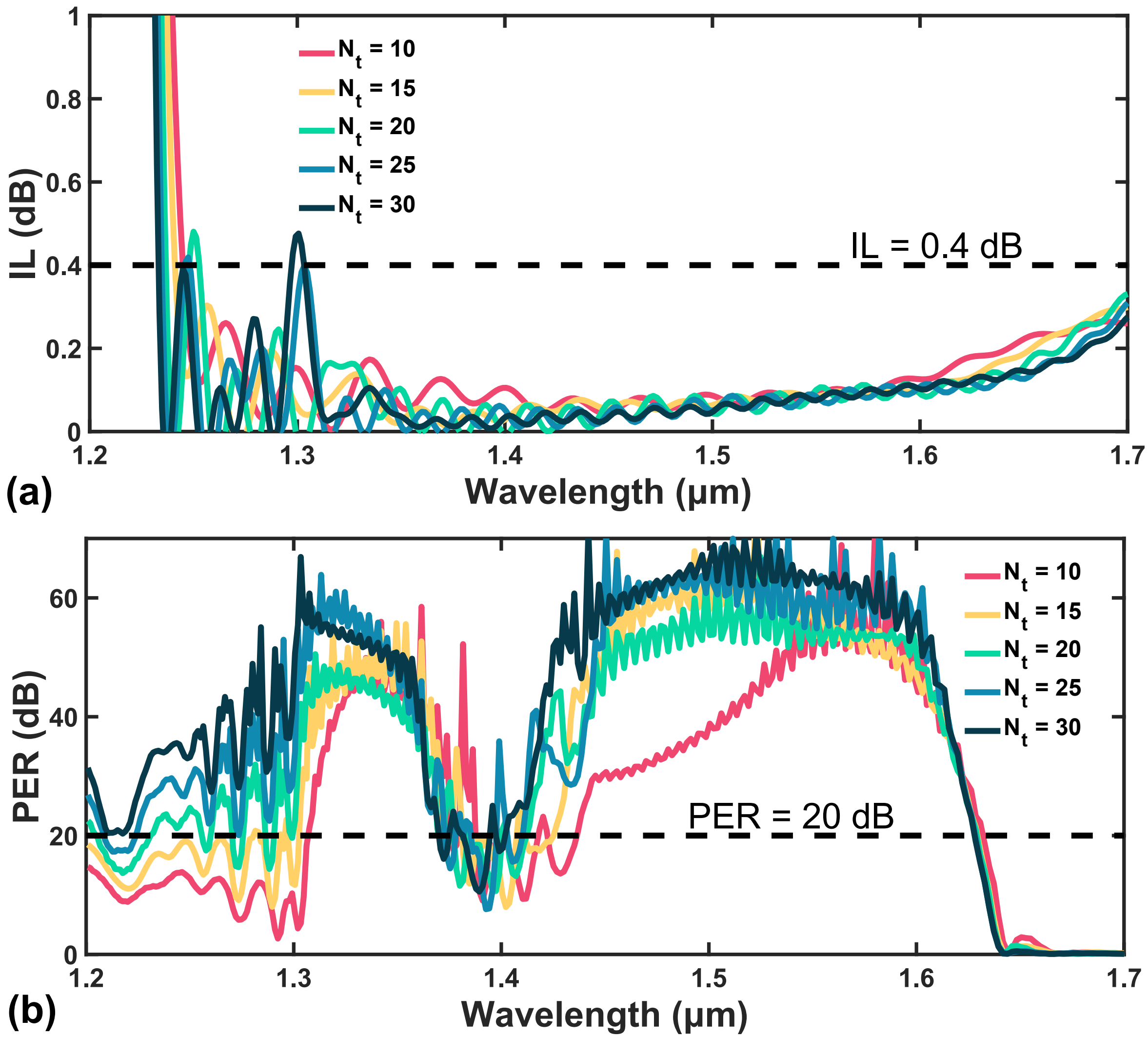

Figure 4.3: Calculated (a) IL and (b) PER spectra with various N_t at $W = 1300$ nm. The PER in O-band is increased by extending the taper.

Simulation results shown in Fig. 4.3 indicate that an increase in grating taper length effectively reduce the transmission in O-band without affecting the overall bandwidth. Accordingly, $N_t = 25$ is determined since it is large enough to keep the PER above 20 dB in the whole O-band, and it makes a compact device with a footprint of only 21.942 μm. Under the finalized parameters, the device achieves < 0.4 dB IL and > 7.5 dB PER over a

390 nm band from 1245 nm to 1635 nm. Benefiting from the aforementioned taper designs, the IL is very low over such a wide band. However, the minimum PER is relatively low, which originates from the notch around $\lambda_0 = 1400$ nm. Nonetheless, we manage to locate the notch in E-band (not commonly used) from 1372 nm to 1410 nm by choosing W and f carefully, so that PER is higher than 20 dB outside this wavelength range.

4.2.3 Further exploration of device principle

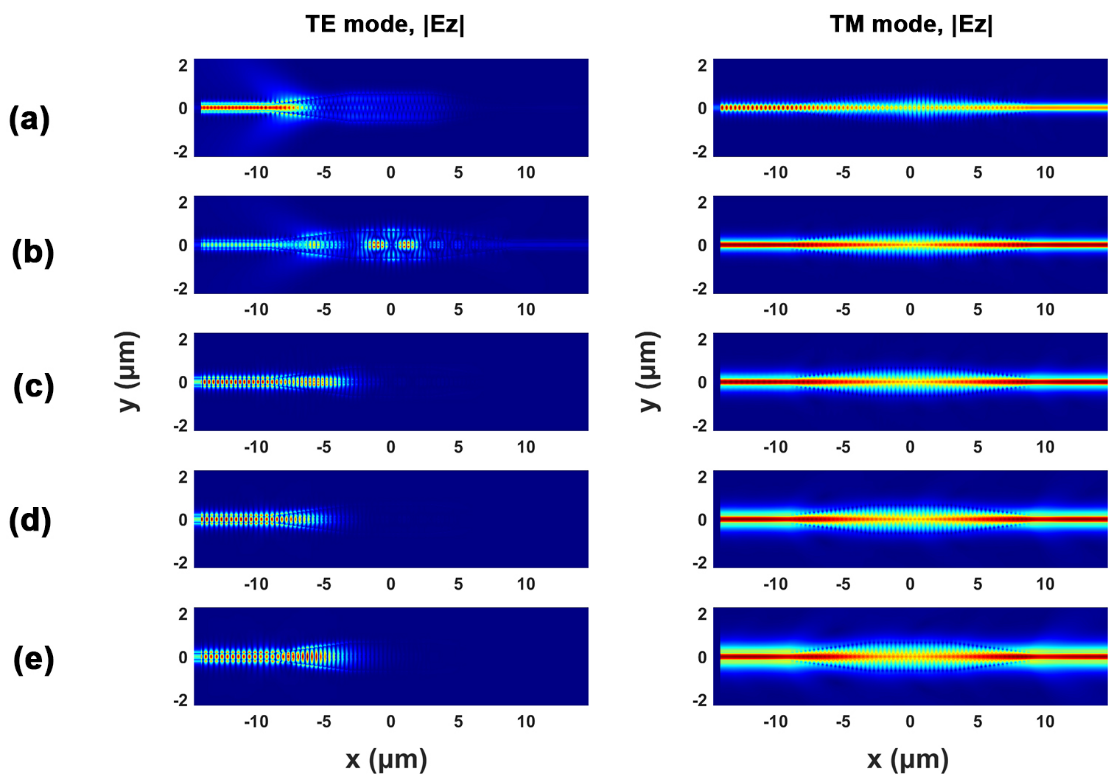

Figure 4.4: Normalized electric field distributions of both TE and TM modes at $\lambda_0 =$ (a) 1300 nm, (b) 1375 nm, (c) 1450 nm, (d) 1525 nm, (e) 1600 nm.

To better understand the principle of the device, we calculate and exhibit in Fig. 4.4(a-

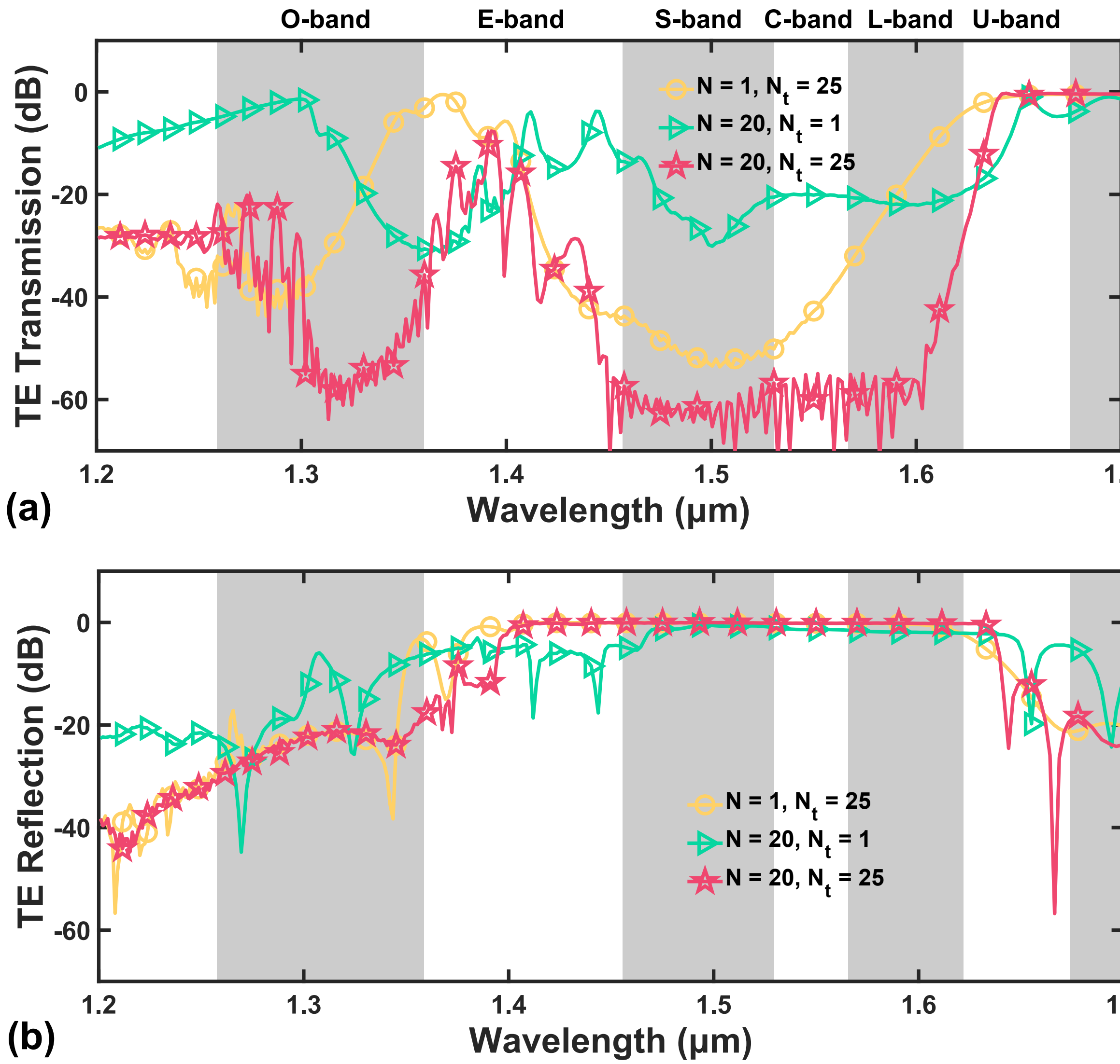

Figure 4.5: Calculated TE mode (a) transmission and (b) reflection spectra of 1) the proposed device, 2) the device without taper gratings and 3) the device without the center grating. The results show that the taper gratings actually contribute to the bandwidth extension in O-band.

e) the electric field distributions of light propagating through the device at 5 wavelengths: 1300 nm, 1375 nm, 1450 nm, 1525 nm and 1600 nm. For 1450 nm - 1600 nm, the light is reflected by the grating according to the field distributions, while at $\lambda_0 = 1300$ nm one can observe that the the light is diffracted. However, the diffraction emerges at the taper gratings rather than the center grating. To figure out the function of the taper gratings, three different device configurations are compared. In the first configuration, N is set to 1 so that the structure only contains taper gratings with $2N_\mathrm{t} + 1 = 51$ bars. For the second test, N_t is chosen as 1 while N is set back to 20. The original set of parameters are used as a benchmark, becoming the third setting. The calculated TE mode transmission and reflection spectra of the three configurations are demonstrated in Fig. 4.5.

By the O-band transmission shown in Fig. 4.5(a), if no taper grating is used, the center grating with uniform widths cannot effectively block the TE mode light with $\lambda_0 < 1330$ nm. On the contrary, the device that only contains the taper gratings show similar performance as the benchmark device around O-band. Since both transmission and reflection are limited, it can be determined that the proposed device works under a diffraction regime, and this regime actually arises from the taper gratings. On the other hand, the center grating is also crucial because it extends the bandgap and improves the performance where the TE mode is reflected. In short, the smooth combination of the taper and center gratings successfully extends the operation bandwidth by multiplexing the diffraction regime with the Bragg reflection for the TE mode, while maintaining low loss for the TM mode.

Wavelength range	1245 nm - 1372 nm	1410 nm - 1626 nm
Regime for TE mode	diffraction	reflection
Regime for TM mode	subwavelength	subwavelength
Main functional section	taper gratings	center grating

Table 4.1: A summary of the grating-regimes multiplexing as the primary device principle

To conclude, we have designed an all-silicon TM-pass polarizer with simulation that covers [1245 nm, 1372 nm] $\cup$ [1410 nm, 1626 nm], with IL < 0.4 dB and PER > 20 dB. The 343 nm operation band includes O-, S-, C-, L- bands, and part of E- band. The broadband feature is achieved by multiplexing different regimes with different sections of the structure, and details can be discovered in Table 4.1. One should be aware that the performance can be further improved if we increase N_t or W, at a cost of larger size and longer delay. In the next section, we report the experimental results for the current set of parameters as a proof of concept.

4.3 Fabrication and characterization

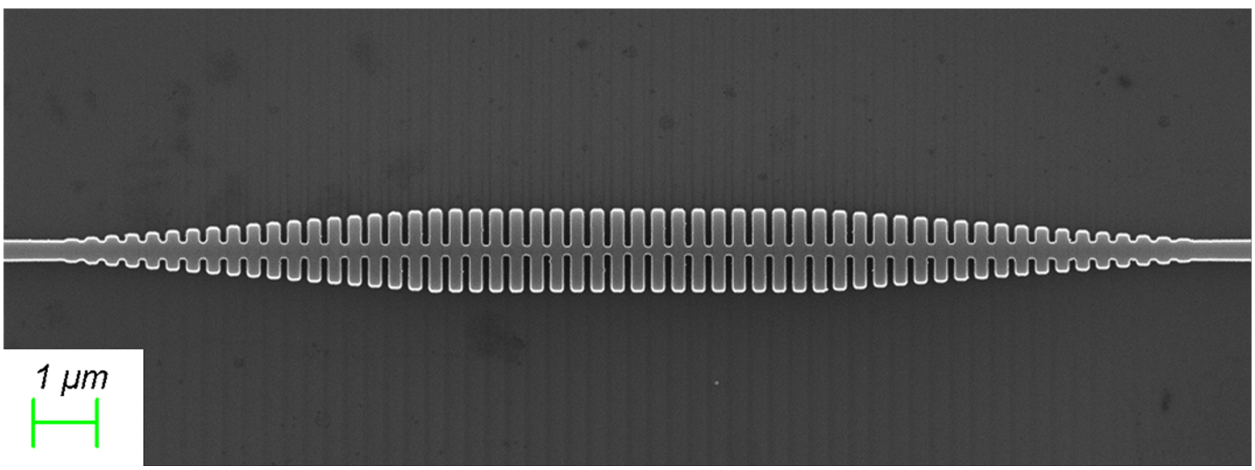

Figure 4.6: SEM image of the fabricated TM-pass polarizer.

The device is fabricated by the NanoSOI fabrication process provided by Applied Nanotools Inc. The wafer is a standard 220 nm SOI platform with a 2.2-μm-thick top cladding oxide. The SEM image of the device is displayed in Fig. 4.6. For test purposes, we apply broadband vertical grating couplers [114–116] to connect the device-under-test (DUT) with our measurement system. The testing setup is the similar to Fig. 3.9. In addition, an isolator is placed before the PC to eliminate the reflected light. Since the device works from O- to C-, L-bands, and the grating couplers are designed only for a single band and a single polarization, four measurements need to be performed for one device (TE/O, TM/O, TE/C, TM/C). Limited by the wavelength range of the tunable lasers, we obtain the transmission spectra of both TE and TM modes within the ranges [1260 nm, 1360 nm] and [1500 nm, 1630 nm]. In each measurement set, two back-to-back connected grating couplers are fabricated near the DUT for normalization.

Because the simulated IL for the TM mode is relatively low, 20 copies of the device are cascaded as the DUT in the TM mode characterization, then the IL is calculated as the one-twentieth of the overall loss in dB.

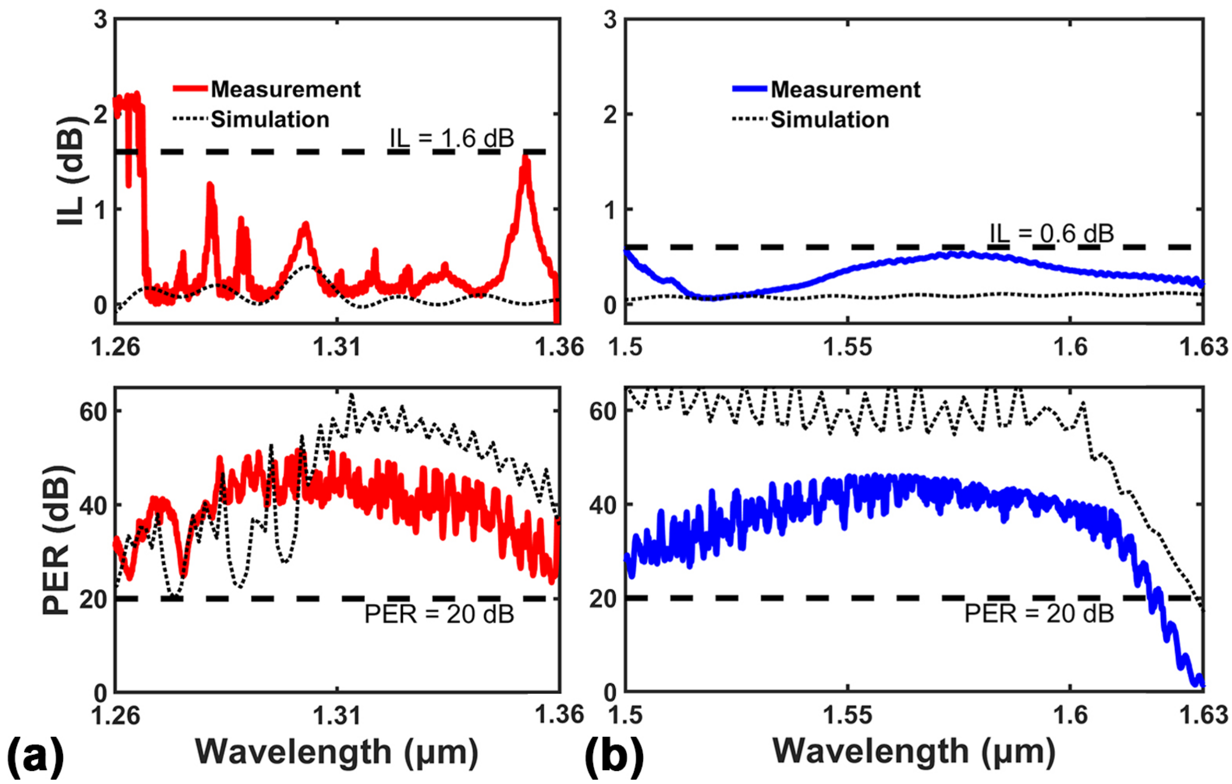

Figure 4.7: Measured IL and PER spectra from (a) 1260 nm to 1360 nm, and from (b) 1500 nm to 1630 nm. Calculated IL and PER spectra are displayed in dotted lines as references.

The measured IL and PER spectra are shown in Fig. 4.7, along with the calculated data as a reference. The IL is below 0.6 dB from 1500 nm to 1630 nm, while in O-band one can observe the edge of the Bragg reflection regime at $\lambda_0 = 1265$ nm, which is a slight redshift (˜20 nm) from the simulation. For 1265 nm $< \lambda_0 <$ 1360 nm the maximum measured IL is

1.6 dB. Note that there are several notches in the O-band IL spectrum. As reported in Fig. 4.2(b), the TM mode reflection becomes intense in O-band since it is close to the reflection regime. It is then inferred that the cascade of devices forms a series of Fabry-Pérot cavities that result in the notches. Therefore, one can estimate the actual single-device ILs more optimistically around those maxima. Regarding the TE mode performance, PER > 20 dB is achieved over all the measurable wavelengths except for $\lambda_0 > 1617$ nm. In simulations, the cutoff wavelength with the same PER threshold is 1626 nm. The 9 nm gap may be caused by over-etching in the fabrication process. Still, the measured PERs are in accordance with simulated values.

4.4 Conclusion

In summary, we have demonstrated an all-silicon TM-pass polarizer that operates in multiple optical telecommunication bands. The grating-based device utilizes polarization-dependent grating regimes to block the TE mode while remaining transparent to the TM mode. Firstly, a wide grating at the center is applied to enhance the birefringence so that the TM mode is under subwavelength regime for all-optical bands (¿ 1.26 µm) while the grating works as a Bragg reflector with TE mode for S-, C- and L-bands. Moreover, it is revealed that taper gratings with increasing widths can cause the O-band TE-polarized light to diffract as well. Therefore, the proposed tapered structure is able to extend the operation bandwidth by multiplexing the diffraction and reflection regimes for TE mode. With 3-D FDTD simulation, the device achieves IL < 0.4 dB and PER > 20 dB over [1245 nm, 1372 nm] ∪ [1410 nm, 1626 nm] (343 nm band in total) using a ˜22-µm-long structure. The operation band covers the whole O-, S-, C- and L- bands, which are mostly employed in practical optical communication systems. The proposed device has been fabricated and characterized. Experimental results indicate IL < 1.6 dB and PER > 20 dB from 1265 nm to 1360 nm, and IL < 0.6 dB and PER > 20 dB from 1500 nm to 1617 nm. The measured spectra prove that the device functions well over most targeted wavelengths. Last but not least, the device is designed on a standard 220 nm SOI with oxide cladding, so that it is endowed with compatibility to numerous active/passive silicon photonics components. To the best of our knowledge, this is one of the largest bandwidth achieved with such a standard platform for all-silicon TM-pass polarizers. Plus the single-etch structure and a minimum feature size larger than 100 nm, our proposed device contributes towards the development of practical multi-band PICs.

Chapter 5

Silicon single-mode waveguide crossing covering all optical communication bands

5.1 Motivation

Considering the single-layer characteristic of the standard SOI platform, waveguide crossings are inevitable for on-chip routing. With the ever-increasing density and complexity of PICs, low-loss silicon waveguide crossings are playing an increasingly important role in circuit design, e.g. large-scale silicon photonics switches [117, 118] and routing systems [119, 120].

Multiple structures have been proposed to achieve low-loss waveguide crossings on SOI. Vertical-coupling-based structures reduce the loss of crossings [121–123], however at the expense of increased fabrication complexity. MMI couplers have been utilized to decrease the loss of crossings while maintaining simplicity in fabrication [124–126]. With advanced design algorithms including PSO [127, 128] or Levenberg-Marquardt update [129], the loss per crossing can be reduced to <0.1 dB within C-band (1530 - 1565 nm). Moreover, it has been shown that a 1-D Gaussian beam can be synthesized by carefully manipulating the two or three lowest even-order modes to further minimize the insertion loss of a waveguide crossing [130, 131]. Such delicate designs achieve insertion losses <0.01 dB at optimum wavelengths.

Up to now, however, there is no previous study that has investigated an ultra-broadband low-loss single-mode waveguide crossing that covers multiple optical communication bands. For the past years, researchers have demonstrated such broadband designs of various SOI-integrated photonics devices including PBS [132], polarizers [5, 109, 110, 133], polarization rotators [134], and 3-dB couplers [135]. These designs cover multiple or all optical communication bands (O-, E-, S-, C-, L-, and U-bands). Although broadband operation has been shown with multi-mode waveguide crossing [136], it is not practical for single-mode applications since a long taper is needed to convert single-mode waveguide to multi-mode waveguide.

Therefore, the design we propose in this chapter aims to fill the gap in this area by proposing a broadband low-loss waveguide crossing on the SOI platform that covers all optical communication bands. Such a design would facilitate the development of multi-band PIC by expanding the broadband SOI device library.

As one of the commonly adapted structures for waveguide crossing, the MMI coupler makes use of the self-image effect to confine the modal electric field at the intersection. Despite the fact that MMI couplers are relatively broadband, it is shown in [124] that within a 60 nm band (1520 nm - 1580 nm) the measured IL per crossing varies by ˜0.2 dB. Similarly in a polarization insensitive crossing design based on MMI [126], the highest IL over a 90 nm band (1520 nm - 1610 nm) is ˜0.2 dB more than that of the center wavelength 1550 nm for the transverse-electric (TE) mode. Even with the state-of-art optimization algorithms such as the Levenberg-Marquardt updates [129], one can observe that the IL declines to 0.5 dB with ˜230 nm bandwidth in simulation. Note that it is possible for such approaches that the performance over a large bandwidth can be improved by modifying the definition of FOM, yet it has not been demonstrated.

In this chapter, we adopt a different idea to achieve the ultra-broadband operation. It is known that the large loss of a direct intersection of single-mode SOI waveguide stems from the high index contrast between the silicon core and the oxide cladding. The high contrast causes wide-angle spatial components in the mode that radiate away when the light enters the intersection area. In [137], a shallow-etched lateral cladding is introduced to decrease the index contrast, decreasing the IL to 0.16 dB. However, shallow-etch adds cost and complexity to fabrication. Hence, this paper proposes a single-layer design using an anisotropic metamaterial as the lateral cladding with simplified fabrication. The adopted metamaterial is the SWG [68,138,139]. The SWG consists of periodic structures with periods much smaller than the wavelength of the incident light. Since SWG exhibits capabilities in refractive index engineering and dispersion management, it adds degrees of freedom to the design and benefits various types of integrated photonic devices. The use of SWG has been reported in various fields, such as integrated devices in optical communication bands [139–141] and different types of chip-scale sensing [142–145]. Specifically for the topic of this work, SWG has been demonstrated in SOI waveguide crossings [72, 136, 146, 147] to maximize the transmittance. Besides index engineering, the anisotropic feature of the SWG has also been utilized to achieve ultra-broadband polarization handling on SOI [109,132]. Our work is also inspired by the anisotropic modeling of the metamaterial. Similarly in [148–150], graphene-embedded silicon waveguides are adopted to achieve broadband TE-pass polarizers and PSRs where the key factor is the graphene treated as an anisotropic metamaterial.

Unlike MMI-coupler-based crossings, such a design avoids the excitation of higher-order modes and then benefits the performance over a large range of wavelengths.

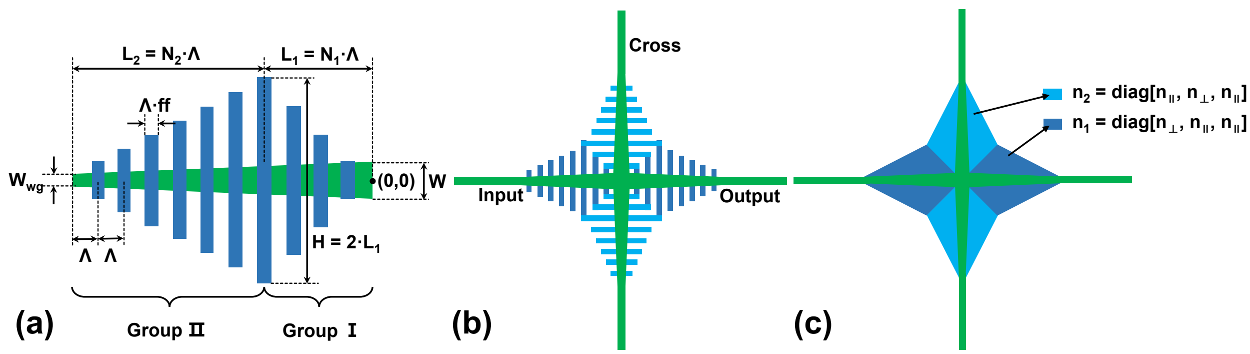

Figure 5.1: The schematics of the initial design. (a) Parameter definitions of a single arm. (b) The overall structure. (c) The illustration of how the SWG is regarded as anisotropic homogeneous mediums.

5.2 Design and simulation

5.2.1 Initial design

The initial schematic is shown in Figure 5.1. Since the proposed structure has 4-fold symmetry, we first define one of the four arms as in Figure 5.1(a), then it can be expanded to its complete form in Figure 5.1(b). The basic component of the arm is a linearly tapered strip waveguide with a length of L, where the width changes from the W_{wg}, the width of the connecting single-mode waveguide, to W at the intersection point (0,0). On top of it, two groups of SWG with the same pitch Λ and fill factor f are placed as the lateral cladding. Starting from the left-hand end, group II consists of N_2 periods of SWG, with linearly increasing height from 0 to H, while the following group I contains N_1 periods with decreasing height from H to 0. It consequently implies that $L = L_1 + L_2 = (N_1 + N_2) * \Lambda$.

If the SWG is regarded as an anisotropic homogeneous medium as demonstrated in Figure 5.1(c), there are in fact two types of metamaterials due to the two different orientations of SWG [68, 151].

The diagonal relative permittivity tensors are given by [132]:

$$\varepsilon_1 = \mathrm{diag}[\varepsilon_1^{\mathrm{xx}}, \varepsilon_1^{\mathrm{yy}}, \varepsilon_1^{\mathrm{zz}}] = \mathrm{diag}[n_\perp^2, n_\parallel^2, n_\parallel^2], \tag{5.1}$$

$$\varepsilon_2 = \mathrm{diag}[\varepsilon_2^{\mathrm{xx}}, \varepsilon_2^{\mathrm{yy}}, \varepsilon_2^{\mathrm{zz}}] = \mathrm{diag}[n_\parallel^2, n_\perp^2, n_\parallel^2], \tag{5.2}$$

where the indexes of parallel and perpendicular polarization can be expressed (with zero-order approximation) as follows [68, 152]:

$$n_\parallel^2 = ff \cdot n_{\mathrm{Si}}^2 + (1 - ff) \cdot n_{\mathrm{SiO_2}}^2, \tag{5.3}$$

$$\frac{1}{n_\perp^2} = \frac{ff}{n_{\mathrm{Si}}^2} + \frac{1 - ff}{n_{\mathrm{SiO_2}}^2}, \tag{5.4}$$

We create 4 copies of the single arm via rotating it around the intersection point by 0°, 90°, 180°, and 270°, respectively. The combination of all 4 copies then forms the proposed structure. In order to properly connect the copies, the maximum SWG height H is set to $2 \cdot L_1$. One detail to notice here is that the heights of SWG in group II need to be slightly extended by $\Lambda \cdot ff$ to avoid unmanufacturable small feature sizes. Since $n_{\mathrm{SiO_2}} < n_\parallel < n_{\mathrm{Si}}$, $n_{\mathrm{SiO_2}} < n_\perp < n_{\mathrm{Si}}$, a low-index-contrast waveguide profile is then created near the intersection area. In [137], it is stated that a low refractive index contrast reduces the diffraction loss and the back reflection in the non-confined area, hence the crossing region. Therefore with proper optimization of the SWG, the index can be finely engineered to maximize the transmission and minimize the crosstalk.

Prior to optimizing the geometries of the device, several parameters can be preset. Λ is

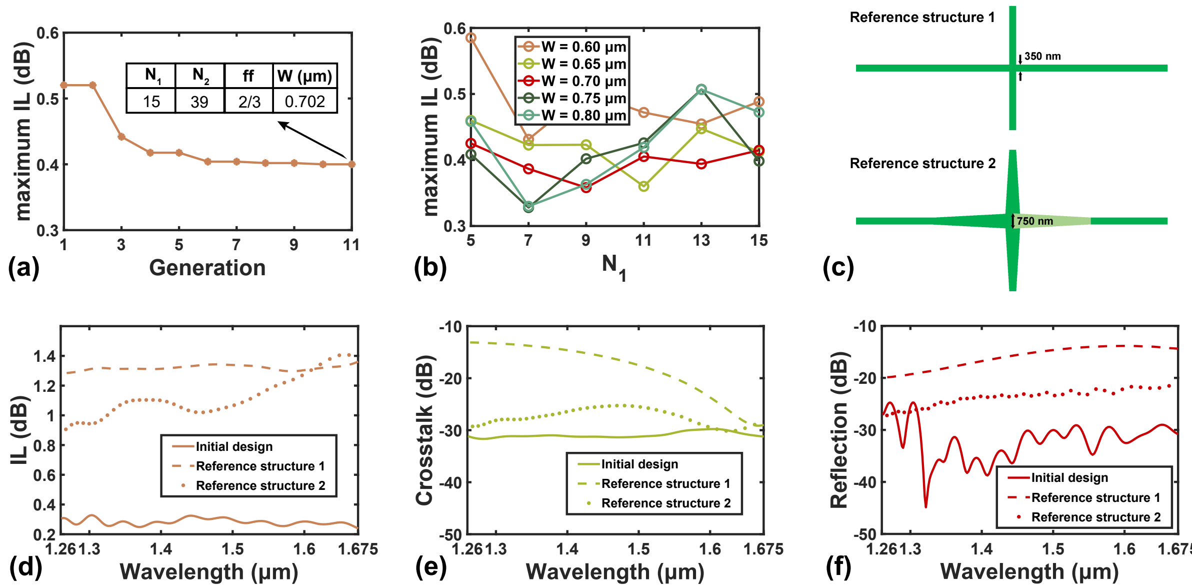

Figure 5.2: The simulation results of the initial design. (a) FOM trend of the PSO with the initial design. (b) Dependence of maximum IL on W and N_1. (c) Schematics of two reference waveguide crossing structures (d-f) Calculated spectra of (d) IL, (e) crosstalk, and (f) reflection of the device with optimized geometry, along with the results of both reference structures in (c).

set to 0.180 μm to ensure that the gratings work within the subwavelength regime at every target wavelength, of which the range is [1260 nm, 1675 nm]. We set $W_{\mathrm{wg}} = 350$ nm so that the single-mode condition of the connecting waveguide is fulfilled for all the bands. In order to search for a global best FOM, we initially utilize PSO in 3-D FDTD simulations with large mesh sizes to efficiently find suboptimal parameters, and then we carry out sweeps on key device geometries with finer meshes. We specifically use the Ansys Lumerical FDTD solver along with the built-in PSO algorithm to conduct the simulations. Note that the proposed devices work at TE mode, and are optimized with TE-mode simulations.

Commonly, the IL, the crosstalk, and the reflection are all important targets to optimize in the design process of a crossing. They are defined as:

$$\mathrm{IL} = -10 * \log_{10}(P_{\mathrm{out}}/P_{\mathrm{in}}), \tag{5.5}$$

$$\mathrm{Crosstalk} = 10 * \log_{10}(P_{\mathrm{cross}}/P_{\mathrm{in}}), \tag{5.6}$$

$$\mathrm{Reflection} = 10 * \log_{10}(\hat{P}_{\mathrm{in}}/P_{\mathrm{in}}), \tag{5.7}$$

where P_{in} is the input power, P_{out} is the power from the output port, P_{cross} is the power from the cross port, and $\hat{P}_{\mathrm{in}}$ is the reflected power from the input port.

In our optimization process, the FOM is defined as the maximum IL over the whole wavelength range, i.e. we temporarily ignore the crosstalk and the reflection in the optimization. The parameter space is shown in Table 5.1. Note that for N_1 and N_2, since the PSO runs in continuous variable space, we set the final value as $ceil(N_1)$ and $ceil(N_2)$. The PSO runs with 30 generations and a generation size of 10.

Parameters	N_1	N_2	ff	W (µm)
Lower bounds	5	20	1/3	0.400
Upper bounds	15	39	2/3	1.00

Table 5.1: Ranges of parameters in PSO for the initial design

The simulation results are shown in Figure 5.2. Having conducted PSO, the FOM converges to 0.400 dB after 11 generations according to Figure 5.2(a), where the parameters at the last generation are also shown. In such a multivariate optimization task with little a priori information, the PSO proves to be an efficient tool to provide the designer with a decent starting point for further optimization.

For the next step of optimization, we perform parametric sweeps rather than PSO, and the number of mesh points per wavelength increases from ~10 to ~14 for more accuracy. We firstly fix $N_2 = 39$ and $ff = 2/3$. The reason for fixing N_2 is that the SWG of group II

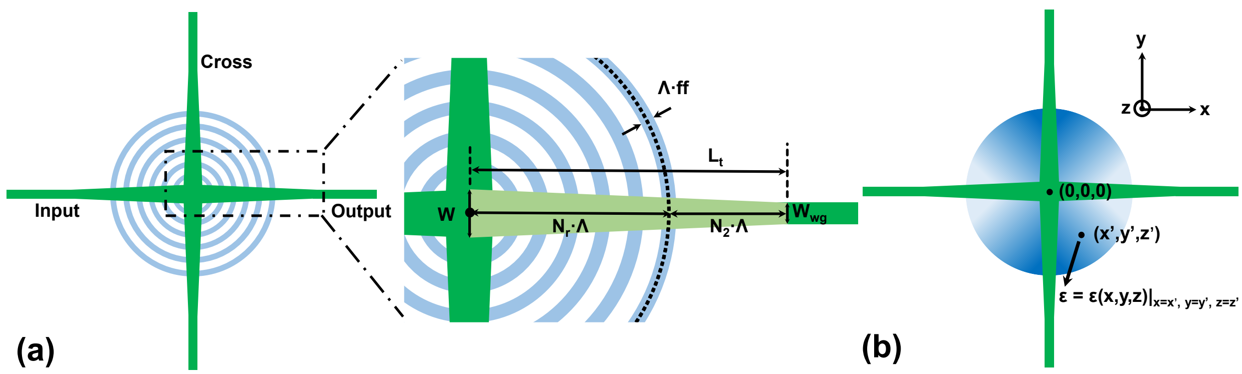

Figure 5.3: The schematics of the improved design. (a) The overall structure and specific parameter definitions. (b) The illustration of how the SWG is regarded as an anisotropic homogeneous medium with gradually changing relative permittivity tensors.

acts as a taper structure from strip waveguide to waveguide with SWG cladding. Therefore when N_2 is large enough, it mainly determines the footprint of the device rather than the performance. Meanwhile, the fill factor ff reaches the upper bound 2/3 after convergence, and it is not feasible to further increase the value due to the 60 nm minimum feature size of the fabrication process. Therefore ff is also fixed as the upper bound to simplify the following optimization.

Then the device under various combinations of N_1 and W are evaluated by simulation. The results are displayed in Figure 5.2(b). It is inferred that the PSO only reaches a local optimum, since the best FOM is achieved at $N_1 = 7$ and $W = 0.750$ µm. The detailed device performances, including the IL, the crosstalk, and the reflection, are shown in Figure 5.2(d), (e), and (f) as functions of wavelength. The IL over the 415 nm wavelength ranges from 0.237 dB to 0.328 dB, indicating a broadband operation. As for the crosstalk and the reflection, although they are not considered during the optimization, crosstalk <-29 dB and reflection <-24 dB are achieved. To better prove the functionality of SWG over the whole bandwidth, we also simulate two reference structures as shown in Figure 5.2(c). Reference structure 1 is a direct waveguide crossing of 350-nm wide waveguide, while reference 2 is a crossing with linear tapers from 350-nm to 750-nm widths. Reference 2 can also be formed by removing the SWG cladding in the initial design. Their simulation results are displayed in Figure 5.2(d), (e), and (f) as benchmarks. The calculated results prove the validity of the proposed design with lateral SWG cladding, as the device maintains decent performance over all the optical communication bands, compared to direct crossings without the SWG.

5.2.2 Improved design

Although the initial structure has shown broadband features, there are several weaknesses about it. First of all, a long taper (group II SWG) is needed to achieve better performance, which increases the device footprint. Besides, the mode profile tends to change quickly as the light propagates near the intersection, because a 45°interface is inevitable between the two mediums as shown in Figure 5.1(c). Compared to the angle of common linear tapers on SOI, 45°is considered large and is likely to increase the loss of the device.

Hence, an improved design of SWG-based crossing is proposed. Instead of 1D SWG, we adopt a curved SWG to fill the lateral cladding region. As demonstrated in Figure 5.3(a), it basically consists of four tapered strip waveguides with length L_{t} for the four arms. The taper width alters linearly from W_{wg} to W, the same as the initial design. Then N_{r} rings with the same width of $\Lambda \cdot ff$, all centered at the intersection (0,0), are placed. The center radius of the n^{th} ring is defined as $r_{\mathrm{n}} = n \cdot \Lambda$, so that the gaps between adjacent rings are equal. Note that a similar definition of L_{t} is applied compared with the initial design. The length is divided into two parts, with N_{r} and N_2 grating period respectively, although the second part does not contain any SWG structures. Therefore, it is defined that $L_{\mathrm{t}} = (N_{\mathrm{r}} + N_2) * \Lambda$

as illustrated in Figure 5.3(a).

Above is how the proposed curved SWG cladding is formed. Such structure mitigates both issues in the initial design. Firstly, it avoids the use of long tapers since the structure itself has a gradually-changing geometry. Meanwhile, the curved SWG can be treated as a medium with gradually varying permittivity. If we establish a Cartesian coordinate plane as in Figure 5.3(b), the relative permittivity tensor at point (x,y,z) can be written as Equation 5.8, following the conversion rule of second-order tensors under coordinate transformations:

$$\begin{aligned}\varepsilon(x,y,z) = &\begin{bmatrix} \varepsilon^{\mathrm{xx}}(x,y) & \varepsilon^{\mathrm{xy}}(x,y) & 0 \\ \varepsilon^{\mathrm{yx}}(x,y) & \varepsilon^{\mathrm{yy}}(x,y) & 0 \\ 0 & 0 & \varepsilon^{\mathrm{zz}}(x,y) \end{bmatrix}, \\ z \in &(0, 220\ \mathrm{nm}),\end{aligned} \tag{5.8}$$

where:

$$\begin{cases} \varepsilon^{\mathrm{xx}}(x,y) = n_\perp^2 \cdot \cos^2\theta(x,y) + n_\parallel^2 \cdot \sin^2\theta(x,y), \\ \varepsilon^{\mathrm{yy}}(x,y) = n_\perp^2 \cdot \sin^2\theta(x,y) + n_\parallel^2 \cdot \cos^2\theta(x,y), \\ \varepsilon^{\mathrm{xy}}(x,y) = (n_\perp^2 - n_\parallel^2) \cdot \cos\theta(x,y) \cdot \sin\theta(x,y), \\ \varepsilon^{\mathrm{yx}}(x,y) = \varepsilon^{\mathrm{xy}}(x,y), \\ \varepsilon^{\mathrm{zz}}(x,y) = n_\parallel^2, \end{cases} \tag{5.9}$$

with $\theta(x,y) = \arctan(y/x)$. Compared with the initial design, such a model avoids rapid transition of waveguide cross section while maintaining the same functionality.

PSO with large meshes is utilized again to get suboptimal parameters as the starting point of the follow-up parameters sweep. The target parameters and their bounds are listed in the Table 5.2. Note that the SWG period Λ is also considered in the PSO for an extra degree of freedom. The generation size is adjusted from 10 to 15 to avoid local optimums, while the number of generations is reduced from 30 to 25 to accelerate the optimization

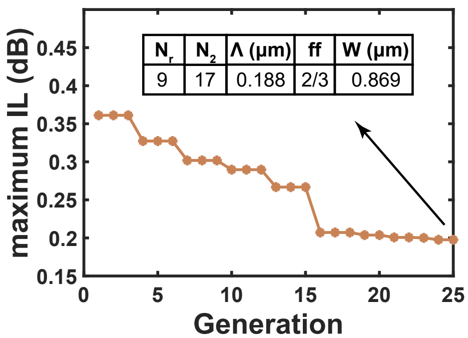

Figure 5.4: FOM trend of the PSO with the improved design.

process.

Parameters	N_r	N_2	Λ (μm)	ff	W (μm)
Lower bounds	7	5	0.180	1/3	0.400
Upper bounds	25	20	0.220	2/3	0.900

Table 5.2: Ranges of parameters in PSO for the improved design

The FOM trend during the PSO, i.e. the evolution of the maximum IL from the first to the last generation, is shown in Figure 5.4. After 25 generations, the maximum IL of the improved design over all the optical communication bands reaches 0.198 dB. With the improved design and extended parameter space, the optimized PSO demonstrates excellent optimization efficiency. The algorithm manages to decrease the FOM by 0.164 dB. The best parameter set after the convergence is listed in Figure 5.4 as well, which will be referred to in the following optimizations.

Same as the initial design, the ff also reaches the upper bound 2/3 after PSO. In the following step of optimization, although the SWG period Λ is no longer set as the constant value of 0.180 μm, the ff is still fixed as 2/3 for simplification. As for N_2, it is mostly related to the length of the taper strip waveguide. Though it is possible to further improve the performance by extending the taper, this parameter is relatively independent of the other

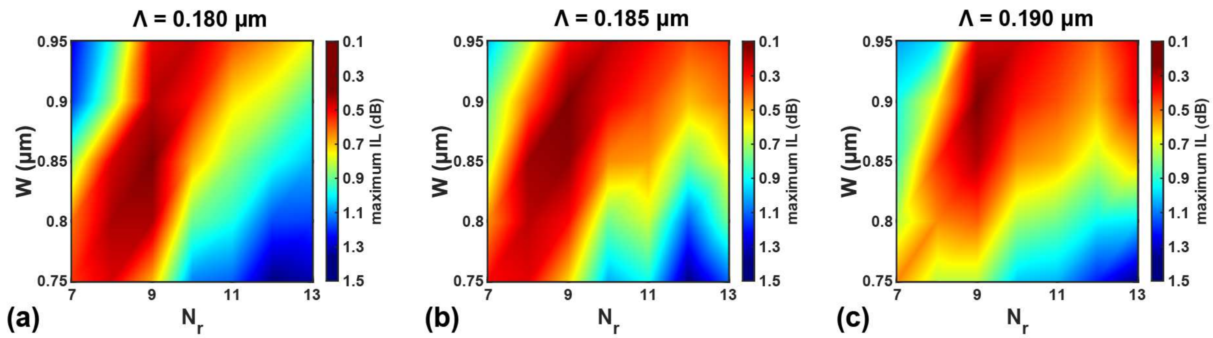

Figure 5.5: Calculated maximum IL as functions of N_{r} and W with (a) $\Lambda = 0.180$ µm, (b) $\Lambda = 0.185$ µm, and (c) $\Lambda = 0.190$ µm.

geometries. Therefore N_2 is fixed at the suboptimal value of 17, so that compact size and good performance can be achieved simultaneously.

Consequently, deciding the best set of N_{r}, W, and Λ becomes the next step. For the improved design, a more meticulous optimization flow is developed from here. Initially, a 3-D parameter sweep is conducted. The values are selected near the suboptimal parameters from the PSO listed in Figure 5.4. Specifically, $N_{\mathrm{r}} \in \{7, 8, 9, 10, 11, 12, 13\}$, $W \in \{0.750, 0.800, 0.850, 0.900, 0.950\}$ µm, and $\Lambda \in \{0.180, 0.185, 0.190\}$ µm are chosen. 3-D FDTD simulations with denser meshes are performed, and the FOM remains the maximum IL.

The results are displayed in Figure 5.5. It is reasonable to choose the geometry with the least FOM and then finalize the design. However, since the mesh accuracy can still be increased and the crosstalk has not been considered yet, an extra step of optimization is introduced. A FOM threshold $\mathrm{FOM_{th}}$ is defined to select the best k sets of parameters,

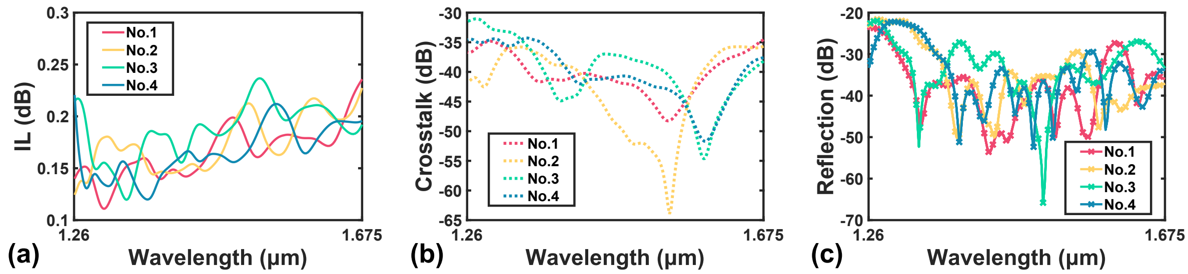

Figure 5.6: Calculated spectra of (a) IL, (b) crosstalk, and (c) reflection of all candidate geometries specified in Table 5.3.

where k depends on $\mathrm{FOM_{th}}$. Then the structure is finalized by choosing the geometries with the best secondary FOM among the k candidate sets. In this work, for instance, $\mathrm{FOM_{th}}$ is set to 0.25 dB. Since only 4 sets of parameters fulfill FOM <0.25 dB, they are selected as candidates and sent to the 3-D FDTD simulation engine again, but with finer meshes. The 4 sets of parameters are shown in Table 5.3, and their corresponding calculated spectra of IL, crosstalk, and reflection are demonstrated in Figure 5.6. One sees that all the candidates perform well in terms of the IL spectrum. Then the maximum crosstalk is chosen as the secondary FOM, and design no. 2 achieves the least maximum crosstalk. Hence, the geometry is determined that $N_\mathrm{r} = 9$, $W = 0.850$ µm, and $\Lambda = 0.185$ µm. Under the highest mesh accuracy, the structure obtains max(IL) = 0.229 dB, max(Crosstalk) = -35.6 dB, and max(Reflection) = -21.6 dB, outperforming the initial design in terms of broadband performance except for the reflection property. One should notice that the footprint of the improved design is only 9.78 * 9.78 µm^2, smaller than that of the initial design, 16.56 * 16.56 µm^2. Furthermore, besides the centering SWG that takes 3.38 * 3.38 µm^2 space, the rest of the area is rather empty since it only contains taper strip waveguides, which makes the component arrangement around the crossing very flexible when designing the circuit. Therefore, this is a very compact design.

Table 5.4 concludes the three-step optimization for the improved design. The three steps are compared in terms of optimization method, simulation technique, mesh accuracy,

Parameters	N_r	Λ (µm)	W (µm)
No. 1	9	0.180	0.850
No. 2	9	0.185	0.850
No. 3	9	0.185	0.900
No. 4	9	0.190	0.900

Table 5.3: Candidate sets of parameters selected from Figure 5.5

simulation time, FOM, and number of iterations. Such a layered process avoids a large number of time-consuming simulations with dense meshes at one time, while maintaining the reliability of the optimization.

Step	Method	Technique	Mesh accuracy	Simulation time
1	PSO	3-D FDTD	˜10 mesh points / λ	short
2	3-D sweeping	3-D FDTD	˜14 mesh points / λ	medium
3	1-D sweeping	3-D FDTD	˜18 mesh points / λ	long
Step	FOM	Number of iterations		
1	max(IL)	25*15		
2	max(IL)	3*5*7		
3	max(Crosstalk)	4		

Table 5.4: Summary of the three-step optimization process

Last but not least, the fabrication tolerance of the improved design is discussed. Due to the periodic nature of SWG, the fill factor ff tends to be more sensitive to fabrication errors than the period Λ. Hence, our analysis focuses on the fill factor. The maximum IL, crosstalk, and reflection as functions of ff are calculated and plotted in Figure 5.7. It is implied from Figure 5.7 that the performance is not very tolerant to a largely increased ff since the maximum IL reaches around 1 dB when the fill factor increases from 2/3 to 5/6. Nevertheless, the design performs stably as ff declines, and the maximum crosstalk and maximum reflection even decrease. With a ff ranging from 1/2 to 7/9, the maximum IL over the 415-nm optical band is kept below 0.38 dB, the maximum crosstalk (CT) is lower than -31 dB, and the maximum R is below -18 dB. It is then a reasonable choice to apply a

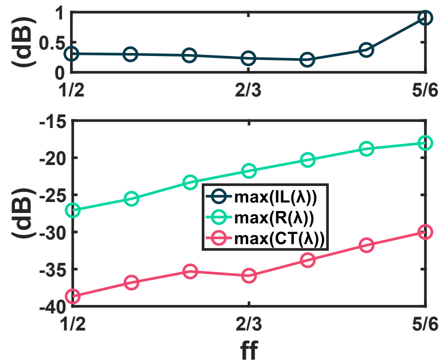

Figure 5.7: Dependence of maximum IL, maximum crosstalk, and maximum reflection on fill factor, as a fabrication tolerance analysis.

slightly lower fill factor when producing the crossing on the chip, to acquire more tolerance of fabrication errors, lower crosstalk, and less reflection at the cost of marginally higher IL overall.

To conclude the design process, we demonstrate the electric field distribution of the initial and the improved design, along with the two reference structures in Figure 5.2(c). The absolute values of the y-axis components of the electric field, $|\mathbf{E}_{\mathrm{y}}|$ at the $z = 0$ plane are captured from simulations and displayed in Figure 5.8. It is shown that the transmittance can be increased by the SWG cladding, especially the curved SWG, at both the lower and upper bounds of the wavelength range, namely 1260 nm and 1675 nm.

5.3 Experiment

Both the initial and improved designs were fabricated on the standard 220 nm SOI platform with a 2.2 µm-thick top cladding oxide, by the NanoSOI fabrication process of Applied Nanotools Inc. Broadband vertical grating couplers are applied to couple light into and out of the chip [115,116]. The testing setup is the same as Fig. 3.9. Since the calculated loss of the proposed device is too low to neglect the measurement errors, we measured the transmission

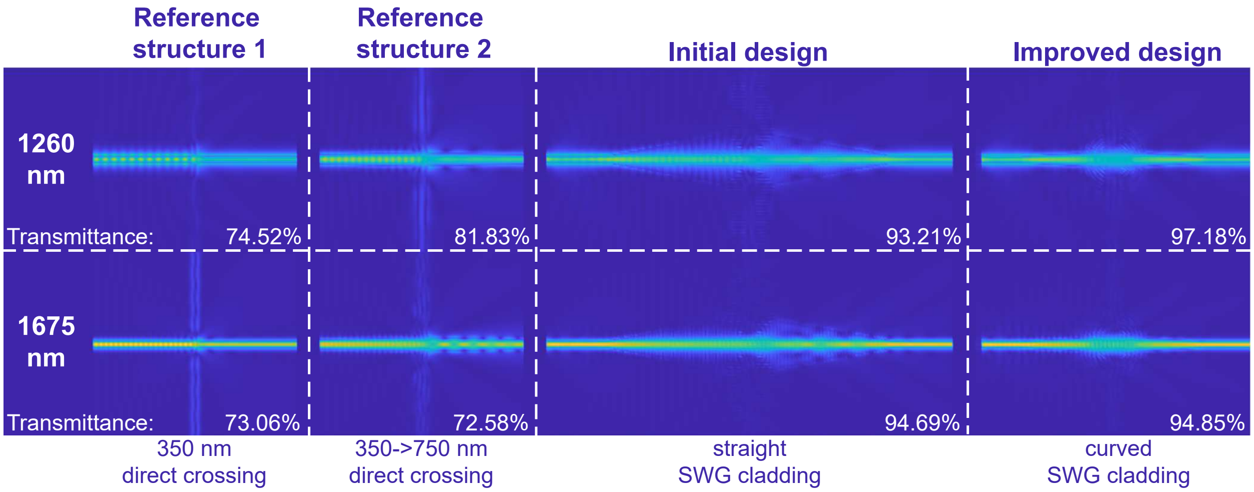

Figure 5.8: Electric field distribution, specifically $|\mathbf{E}_\mathrm{y}|$ of the two reference structures (Figure 5.2(c)), the initial design (Figure 5.1), and the improved design (Figure 5.3), at 1260 nm and 1675 nm.

spectrum of 14, 32, and 50 cascaded crossings to accurately estimate the insertion loss, as shown in Figure 5.9. The test structure is duplicated, but with O-band and C-band grating couplers respectively, so that the performance over [1260 nm, 1360 nm], and [1500 nm, 1630 nm] can both be measured. As for the crosstalk test, the cross port rather than the output port of the crossing is connected to the output grating coupler. Back-to-back connected pairs of grating couplers are placed near the devices for calibration.

The image of a single fabricated crossing with the improved design from the SEM is displayed as an inset of Figure 5.9. The clear features show that the curved SWG is decently fabricated.

The experimental results from 1500 nm to 1630 nm are shown in Figure 5.10. For the initial design, the measured transmission spectra with various numbers of cascaded devices are shown in Figure 5.10(a), from which the ILs are extracted by linear fitting in Figure 5.10(b). To make sure that all three measured values are considered at each wavelength, the point (0,0) is also added, so that the fitted IL is based on four data points. Figure

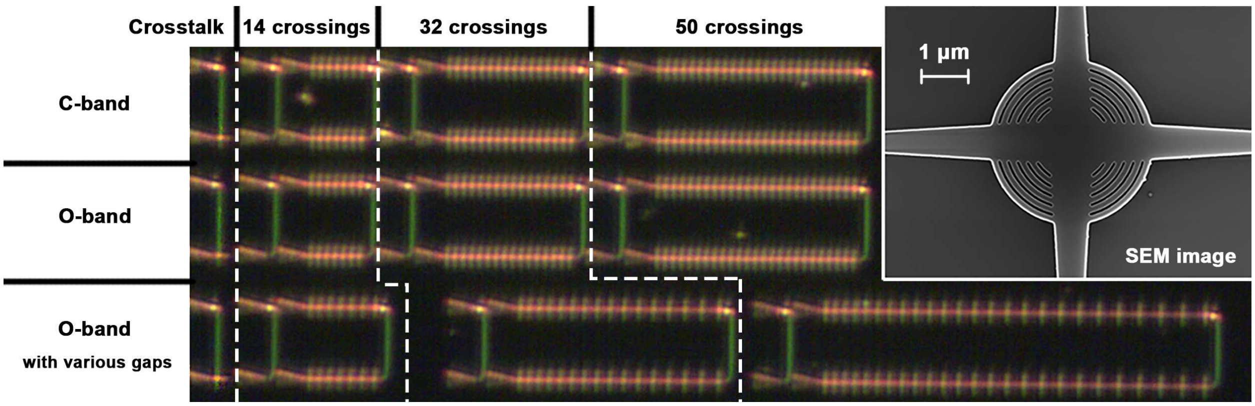

Figure 5.9: Measurement arrangement for the proposed crossing. Inset shows the SEM image of a single fabricated crossing with the improved design.

5.10(c) displays the measured crosstalks over the measured wavelength range. Whilst Figure 5.10(d), (e), and (f) corresponds to the results of the improved design in the same order as stated above. As can be seen from Figure 5.10(b) and (e), the IL response over [1500 nm, 1630 nm] ranges from 0.199 dB to 0.275 dB for the initial design, and from 0.181 dB to 0.264 dB for the improved design. Whilst the responses are both flat, the maximum measured IL of the improved design is 0.011 dB below that of the initial design. The improved design also outperforms the initial design on the crosstalk, as the maximum crosstalk of the improved design is only -35.2 dB, which is 10.0 dB below the maximum value for the initial design.

The results obtained in the O-band are more complicated to analyze than that near C-band. From Figure 5.11(a) and (d), notches in transmission spectra are observed at wavelengths shorter than 1310 nm. Since the notches emerge uniformly on the wavelength axis, it is possible that they come from the response of Fabry-Pérot cavities. Tracing back to Figure 5.6(c), relatively high reflection is observed at the same wavelength range. The calculated reflections are larger than -23.7 dB for wavelengths shorter than 1310 nm, while they drop rapidly below -25.1 dB in wavelengths >1325 nm. Thus, multiple Fabry-Pérot cavities are formed between the cascaded crossings at short wavelengths. Although a single Fabry-Pérot cavity is not harmful due to the weak reflection, with uniform gaps between the

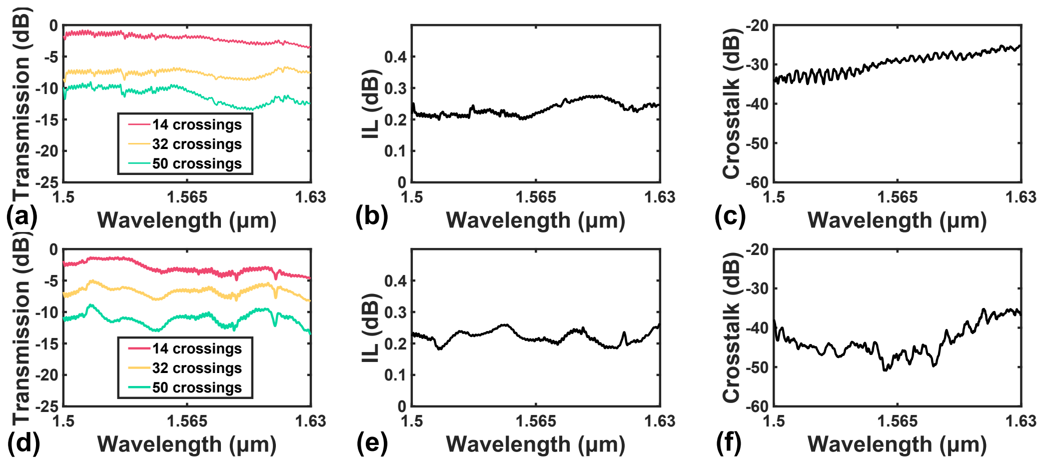

Figure 5.10: (a) Measured transmission spectra with 14, 32, and 50 cascaded crossings, (b) fitted IL spectrum, and (c) measured crosstalk spectrum of the initial design from 1500 nm to 1630 nm. (d) Measured transmission spectra with 14, 32, and 50 cascaded crossings, (e) fitted IL spectrum, and (f) measured crosstalk spectrum of the improved design from 1500 nm to 1630 nm.

fabricated devices, the responses of the multiple Fabry-Pérot cavities overlap and become spikier. This also explains why the notches in the spectrum with 50 crossings are deeper than that with 14 crossings.

Aware of the fact that the notches are not caused by the crossing itself, the ILs at the notches can be estimated by spline interpolation using the data points beside the notches, as demonstrated by the red dots in Figure 5.11(b) and (e). The maximum IL of the improved design is only 0.178 dB, much lower than that of the initial design, 0.352 dB. Comparing Figure 5.11(c) and (f), it is inferred that the improved design is also better than the initial design in terms of crosstalk in the O-band. The maximum measured crosstalk is -30.9 dB for the improved design and -26.2 dB for the initial design.

Although such estimation methodology is acceptable for the crossing to be used as a single component in a circuit, it does not make sense when multiple crossings are cascaded on the chip, just as the way the crossings are fabricated in our test chip. We propose two methods

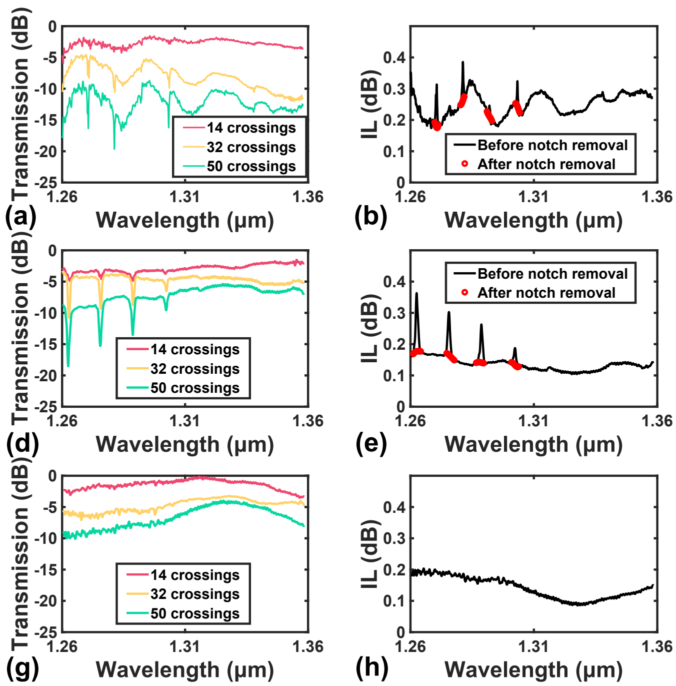

Figure 5.11: (a) Measured transmission spectra with 14, 32, and 50 cascaded crossings, (b) fitted IL spectrum, and (c) measured crosstalk spectrum of the initial design from 1260 nm to 1360 nm. (d) Measured transmission spectra with 14, 32, and 50 cascaded crossings with uniform gaps, (e) fitted IL spectrum, and (f) measured crosstalk spectrum of the improved design from 1260 nm to 1360 nm. (g) Measured transmission spectra with 14, 32, and 50 cascaded crossings with various gaps and (h) fitted IL spectrum of the improved design from 1260 nm to 1360 nm.

to mitigate this issue. The first method is to decrease the reflection. The condition for the gratings to operate in the SWG regime is given by $\lambda > 2n_{\text{eff}}\Lambda$. Therefore, if the period of the SWG is further decreased, the devices will operate further away from the Bragg reflection regime. However, the minimum feature size also shrinks under such modification, adding challenges to the fabrication process. The n_{eff} can be decreased as well by reducing the fill factor ff. The effect has been predicted by Figure 5.7, where the maximum reflection declines when ff is smaller. Nonetheless, it comes at a cost of larger IL overall.

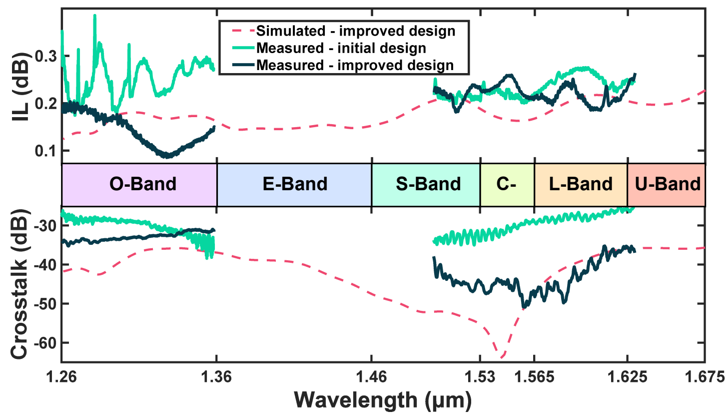

Figure 5.12: Multi-band device performance comparing the measured results of the improved design with the measured results of the initial design and the calculated results of the improved design, in terms of IL and crosstalk.

Hence, the second method is proposed. Instead of reducing the reflection, we change the way of arranging the cascaded crossings. As shown in Figure 5.9, we introduce various gaps between the cascaded crossing to prevent the responses from overlapping. The transmission spectra of such an arrangement are measured and displayed in Figure 5.11(g). The results prove that such a design manages to eliminate the notches in the spectra. As can be seen from Figure 5.11(h), the maximum IL is 0.204 dB, and the ILs at wavelengths <1310 nm are generally higher than that obtained from the uniformly placed crossings shown in Figure 5.11(e). Since the responses of the multiple Fabry-Pérot cavities are no longer overlapping, the increase in ILs can be regarded as those responses spread out on the spectrum. Because the results with various gaps are closer to the real situation and need less post-processing, they are considered as the final estimated IL spectrum of the improved design.

Finally, we conclude the overall performance of our proposed design in Figure 5.12. We compare the measured results of the improved and the initial design and the simulated results of the improved design. It can be implied that the measured IL and crosstalk spectra accord well with the simulation for the improved design, with slightly higher maximum IL and

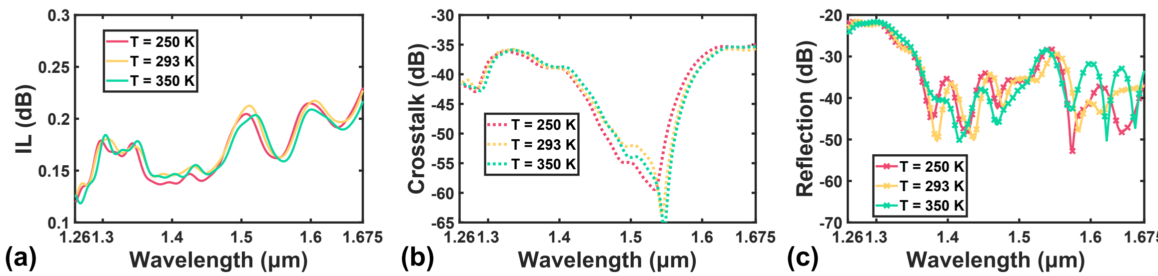

Figure 5.13: Calculated spectra of (a) IL, (b) crosstalk, and (c) reflection under various temperatures.

crosstalk. We also prove the superiority of the improved design compared to the initial design from an experimental perspective. Over the 230-nm wavelength range of measurement, the proposed device achieves a maximum IL of 0.264 dB and a maximum crosstalk of -30.9 dB, demonstrating decent functionality over essential optical communication bands including the O-, C-, and L-bands.

5.4 Analysis on temperature sensitivity

Aside from the broadband feature of our proposed designs that are demonstrated in the previous sections, the sensitivity of temperature should also be discussed. Typical low-loss crossing designs on SOI usually utilize the self-imaging effect of multi-mode interference to concentrate the light at the intersection. While this is an effective method, the beat length is sensitive to temperature changes, which leads to performance degradation in an environment with heat fluctuation. Very few works on waveguide crossing report temperature-related results.

On the contrary, our proposed design introduces the SWG as lateral claddings, and single-mode transmission is guaranteed through the crossing. Such simplicity may stabilize the device performance within a large range of temperatures. To evaluate it, the spectra of IL, crosstalk, and reflection are calculated using the index profile of silicon under 250 K, 293 K, and 350 K. The refractive index information is collected from [37]. For the oxide layers, since the thermal-optics coefficient of SiO_2 is much lower than that of silicon, the index is kept the same. Note that the indices under 293 K are the profile applied in all previous simulations.

The calculated results shown in Figure 5.13 regarding the improved design exhibit no significant difference among the spectra under different temperatures. In Figure 5.13(a), the IL ranges from 0.124 dB to 0.229 dB over all optical communication bands under 293 K. Whilst the IL ranges are [0.120 dB, 0.232 dB] and [0.118 dB, 0.219 dB] for 250 K and 350 K, respectively. A closer inspection of the curves shows that the shape of the IL spectrum is maintained from 250 K to 350 K, only with a slight red shift as the temperature increases. A similar statement can be made on crosstalk and reflection. The maximum crosstalks are -34.9 dB, -35.6 dB, and 35.3 dB under 250 K, 293 K, and 350 K, respectively. As for reflection, the maximum values are -21.6 dB, -21.6 dB, and -21.7 dB for the three temperatures. The pattern of the spectrum is kept during temperature changes in both Figure 5.13(b) and (c).

Although the temperature insensitivity has been proved by simulations, it needs further verification from experiments. Since a thermoelectric cooler (TEC) is inserted under the testbed, a TEC controller can be used to tune the temperature of the chip. The transmission spectra are then repeatedly measured under different temperatures, including 10 °C, 25 °C, 40 °C, and 55 °C. The results are shown in Figure 5.14. From 10 °C to 55 °C, the ILs are kept below 0.204 dB from 1260 nm to 1360 nm, and they are below 0.289 dB from 1500 nm to 1630 nm. As for the crosstalk, the values are all below -30.7 dB from 1260 nm to 1360 nm, and they are below -34.7 dB from 1500 nm to 1630 nm. These values are very close to the results reported in the previous section. It is then inferred that the temperature hardly affects the device performance, which is an advantage for the crossing to be used in real-world circuits.

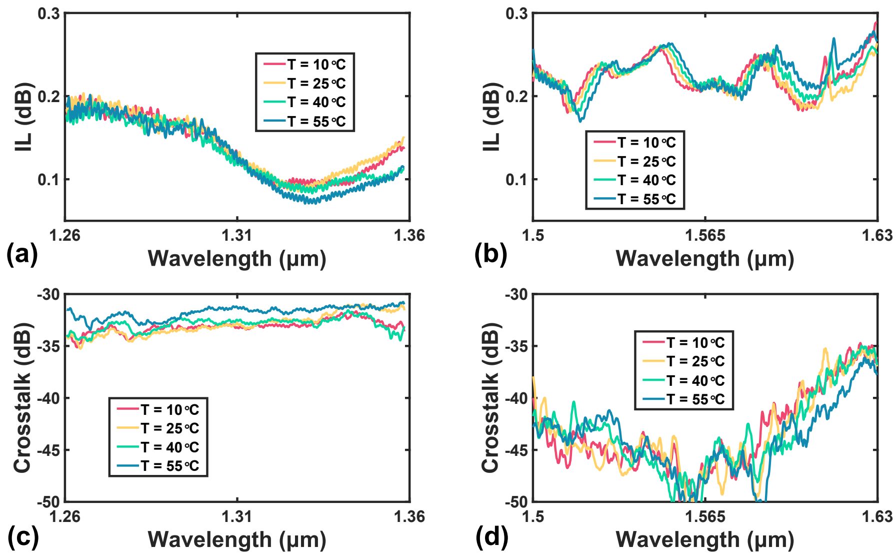

Figure 5.14: Measured IL spectra (a) from 1260 nm to 1360 nm, and (b) from 1500 nm to 1630 nm, measured crosstalk spectra (c) from 1260 nm to 1360 nm, and (d) from 1500 nm to 1630 nm of the improved design with various gaps under different temperatures.

5.5 Conclusion

In conclusion, we have designed two versions of multi-band SOI waveguide crossing that apply SWG as lateral cladding. The initial design uses straight SWG cladding to reduce the index contrast, then decrease the proportion of the light that is radiated out. However, the initial design cannot achieve a compact footprint due to the need of a long taper. Therefore, curved SWG is proposed to replace the straight waveguide, which forms the improved design. The curved SWG can be modeled as a metamaterial with gradually changing permittivity tensors, thus making the device exempt from the need for a long taper and improving the performance of the device as well. After a three-step optimization, the improved design achieves a calculated maximum IL of 0.229 dB and maximum crosstalk of -35.6 dB from 1260 nm to 1675 nm, covering all the optical communication bands. The proposed device is then fabricated and characterized over a 230-nm wavelength range consisting of [1260 nm, 1360 nm] and [1500 nm, 1630 nm]. To accurately estimate the IL, cascaded crossings with different numbers are fabricated on the chip, and the ILs are obtained by linear fitting. Since the relatively high reflection in the O-band causes notches in the IL spectrum, various gaps between the cascaded devices are introduced to cope with the issue. As a result, the improved design achieves measured maximum IL of 0.204 dB and maximum crosstalk of -30.9 dB from 1260 nm to 1360 nm, and maximum IL of 0.264 dB and maximum crosstalk of -35.2 dB from 1500 nm to 1630 nm. The temperature sensitivity of the proposed crossing has also been evaluated in simulation and experiments. Both calculated and measured results of the improved design under different temperatures demonstrate excellent performance stability. Such a broadband, compact, and temperature-insensitive design enriches the component library of multi-band PIC. Furthermore, the proposed curved SWG may provide a new perspective for designers to apply SWG in silicon photonics devices.

Chapter 6

Transmitter DSP for optical DSCM transmission on a silicon photonic modulator

6.1 Motivation

The DSCM system has become an attractive technology in optical communication over the years. Compared to conventional single-carrier transmission, the DSCM scheme utilizes multiple channels without the need for extra hardware such as lasers and digital-to-analog converters (DAC) because they are multiplexed digitally with transmitter digital signal processing (DSP). Such multi-channel transmission has proved superior to single-carrier systems in various aspects. The DSCM scheme is effectively used in long-haul optical fiber transmission systems to mitigate fiber nonlinearities [153]. By digitally multiplexing the Nyquist subcarriers, the symbol rate can be optimized to minimize the effect of the fiber nonlinearity including self-phase modulation (SPM), cross-phase modulation (XPM), and four-wave mixing (FWM) components, according to the enhanced Gaussian noise (EGN) model [154]. Spectrum optimization via DSCM also increases the tolerance to filter concatenation [155, 156]. Furthermore, it was shown that the DSCM system is more tolerant to equalization enhanced phase noise (EEPN) [157], and the complexity of the CD compensation can be significantly reduced in DSCM systems [158]. In [159], researchers applied probabilistic constellation shaping (PCS) in a DSCM system. Here, different entropies are loaded onto different subcarriers in a band-limited DSCM transmission system. The results show gains compared to single-carrier transmission. Recently, researchers have proposed to utilize the DSCM configuration to reduce the cost of optical access networks, meanwhile realizing flexible, adaptable, and scalable software-configurable networks [160]. Although multi-channel transmission can also be realized by orthogonal frequency-division multiplexing (OFDM), it does not allow independent transmission and processing of the subcarriers as DSCM does. Such features limit the application of OFDM systems, especially in agile optical networks. In [161], the autonomous operation of subcarriers can only be implemented using the DSCM approach but not the OFDM approach, since it depends on the fact that the subcarriers can be configured independently in DSCM.

However, the DSCM system suffers from several defects, especially on the transmitter side. It is commonly accepted that multi-carrier transmission schemes such as OFDM and DSCM systems are afflicted by high PAPR [153, 162, 163]. With limits on the transmitted peak value, a high PAPR results in a low optical power being launched into the fiber, which constrains the transmission reach. While PAPR reduction techniques for OFDM systems have been extensively studied [162], this topic is not well investigated for DSCM optical fiber transmission systems. Moreover, the nonlinear transfer functions of the modulators and the radio-frequency (RF) amplifiers as the drivers distort the transmitted signals. While the pre-compensation based on a look-up table (LUT) can be used to mitigate this issue for single-carrier systems, it is not feasible for DSCM signals, since the device nonlinearity will be translated to noise rather than constellation deformation in each subcarrier.

Back to the theme of this thesis, optical transmitters based on silicon photonics technology are considered a low-cost solution due to their compatibility with the CMOS process. As the core component, high-speed silicon photonics modulators have been intensively studied for the past decade [48, 49, 164–166], among which the Mach-Zehnder modulator (MZM) is a promising candidate for its relatively large bandwidth. However, the MZMs usually require high driving voltages which approach the nonlinear region in the transfer function of the modulator drivers. The high PAPR of the DSCM signals will also require more gain from the RF amplifiers, leading to more power consumption. Therefore it is necessary to develop algorithms to mitigate those issues, especially when silicon photonics optical transmitters are employed.

6.2 The impact of transmitter parameters on DSCM system

In an ideal transmission system with the additive white Gaussian noise (AWGN) added to the signal, the DSCM system will theoretically achieve the same performance as the single carrier system under the same SNR. However, the real system is not usually a mean-power-limited system. For example, since the DAC has a fixed maximum output level, the high PAPR of the DSCM signals leads to lower launch power.

Therefore, a simulation platform is built to study the effect of relevant transmitter parameters on the performance of both DSCM and single-carrier systems. The initial simulation includes a parameterized optical transmitter with an IQ-MZM under the single-driver series-push-pull (SPP) configuration and a conventional coherent receiver. Note that in this chapter, the received optical power (ROP) is fixed during the parameter sweep. The reason is to keep the same noise level generated by the BPDs so that the performance is only affected by the analyzed parameters.

The global configuration of the simulation is listed in Table 6.1.

Number of subcarriers	8
Total symbol rate	80 GBaud
Modulation format	32QAM
RRC Roll-off factor	0.1
3-dB bandwidth of DAC channels	50 GHz
Pre-emphasis	Yes
Clipping ratio	12 dB
Laser power (Tx & Rx)	15 dBm
Laser linewidth (Tx & Rx)	1 Hz (nearly no phase noise)
Laser frequency offset	0 Hz
Channel	Optical back-to-back (B2B)
PD responsivity	0.45 A/W
Number of total transmitted bits	327680

Table 6.1: Simulation configuration

The data structure and DSP blocks applied in the DSCM system simulation are displayed in Fig. 6.1. The transmission bits are first converted to N parallel sequences, where N is the number of subcarriers. Each sequence is independently mapped to QAM symbols, shaped by RRC pulse shaping filters at 2 samples per symbol, and up-sampled by a factor of N. Then the subcarriers are shifted to their allocated frequency slots and combined. Note that the frequency shifts are determined to ensure that there are no overlaps or gaps between the shaped subcarriers. The composite signal is then processed by the pre-emphasis filters, the clipping, and the quantization before being sent to the DACs. At the receiver side, the signal captured by the analog-to-digital converters (ADC) is first corrected and synchronized with the transmitted samples. Then it is resampled to $2N$ samples per symbol. After chromatic dispersion compensation (CDC), the signal is split into N lanes and shifted in order to center each subcarrier in the frequency domain. The following matched RRC filters operate at $2N$ samples per symbol and act as low-pass filters (LPF) at the same time to eliminate other unwanted subcarriers in each lane. Each subcarrier is then down-sampled by a factor of N.

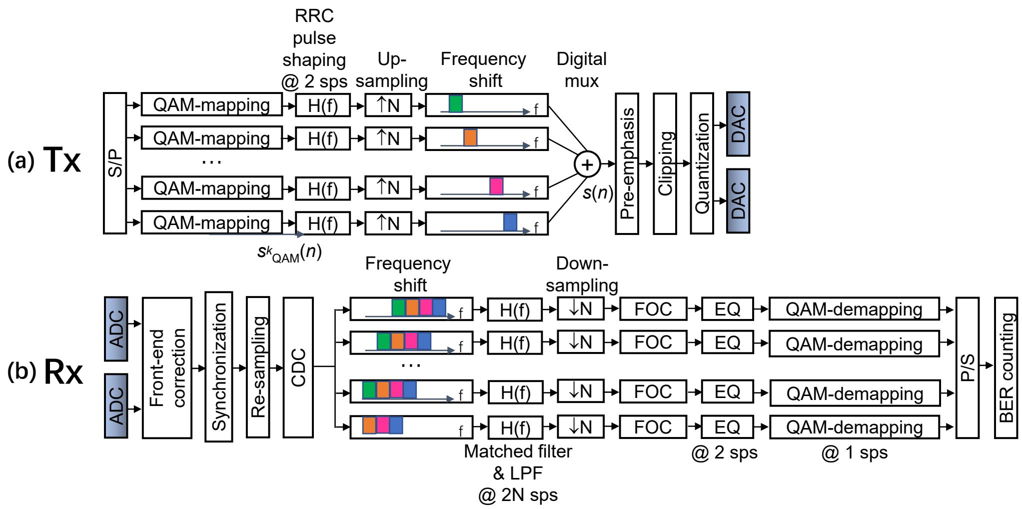

Figure 6.1: (a) Transmitter and (b) receiver data structure and DSP for the DSCM system. EQ: (adaptive LMS) equalizer.

Finally, the symbols are recovered by frequency offset compensation (FOC) and adaptive equalization based on the least mean square (LMS) algorithm. Note that the adaptive equalizer is training-symbol-directed so that the performance is maximized. The bit error rate (BER) is calculated using the received bits from the QAM-symbol demapping.

First, we study the ER of the MZM. The value of ER is swept and the BERs under different numbers of subcarriers are recorded. Note that the number 1 corresponds to the single-carrier system. The results are shown in Fig. 6.2. For Fig. 6.2(a), the ROP is fixed at -20 dBm, so that the BERs are around the hard-decision forward error correction (HD-FEC) threshold of 3.8e-3. For Fig. 6.2(b), the ROP is fixed at -22.5 dBm, so that the BERs are around the SD-FEC threshold of 2e-2. A clipping ratio as high as 12 dB is set to avoid the unwanted influence of clipping. Note that the half-wave voltage V_π of the modulator is set to $V_\pi = 3V_{\mathrm{RF}}$. To clarify, the V_{RF} here is defined as the swing of the RF signal before the SPP-MZM, so the swing applied on the SPP-MZM is $V_{\mathrm{RF}} - (-V_{\mathrm{RF}}) = 2V_{\mathrm{RF}}$. This way the modulation depth is $2V_{\mathrm{RF}}/2V_\pi$ in this paper rather than $V_{\mathrm{RF}}/2V_\pi$. Such configuration

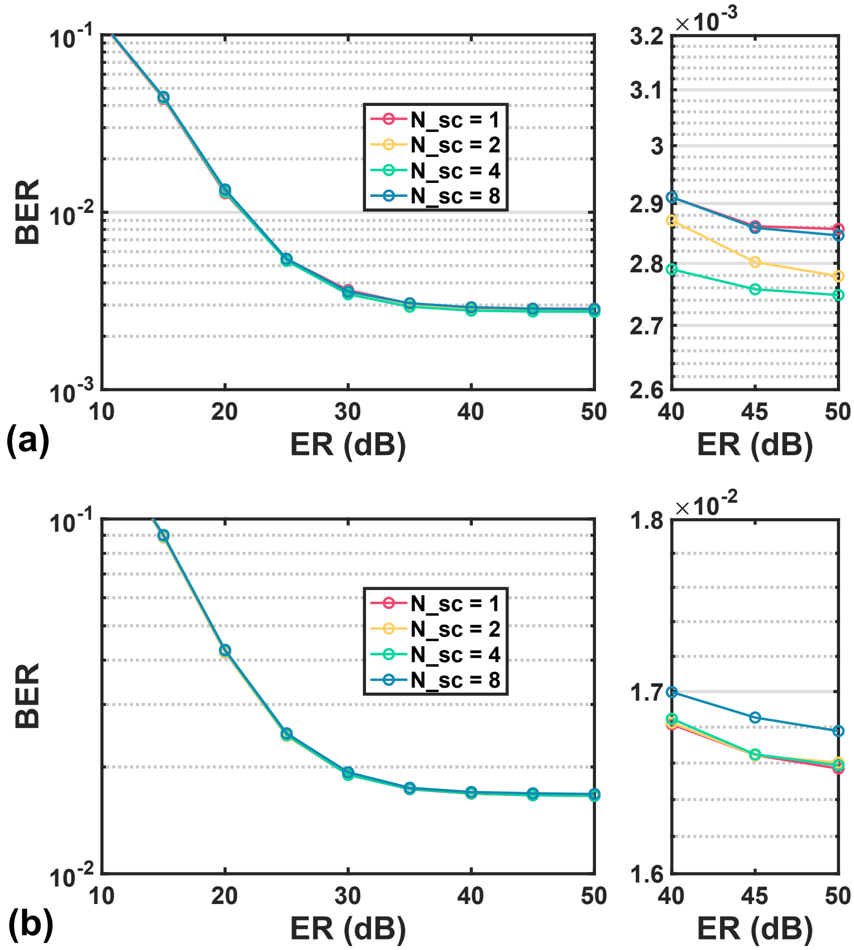

Figure 6.2: Dependence of calculated BER on the extinction ratio at (a) ROP = -20 dBm and (b) ROP = -22.5 dBm, with different numbers of subcarriers.

guarantees that the RF signal is limited in the linear region of the transfer function of an SPP-MZM.

From Fig. 6.2, it is inferred that the performance converges after ER $>$ 40 dB when we use one-third of the transfer function. Since the ER determines the minimum modulated intensity, the results will likely vary when the ratio V_{RF}/V_{π} changes. Another observation is that the performance is irrelevant to the number of subcarriers.

Usually with an SPP-IQ-MZM in a coherent transmitter, V_{RF} needs to be controlled

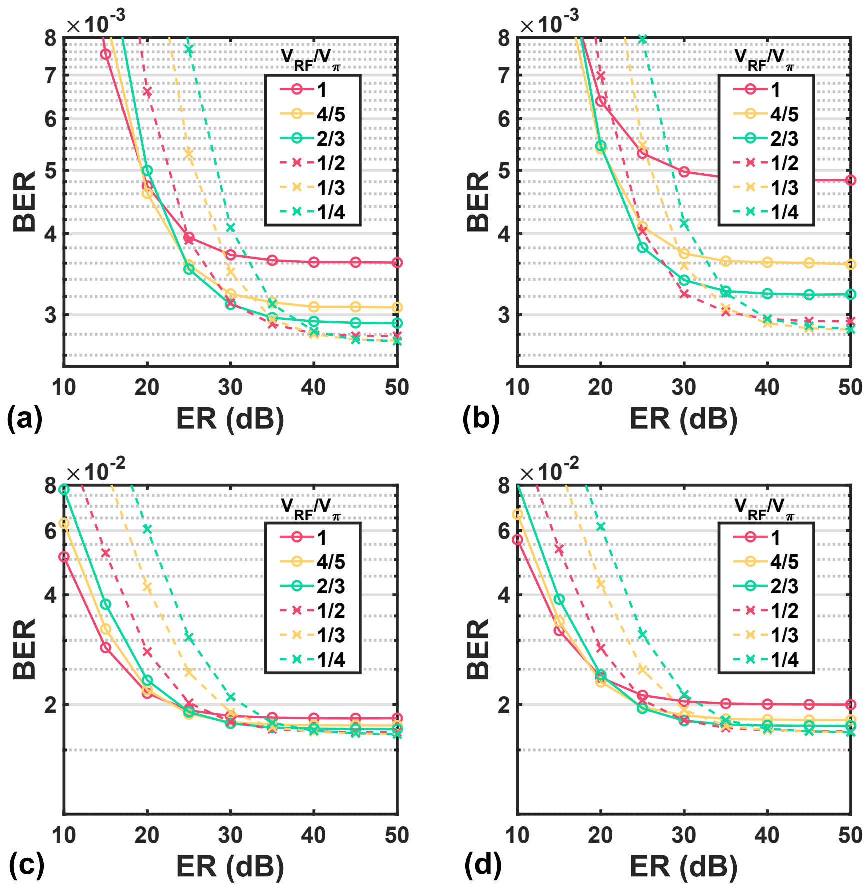

Figure 6.3: Dependence of calculated BER on the extinction ratio under different V_{RF}/V_π for (a) the single-carrier system and (b) the DSCM system with 8 subcarriers at ROP = -20 dBm. Dependence of calculated BER on the extinction ratio under different V_{RF}/V_π for (c) the single-carrier system and (d) the DSCM system with 8 subcarriers at ROP = -22.5 dBm.

so that $V_{\mathrm{RF}}/V_\pi < 2/3$, to avoid excessive device nonlinearity from the sinusoidal transfer function. To evaluate the effect of the nonlinear transfer function on DSCM and single-carrier systems, the interplay between the ratio V_{RF}/V_π and the ER is studied. Specifically, the BER trends with changing ER under different V_{RF}/V_π are recorded and shown in Fig. 6.3, since such results make one understand how the system behaves under both ideal modulators with high ERs (more than 40 dB) and practical devices with relatively low ERs (less than

20 dB), which is the reason behind such methodology.

From Fig. 6.3, one can see that the convergence of BER under increasing ER is dependent on the ratio V_{RF}/V_{π}. When $V_{\mathrm{RF}}/V_{\pi} = 1$, which means that the RF signal covers the full range of modulator transfer function, the system is more tolerant to low ERs, since the signal power is large compared with the lowest level. However, the BER fails to converge to an acceptable value when the ER is large enough. That is the effect of the nonlinear transfer function. Comparing Fig. 6.3(a) and (b), the nonlinearity causes more damage on a system with 8 subcarriers than the single-carrier system, even when there is no nonlinearity compensation in both systems.

When $V_{\mathrm{RF}}/V_{\pi} = 1/4$, which means that the signal only covers one-fourth of the modulator transfer function, the BER converges at higher ERs. Although the performance after convergence is better compared to the case where $V_{\mathrm{RF}}/V_{\pi} = 1$, that is due to the fixed ROP. In a real system, a low V_{RF}/V_{π} leads to more dynamic loss of the optical signal, which further limits the capacity of the system. When the value of the ER is more practical, 20 dB for example, a low V_{RF}/V_{π} further aggravates the performance according to 6.3. Clearly, a large V_{RF}/V_{π} is preferred even with the presence of nonlinear effects.

Clipping is usually applied to the signal before being sent to the DAC to reduce the PAPR. The amplitudes with absolute values higher than the threshold value will be clipped to the threshold with the same sign. The clipping ratio is defined as the ratio of threshold power (squared threshold amplitude) over the mean power of the signal. Note that the PAPR of the sequence after clipping is very close to the clipping ratio, only slightly higher since the new average power decreases due to the clipping process. The lower the clipping ratio, the stronger the clipping. A signal with a higher PAPR usually suffers from more damage by the same amount of clipping. Therefore we proceed to study the effect of clipping on the DSCM and single-carrier systems, the results of which are shown in Fig. 6.4.

From Fig. 6.4, one can see that the effects of clipping on DSCM and single carrier systems are different. Since the DSCM signal usually has a larger PAPR, it is not suitable to use

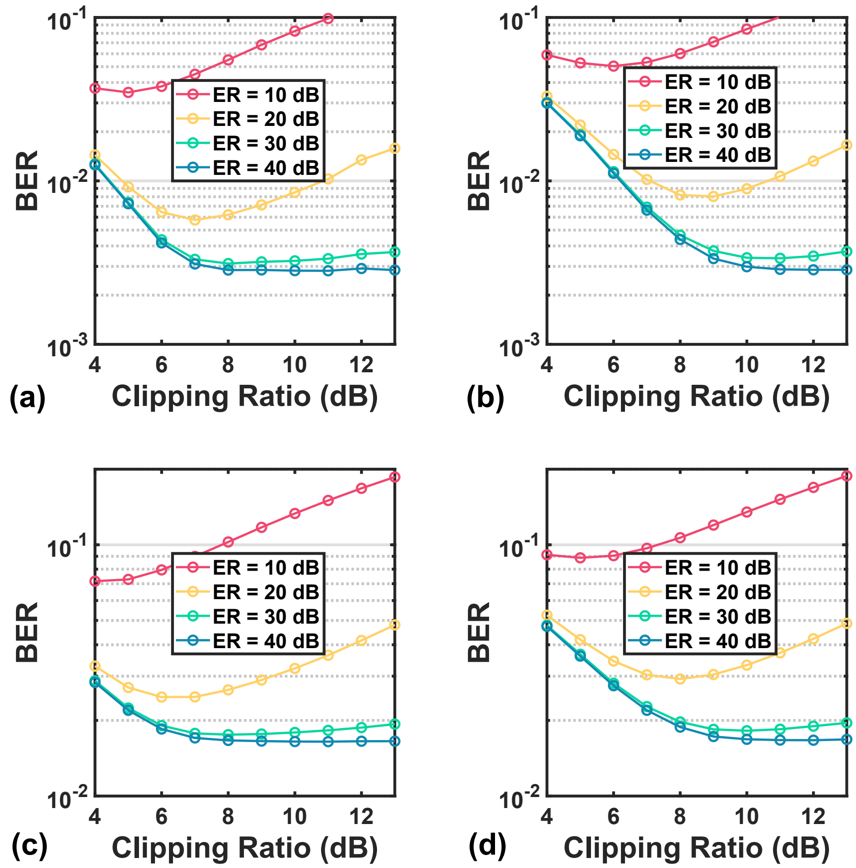

Figure 6.4: Dependence of calculated BER on the clipping ratio under different ER for (a) the single-carrier system and (b) the DSCM system with 8 subcarriers at ROP = -20 dBm. Dependence of calculated BER on the clipping ratio under different ER for (c) the single-carrier system and (d) the DSCM system with 8 subcarriers at ROP = -22.5 dBm.

strong clipping even though it provides higher launch power.

With a rather ideal modulator where ER = 40 dB, the distortion from finite ER can be neglected. Then the BER of the DSCM system with 8 subcarriers starts to be affected when PAPR approaches 10 dB, while this value is 8 dB for the single-carrier system. In a more practical case where ER = 20 dB, a high clipping ratio also results in high BER since the signal power is so small that the finite ER starts to deteriorate the signal. Under such distortion, the optimum PAPR for the DSCM system is ˜2 dB higher than that of the single-carrier system, at both ROPs. And the corresponding best BER is higher as well, even at the same ROP. Note that a higher clipping ratio leads to higher dynamic loss after the modulator, so the performance gap in a real system should be even larger.

From the previous simulation results, one can draw the following conclusions.

1) The design requirement of ER depends on V_{RF}/V_{π} when the modulation format is fixed. And a high V_{RF}/V_{π} can relax the requirement on high ER and increase the launch power. However, the nonlinearity from a low V_{π} damages the signal, and the DSCM system is more sensitive to device nonlinearity than the single-carrier system. Although LUT-based algorithms [167, 168] have been developed to compensate for the transmitter nonlinearity of single-carrier systems in a simple way, they are intrinsically not compatible with the DSCM system, since the device nonlinearity will be translated to noise rather than observable constellation distortion. Therefore, a pre-compensation scheme is needed specifically for the DSCM system.

2) The large PAPR of the DSCM system results in a large performance gap compared with the single-carrier system, which motivates us to develop a PAPR reduction method.

Now consider a scenario where we intend to apply the DSCM system on a silicon photonics IQ-MZM in order. Since the V_{π} of high-bandwidth silicon photonics MZMs is usually large [49], high-gain RF amplifiers are needed as modulator drivers, which bring another source of transmitter nonlinearity to the system. Meanwhile, the high PAPR of the DSCM signals increases the required gain of the RF amps so the transmitter becomes less power efficient. Therefore, it becomes more meaningful to develop effective signal processing algorithms following points 1) and 2) if we want to employ DSCM systems on a silicon-based transmitter.

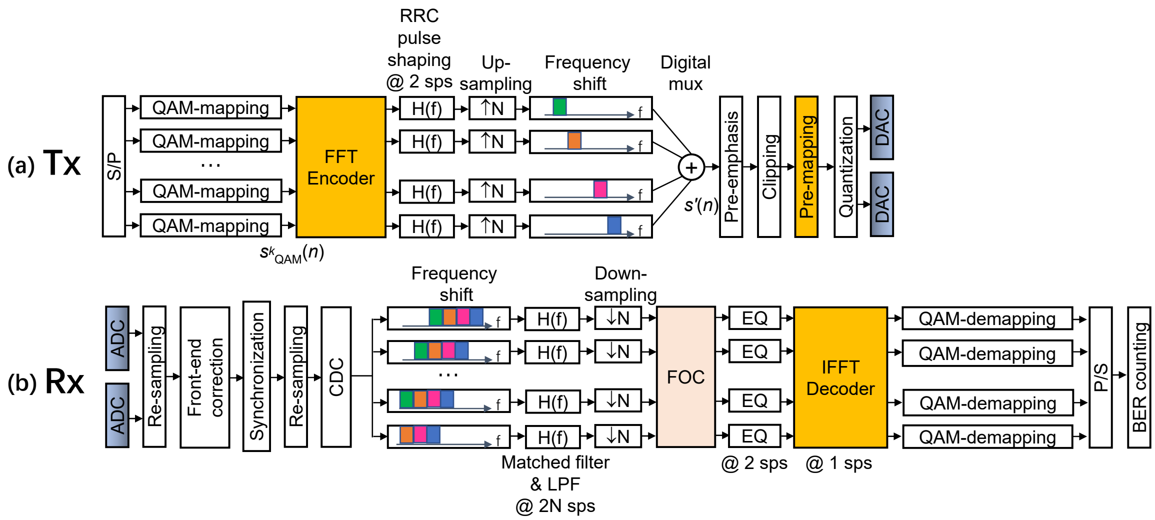

Figure 6.5: Modified (a) transmitter and (b) receiver data structure and DSP for the DSCM system with the addition of proposed algorithms that are highlighted in the figure. The FOC block is slightly emphasized since it needs modification when the FFT encoding is employed.

6.3 Proposed transmitter DSP for DSCM systems

6.3.1 FFT-based subcarriers encoding

Similarly to DSCM, the performance of the OFDM system is also limited by the high PAPR. Since the high PAPR of the system is caused by the inverse discrete Fourier transform (IDFT) operation that mixes multiple symbols in a single symbol block, it has been proposed to add a DFT stage before the IDFT so that the PAPR can be reduced. Such system is named DFT-spread OFDM, which has been demonstrated in OFDM-based optical communication systems [169–175]. However, such technique has not been applied to DSCM system to the best of our knowledge. Hence, we propose to encode the symbols from each subcarrier by an FFT stage, as demonstrated in Fig. 6.5. In this section, we elaborate on the theory and simulation results of the proposed FFT encoding scheme.

Consider a DSCM transmission with N subcarriers where N is usually a power of 2. Suppose $s_k(n)$ is the $2N$-samples-per-symbol sequence allocated for the (k+1)-th subcarrier, so that:

$$s_k(n) = \begin{cases} s_k^{\mathrm{QAM}}(n/2N), & n = 2Nk', k' = .., 0, 1, 2, .. \\ 0, & \text{otherwise} \end{cases}$$
$$k \in \{0, 1, .., N-1\}, \tag{6.1}$$

where $s_k^{\mathrm{QAM}}(n)$ is the complex QAM symbols transmitted by the (k+1)-th subcarrier. Note that $s_k(n)$ is only a constructed intermediate sequence that does not strictly follow the signal generation process in Fig. 6.1. However, it can be used to generate the equivalent composite signal $s(n)$ after subcarrier multiplexing in Fig. 6.1, which can be expressed as:

$$s(n) = \sum_{k=0}^{N-1} \sum_{m=-K}^{K} s_k(n-m)h(m)e^{j\omega_k n}, \tag{6.2}$$

where h is the $2N$-samples-per-symbol impulse response of the finite-impulse-response (FIR) RRC pulse shaping filter with a length of $2K$+1. ω_k is the shifted frequency for the (k+1)-th subcarrier that is given by:

$$\omega_k = \frac{\pi(k + \frac{1-N}{2})(1+\alpha)}{N}, \tag{6.3}$$

where α is the roll-off factor of the RRC filter.

We propose to add a simple FFT encoding stage as shown in Fig. 6.5. Then the multiplexed signal $s'(n)$ is expressed by:

$$s'(n) = \sum_{k=0}^{N-1} \sum_{m=-K}^{K} \hat{s}_k(n-m)h(m)e^{j\omega_k n}, \tag{6.4}$$

where the encoded symbols $\hat{s}_k(n)$ are given by:

$$\hat{s}_k(n) = \sum_{l=0}^{N-1} s_l(n) e^{-j\frac{2\pi kl}{N}}, \tag{6.5}$$

Now we consider a basic 2-subcarrier ($N = 2$) system with binary phase-shift keying (BPSK) modulation. To simplify the calculation, we only consider the samples at $n = 2Nk', k' = .., 0, 1, 2, ..$, which is exactly the sequence $s_k^{\text{QAM}}(n)$. The symbols $s_k^{\text{QAM}}(n)$ only contain ± 1 with equal probabilities. A 3-tap pulse shaping filter is assumed, including the current symbol and two adjacent symbols. The pulse shaping filter is defined as:

$$h(n) = \begin{cases} 1, & n = 0 \\ -a, & n = \pm 2N \\ 0, & \text{otherwise} \end{cases} \tag{6.6}$$

where $-a$ is the coefficient of the RRC filter at adjacent symbols. $-a$ depends on the roll-off factor, and is usually not positive. Here we assume $a \geq 0$ but do not assign a specific value to a.

For the uncoded symbols, the average power can be obtained following Equation 6.2:

$$\begin{aligned} P_{\text{avr}} = \mathbb{E}(|s_0^{\text{QAM}}&(n) e^{j\omega_0 n} \\ &- a s_0^{\text{QAM}}(n-1) e^{j\omega_0 n} \\ &- a s_0^{\text{QAM}}(n+1) e^{j\omega_0 n} \\ &+ s_1^{\text{QAM}}(n) e^{j\omega_1 n} \\ &- a s_1^{\text{QAM}}(n-1) e^{j\omega_1 n} \\ &- a s_1^{\text{QAM}}(n+1) e^{j\omega_1 n}|^2), \end{aligned} \tag{6.7}$$

Since $\omega_0 = -\omega_1$, by the independence between $s_0^{\text{QAM}}(n)$ and $s_1^{\text{QAM}}(n)$, also by the independence between adjacent symbols in the same sequence $s_k^{\text{QAM}}(n)$, we can obtain that $P_{\text{avr}} = 2 + 4a^2$. The peak value is reached when $n(\omega_0 - \omega_1) = 2k'\pi$, where k' is an integer, and the signs of the symbols are different from their adjacent symbols. Therefore we have $P_{\text{peak}} = (2+4a)^2$.

For FFT-encoded signals, we first look at the FFT expression when $N = 2$. Equation 6.5 becomes:

$$\begin{cases} \hat{s}_0^{\text{QAM}}(n) = s_0^{\text{QAM}}(n) + s_1^{\text{QAM}}(n), \\ \hat{s}_1^{\text{QAM}}(n) = s_0^{\text{QAM}}(n) - s_1^{\text{QAM}}(n), \end{cases} \tag{6.8}$$

This way the encoded symbols are no longer independent of each other. They have a joint probability mass function (PMF) as shown in Table 6.2.

		$\hat{s}_1^{\text{QAM}}(n)$		
		-2	**0**	**2**
$\hat{s}_0^{\text{QAM}}(n)$	**-2**	0	1/4	0
	0	1/4	0	1/4
	2	0	1/4	0

Table 6.2: Joint PMF of $\hat{s}_0^{\text{QAM}}(n)$ and $\hat{s}_1^{\text{QAM}}(n)$

Replacing $s_k^{\text{QAM}}(n)$ with $\hat{s}_k^{\text{QAM}}(n)$ in Equation 6.7, we obtain the average power of the encoded symbols $\hat{P}_{\text{avr}} = 4 + 8a^2$. Note that although $\hat{s}_0^{\text{QAM}}(n)$ and $\hat{s}_1^{\text{QAM}}(n)$ are not independent random variables, their covariance is still 0 according to Table 6.2. The peak power, however, needs careful calculation. By Table 6.2, only one of $\hat{s}_0^{\text{QAM}}(n)$ and $\hat{s}_1^{\text{QAM}}(n)$ can be non-zero. Therefore, even if the phases match, the peak power is only as high as $\hat{P}_{\text{peak}} = (2+4a)^2$.

The peak and average power of both FFT-encoded and uncoded systems are summarized in Table 6.3.

Table 6.3 shows that the FFT encoding reduces the PAPR by half. The entanglement among subcarriers caused by the FFT operation decreases the ratio of peak power over average power. However, the actual PAPR reduction will be different than the theoretical value due to the following reasons: 1) the samples between the symbols need to be considered,

$\text{PAPR} = \frac{\text{peak power}}{\text{average power}}$	Uncoded	FFT-encoded
Peak power	$(2+4a)^2$	$(2+4a)^2$
Average power	$2+4a^2$	$4+8a^2$

Table 6.3: Peak and average power of FFT-encoded and uncoded signals, 2 subcarriers, BPSK modulation, 3-tap pulse shaping filter

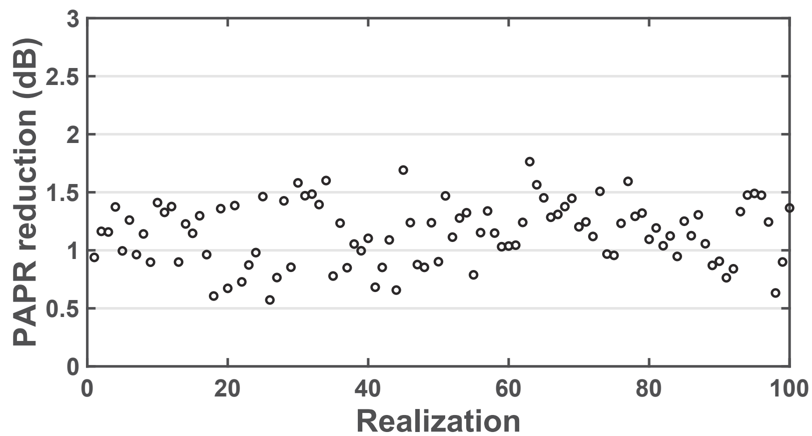

Figure 6.6: PAPR reduction by FFT encoding for different realizations of bit sequences.

2) the PAPR reduction can be dependent on the modulation format, and 3) the PAPR reduction can be dependent on the number of subcarriers. Therefore, we measure the value of PAPR reduction in our simulation system by the Monte Carlo method.

To evaluate the PAPR-reducing effect of the FFT encoding scheme on more complicated DSCM signals, 100 sets of pseudorandom binary sequences (PRBS) are generated with randomly selected seeds. Then the values of PAPR with and without the FFT encoding are calculated for each DAC channel, and the PAPR reduction is obtained by averaging the PAPR difference among all the channels. The results are shown in Fig. 6.6. The average PAPR reduction is 1.149 dB among the 100 realizations. Note that the reduction in PAPR is 1.150 dB for the baseline bit sequence that is used for previous simulations, which is very close to the average value.

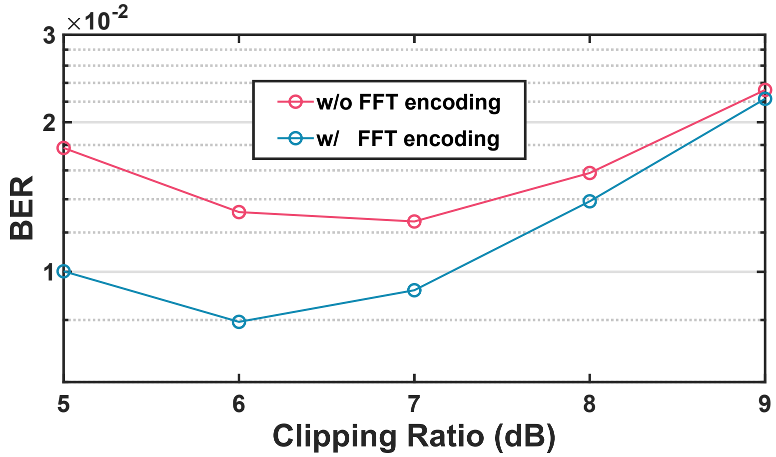

Figure 6.7: Dependence of calculated BER on clipping ratios with both FFT-encoded DSCM systems and original uncoded DSCM systems.

The next step is optimizing the clipping ratios of both encoded and uncoded systems. The BER trends under different clipping ratios are plotted in Fig. 6.7. Note that from this step on, the ROP of the receiver in the simulation is no longer fixed. Instead, the link loss of the channel is fixed. As a result, the optimal clipping ratio for the FFT-encoded system is about 1 dB lower than that of the original DSCM system. More importantly, the best BER of the encoded system is about 8e-3, better than that of the uncoded system, 1.2e-2. Such improvement is because the signal after FFT encoding can endure stronger clipping, thus increasing the launch power while not distorting the signal. Under the same link loss, the encoded transmission can then achieve higher SNR at the receiver due to higher ROP.

To evaluate the gain brought by the FFT encoding, we calculate the BERs of both systems as functions of link losses. Clipping ratios of 5, 6, and 7 dB are tested with the FFT-encoded system, while the values for the uncoded system are 6, 7, and 8 dB. The choices of clipping ratios are according to Fig. 6.7, from which the optimal and the two neighboring values of clipping ratios are selected.

Figure 6.8 indicates that the gains in terms of link loss provided by the FFT encoding are 0.912 dB and 0.989 dB with optimal clipping ratios at SD-FEC and HD-FEC thresholds

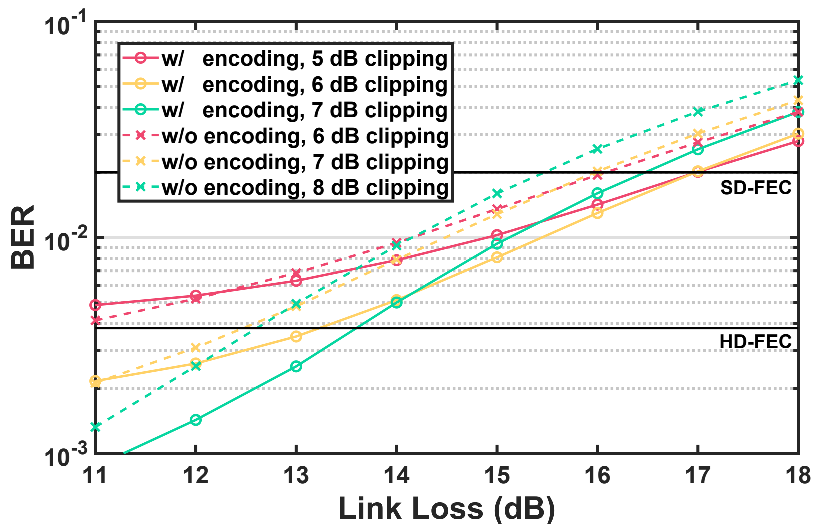

Figure 6.8: Dependence of calculated BER on the link loss under different clipping ratios, with both FFT-encoded DSCM systems and original uncoded DSCM systems. The link loss is fixed at 15 dB.

respectively. It is proved that the PAPR reduction can be translated to the extension of the power budget in the transmission system. Another interesting finding is that the optimal clipping ratio differs between the SD-FEC and HD-FEC thresholds. At high noise levels (SD-FEC), a lower clipping ratio performs better since it has a relatively large ROP so the SNR at the receiver increases. But at low noise levels (HD-FEC), since the electrical noise from the PDs is no longer dominant, the increase in SNR cannot compensate for the distortion brought by a low clipping ratio. Hence, the signal with a high clipping ratio becomes more favored.

Although the FFT encoding is capable to reduce the PAPR and improve the performance, one can observe in Fig. 6.6 that the value of PAPR reduction for different sequences fluctuates between 0.572 dB and 1.764 dB, depending on the seed of the PRBS sequence. Therefore, the sequences with the minimum and maximum PAPR differences are also tested together with the baseline PRBS sequence that is used for previous studies except for Fig. 6.6. In

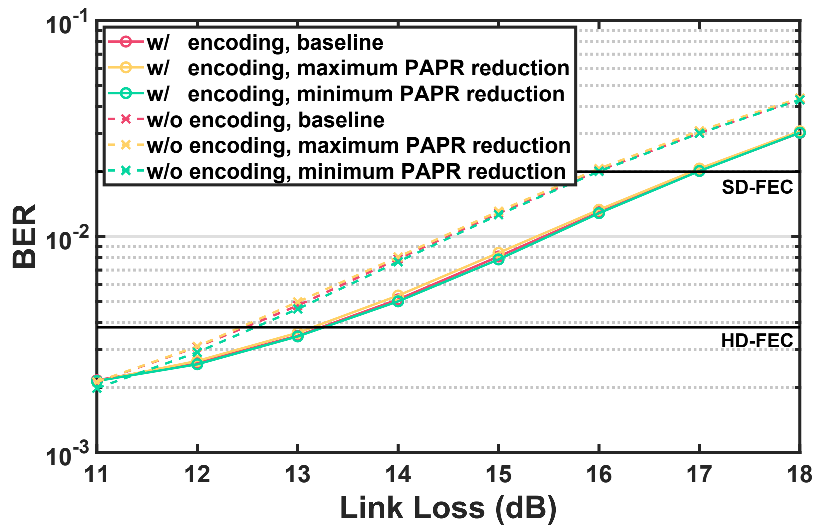

Figure 6.9: Dependence of calculated BER on the link loss using the baseline bit sequence and the two realizations with minimum and maximum PAPR reduction in Fig. 6.6.

Fig. 6.9, the results show that the effectiveness of the FFT encoding scheme is not affected by the difference in values of PAPR reduction since their behaviors are indistinguishable. The PAPR of a single sequence cannot be directly used to predict the performance. What matters most is the level distribution of transmitted samples.

6.3.2 Nonlinear signal pre-mapping

Consider an ideal transmitter model where there is no bandwidth limit and no need for pre-emphasis. The nonlinearity of the optoelectronic components in the transmitter can then be regarded as a memoryless distortion to the normalized in-phase and quadrature sequences output by the DACs $s_{\mathrm{I}}(n)$ and $s_{\mathrm{Q}}(n)$:

$$\begin{cases} s_{\mathrm{I}}^{\mathrm{o}}(n) = f_{\mathrm{nl,I}}(s_{\mathrm{I}}(n)), \\ s_{\mathrm{Q}}^{\mathrm{o}}(n) = f_{\mathrm{nl,Q}}(s_{\mathrm{Q}}(n)), \\ s_{\mathrm{I}}(n), s_{\mathrm{Q}}(n), s_{\mathrm{I}}^{\mathrm{o}}(n), s_{\mathrm{Q}}^{\mathrm{o}}(n) \in [-1, 1], \end{cases} \tag{6.9}$$

where $s^{\mathrm{o}}_{\mathrm{I}}(n)$ and $s^{\mathrm{o}}_{\mathrm{Q}}(n)$ are the normalized sampled in-phase and quadrature amplitudes of the optical signal. In this way, the distortions $f_{\mathrm{nl,I}}$ and $f_{\mathrm{nl,Q}}$ are both monotonic mappings from [-1, 1] to [-1, 1]. In this work, it is assumed that $f_{\mathrm{nl,I}} = f_{\mathrm{nl,Q}} = f_{\mathrm{nl}}$. Let us assume that there exists the inverse function of f_{nl}:

$$g = f_{\mathrm{nl}}^{-1}. \tag{6.10}$$

Therefore, the nonlinear pre-mapping method we propose is a process of finding the function g and applying it to the signal before sending it to the DAC. Since clipping defines the amplitude bounds of the signal, the pre-mapping needs to be inserted after the clipping so that the normalization of the input signal makes sense. Meanwhile, this block cannot be placed after the quantization since it is not a mapping from integers to integers. Therefore, the pre-mapping process is strictly placed between the clipping and the quantization as shown in Fig. 6.5.

In the simulation, we consider an ideal case when the inverse function g can be accurately obtained. Suppose the only source of nonlinearity is the sinusoidal transfer function of the MZM. Then f_{nl} is given by:

$$f_{\mathrm{nl}}(x) = \sin\frac{\pi x}{2}, x \in [-1, 1]. \tag{6.11}$$

Clearly, its inverse function is given by:

$$g(x) = f_{\mathrm{nl}}^{-1}(x) = \frac{\mathrm{arcsin(x)}}{\pi/2}. \tag{6.12}$$

We apply the pre-mapping $g(x)$ to the clipped samples and set $V_{\mathrm{RF}}/V_{\pi} = 1$. The bandwidth limit effect of the DAC channels is simulated by low-pass Gaussian filters with a 3-dB cutoff frequency of 50 GHz in the transmitter. The results are shown in Fig. 6.10.

At $V_{\mathrm{RF}}/V_{\pi} = 1$, the distortion to the signal seriously damages the performance. After

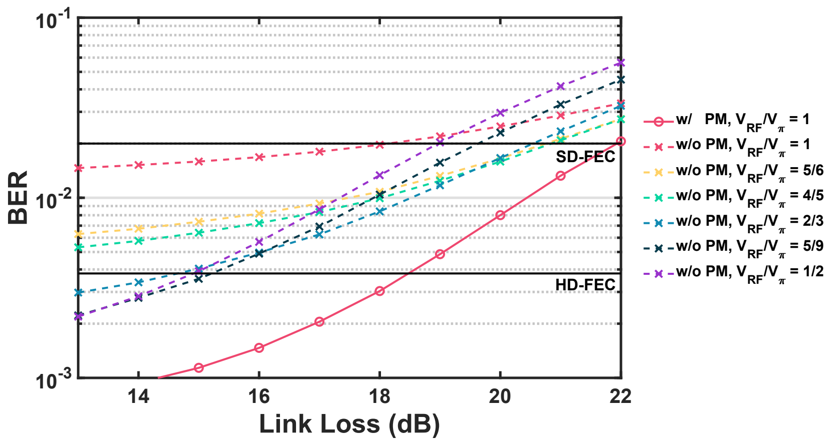

Figure 6.10: Dependence of calculated BER on the link loss with and without nonlinear pre-mapping. In the case without pre-mapping, different V_{RF}/V_{π} are simulated. PM: pre-mapping.

applying the nonlinear pre-mapping, the BER is largely reduced, proving that the algorithm functions as expected in the DSCM system. However, the performance can also be improved by only using the linear region of the transfer function. Therefore, V_{RF}/V_{π} is also swept to examine the limit of the DSCM system without pre-mapping. The results are also displayed in Fig. 6.10.

From the results, one can see that when $V_{\mathrm{RF}}/V_{\pi} = 4/5$, the system achieves the best receiver sensitivity at the SD-FEC threshold. For the HD-FEC threshold, a smaller ratio $V_{\mathrm{RF}}/V_{\pi} = 5/9$ is preferred to reach the best performance since the system becomes more intolerant of nonlinear distortion. Using the optimized ratios at both thresholds as benchmarks, the pre-mapping still outperforms with a gain of 3.232 dB with HD-FEC, and a gain of 1.088 dB with SD-FEC. Note that the pre-emphasis can affect the pre-mapping since the signals will go through the band-limited DAC channels before the sources of nonlinearity, including the RF amps and the modulators. Multi-dimensional pre-mapping can be a solution to this issue, but that is out of the scope of this work. Nevertheless, this study has shown the effectiveness of the pre-mapping scheme with the presence of slight band limitations and pre-emphasis, specifically an 80 GBd signal with 0.1 roll-off and DAC channels with 50 GHz 3-dB bandwidth.

6.3.3 Overall transceiver structure and modification on original DSP

The overall data flow and DSP blocks after inserting the proposed algorithms are displayed in Fig. 6.5. One can see that the FFT encoding and the nonlinear pre-mapping operate independently of each other. Note that both algorithms require low computational complexity. The FFT encoding only includes a single stage of FFT, while the pre-mapping can be implemented through a LUT once it is optimized.

With the FFT-encoded symbols, several original DSP blocks are affected, since the FFT operation eliminates the QAM pattern of the symbols in all the subcarriers. For instance, traditional FOC algorithms based on fourth power operation and Fourier transform rely on the $\pi/2$ phase ambiguity of the square QAM constellation. Therefore they are likely to fail if directly applied to the FFT-encoded signal. One possible solution can be inserting an uncoded pilot QAM symbol sequence before the coded information in each data block.

Alternatively, we propose another FOC algorithm that is blind and only uses the encoded symbols, as shown in Fig. 6.5. Suppose the k+1-th subcarrier after matched filtering are $\hat{s}_k^{\mathrm{Rx}}(n)$. These signals do not have the patterns of QAM symbols. If there is no FO, the original QAM symbols can be recovered by the IFFT decoder through a simple IFFT operation after the equalizers. Therefore, if we temporarily conduct the IFFT operation to signal before the equalizers, the output can be utilized to coarsely estimate the FO, which is similar to the FOC in traditional coherent DSP. Moreover, since all the subcarriers share the same FO, only one IFFT output out of N sequences is needed. Therefore, we choose the one with the least complexity, which is the recovery of the first subcarrier. Consider the following IFFT operation:

$$s_k^{\mathrm{Rx}}(n) = \frac{1}{N}\sum_{l=0}^{N-1} \hat{s}_l^{\mathrm{Rx}}(n) e^{j\frac{2\pi kl}{N}}. \tag{6.13}$$

When $k = 0$, the equation becomes:

$$s_0^{\mathrm{Rx}}(n) = \frac{1}{N}\sum_{l=0}^{N-1} \hat{s}_l^{\mathrm{Rx}}(n), \tag{6.14}$$

One can see that is just an averaging process. Since the FO estimation is based on Fourier transforming the fourth powers of the samples and obtaining the peak frequency, only the summation of the samples is enough, which further reduces the computational complexity. The detailed performance and evaluation of such a technique are not within the scope of this work. However, this method is applied in the experiments for encoded DSCM systems and the FOs can be accurately estimated and compensated.

The equalizer suffers from the same issue that DD-LMS equalizers can not be used since the target symbols are not QAM symbols. In this work, we apply training-symbol-based LMS equalizers for all symbols to reach the highest performance. In practice, the pre-convergence of equalizer taps can be done with the uncoded pilot symbols before the encoded sequence, while the adaptive function can be achieved by inserting another series of pilot QAM symbols between the encoded information sequence with certain intervals, i.e. 1 pilot symbol per 32 transmitted symbols.

6.4 Experiment and discussion

6.4.1 Experimental setup

The setup built for the experiment is shown in Fig. 6.11. The optical carrier is generated by an external cavity laser (ECL) with 15.5 dBm optical power and 1553 nm operating wavelength. The carrier is sent to a silicon photonics IQ-MZM through an on-chip grating

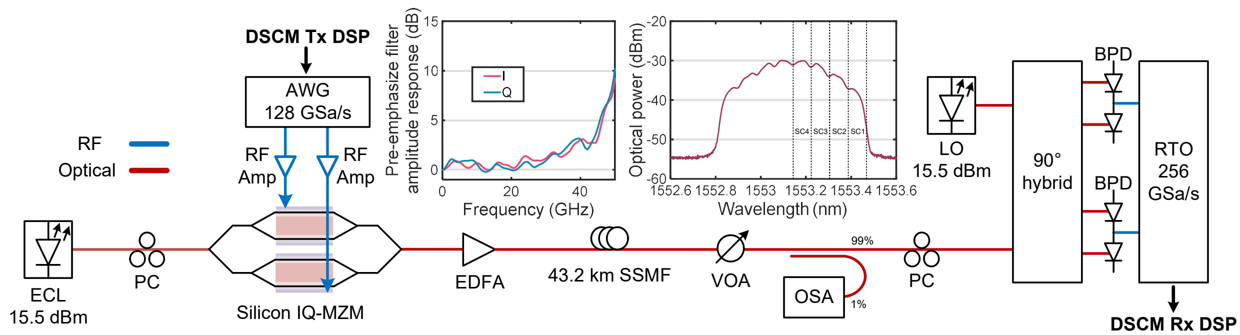

Figure 6.11: The experimental setup. The left inset shows the amplitude response of the pre-emphasis filter. The right inset demonstrates the optical spectrum of a 72 GBaud DSCM system before the receiver, with indications of the locations of several subcarriers.

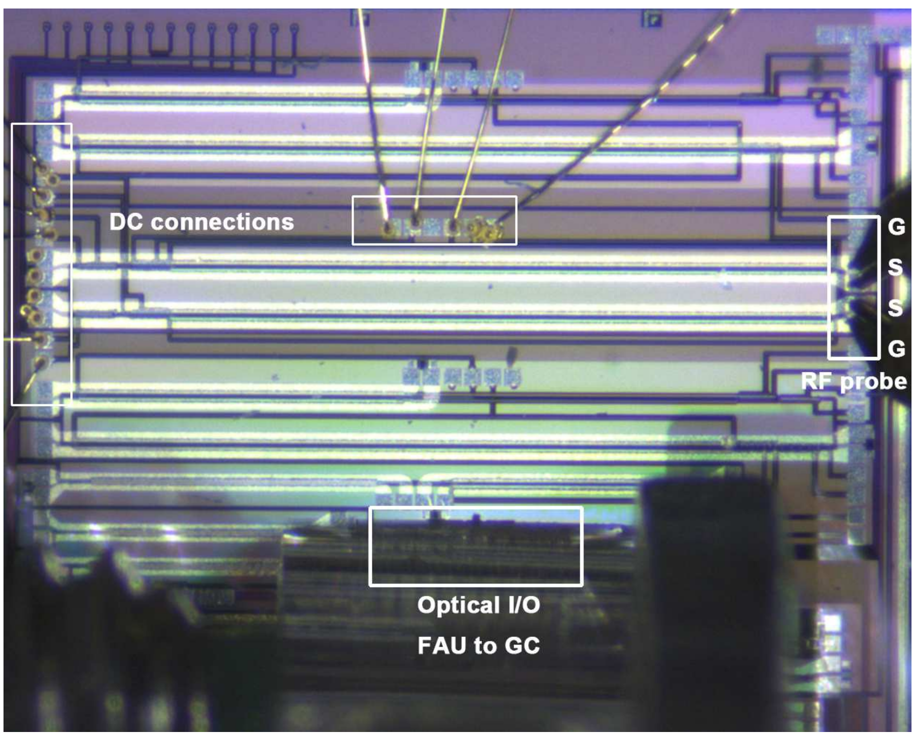

Figure 6.12: Probing stage for the silicon IQ-MZM. DC: direct current.

coupler, so a PC is needed to maximize the optical power coupled to the die. The silicon modulator used here is a 4 mm IQ-MZM and its detailed characterization is described in

[49, 176]. Regarding the general configuration of the transmitted signal, single-polarization DSCM signals with 8 subcarriers are tested in the experiment. After the transmitter DSP illustrated in Fig. 6.1 or Fig. 6.5, the signals are output by two 128 GSa/s DAC channels and magnified by RF amplifiers with ~45 GHz cutoff frequency and 26 dB gain. The amplified RF signals are then applied to the silicon IQ-MZM. A microscope image of the probing stage is shown in Fig. 6.12. Then the optical signal is amplified by a booster erbium-doped fiber amplifier (EDFA) to compensate for the coupling loss from the die and the dynamic loss of the modulator. Note that the operating mode of the EDFA changes as the experiment proceeds, and the reasons will be explained later. After optical amplification, the signal is sent to the channel, which is either a 43.2 km SSMF, or a B2B connection. At the receiver side, the signals first pass a variable optical attenuator (VOA) so that the link loss can be adjusted. The VOA is followed by a 1x2 99/1 coupler, the 1% port of which is connected to an optical spectrum analyzer (OSA) for monitoring. Meanwhile, most power of the signal is guided to the 90° hybrid via a PC due to the single-polarization feature of the system. Coherent detection is conducted in the hybrid with another 15.5 dBm ECL as the LO operating at the same wavelength as the transmitter laser. Finally, the optical field is reconstructed and captured by the BPDs and the real-time oscilloscope (RTO) with a sampling rate of 256 GSa/s.

6.4.2 Experimental results

We first experiment with 72 GBaud DSCM transmission with an average spectrum efficiency of 5 bit/s/Hz, corresponding to a total line rate of 360 Gbps. The reason for choosing such a rate is to keep the BER values close to the SD-FEC threshold of 2e-2. The proposed algorithms are tested both individually and jointly.

FFT-based subcarriers encoding

In an ideal transmission system without any bandwidth limit, we should compare the performance of the conventional DSCM system and FFT-encoded DSCM system, both with uniform 32QAM modulation for all the subcarriers. However, due to the fading effect at high frequency, as shown in the right inset of Fig. 6.11, the power varies for each subcarrier, resulting in different SNRs. Specifically in this case, the side sub-channels (SC1 and SC8) are too noisy for 32QAM that some of the DSP might even fail, and the results will become meaningless. Although methods such as PCS can be employed to optimize the information entropies for each subcarrier, they add extra complexity to the system, which is contrary to the idea of simple implementation in this work. Therefore in conventional uncoded DSCM systems, we manually balance the BERs of subcarriers by bit-loading. Here the modulation formats are chosen as [16 32 32 64 64 32 32 16] QAM for the 8 subcarriers, respectively. Note that the 'manual bit-loading' in this work refers to the process of manually choosing the modulation-format combination with the best performance under the same overall spectral efficiency as defined.

However, for the FFT-encoded system, since each received subcarrier before decoding contains the same amount of information from the original subcarriers, there will be a noise-averaging effect that the BERs of all the subcarriers after decoding have almost the same values. Therefore, 32QAM modulation is adopted for all sub-channels for the encoded system. This represents another advantage for the FFT-encoded system since the entropy optimization is easier.

In this study, the EDFA operates at constant-power mode with 1 dBm output power, so that the electrical noises from the BPDs are kept the same. Both systems are optimized by sweeping the clipping ratio, through an optical B2B channel. The results are shown in Fig. 6.13. One can observe that the curve of the encoded system shifts about 1 dB to the left compared to that of the uncoded system, in terms of clipping ratio. The 1-dB shift of

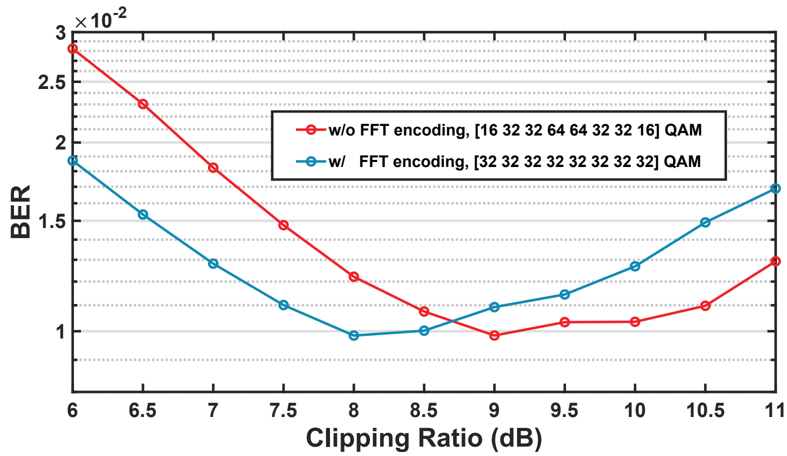

Figure 6.13: Dependence of measured BER on the clipping ratio for both encoded and uncoded systems, over an optical B2B channel.

the optimum point of the clipping ratio matches the simulation well. However, the optimum value of BER is not lower with the encoded system, which differs from the simulation. The reason is that manual bit-loading also improves transmission performance. Therefore, one should regard this study as a comparison between the FFT-encoded system and the bit-loaded system. These results also provide the optimal clipping ratio for the following studies.

Nonlinear signal pre-mapping

Though we observe huge gains from the simulation with the nonlinear signal pre-mapping, the assumption there is too ideal. The simulation results represent the upper bound of the gain provided by the pre-mapping, because in practice, the distortion to signals by transmitter nonlinearity cannot be perfectly obtained, especially with DSCM systems. In other words, both $g(x)$ and the $f_{\mathrm{nl}}^{-1}(x)$ cannot be accurately calculated. Therefore, we propose to use a simple polynomial function $g_{\mathrm{p}}(x)$ to approximate $g(x)$ in the experiment:

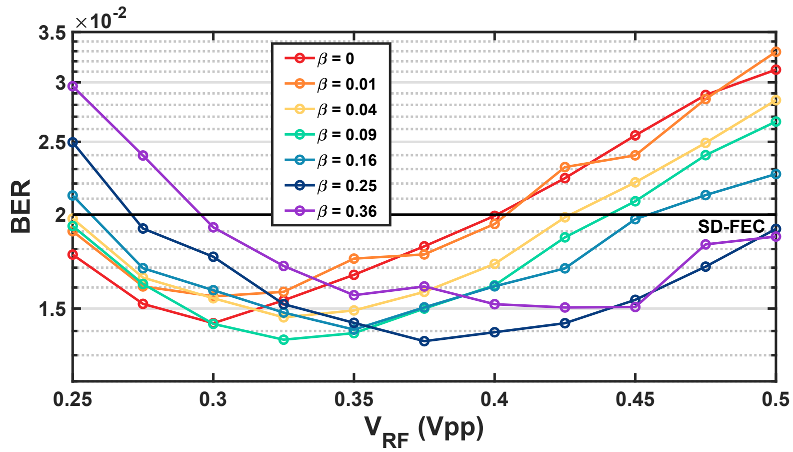

Figure 6.14: Dependence of measured BER on the voltage swings of DAC channels over an optical B2B channel, under varying degrees of nonlinear signal pre-mapping.

$$g_{\mathrm{p}}(x) = \frac{1}{1+\beta}(x+\beta x^3), x \in [-1,1], \beta > 0. \tag{6.15}$$

$g_{\mathrm{p}}(x)$ is chosen since it is a third-degree Maclaurin polynomial for odd functions such as $g(x)$. With such an expression, the optimization of this pre-mapping function is straightforward as only a one-dimensional parametric sweep is needed for β. $g_{\mathrm{p}}(x)$ is expected to partially compensate for the device nonlinearity.

In the experiment, the transmitter nonlinearity is mainly determined by the voltage swing V_{RF} of the DAC channels that affect the distortion stemming from both the RF amplifiers and the MZM. With each V_{RF}, there exists an optimal β. Hence, it is an optimization problem with two parameters. We first perform a two-dimensional parametric sweep of V_{RF} and β, the results of which are demonstrated in Fig. 6.14. The EDFA also operates at constant-power mode with 1 dBm output power, and the channel is optical B2B. The same bit-loading as used in the previous section is also adopted here.

From the results, it is inferred that the optimal β increases as the swing increases. It is within expectation since β should be larger to provide more pre-distortion to the signal when

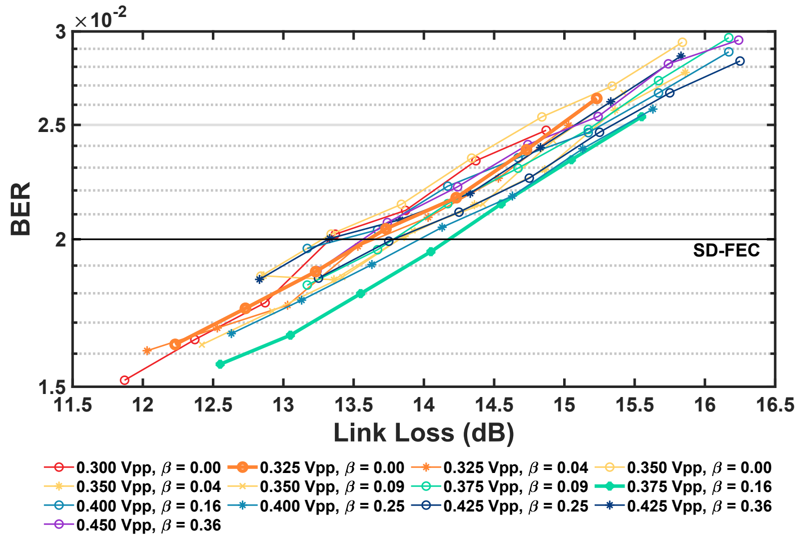

Figure 6.15: Dependence of measured BER on the link loss with different combinations of β and V_{RF}, over a 43.2-km SSMF link.

there is more nonlinearity. Furthermore, the performance at optimal V_{RF} with pre-mapping can be superior to that without pre-mapping ($\beta = 0$), specifically when $\beta = 0.09, 0.16, 0.25$.

To find the best combination of β and V_{RF}, a more rigorous methodology is adopted. Regardless of the output optical power from the silicon IQ-MZM, we use another VOA to decrease it to a constant power of -25.2 dBm as the input to the EDFA. We record this power difference and consider it as an extra link loss. Based on this setting, we sweep the link loss by tuning the VOA at the receiver side. Note that the EDFA output has been increased to 4 dBm since the channel is changed to 43.2 km SSMF. In this way, the optical noise from the EDFA maintains the same level with constant input power, the same as the electrical noise.

Several sub-optimal parameter pairs are selected based on Fig. 6.14. BER values as functions of link loss are then obtained by experiment and shown in Fig. 6.15. After comparing the maximum tolerated link loss for each combination of β and V_{RF}, the best configuration for systems both with and without the proposed algorithm is determined. The optimal V_{RF} is 0.325 Vpp without pre-mapping, and the best combination of pre-mapping is V_{RF} =0.375 Vpp and $\beta = 0.16$. Between the best results, the pre-mapping provides 0.572 dB gain in terms of link loss, which proves the effectiveness of the modified nonlinear pre-mapping even when the analytical form of $g(x)$ is unknown.

Combined performance

Since both algorithms have been evaluated and optimized, we test the system performance with the two DSP blocks acting simultaneously.

The EDFA setting is reset here. Although the previous configuration with the same input and output power guarantees the same noise level, it regards the transmitter as a constant-launch-power one. However, in practice, the launch power will change with different V_{RF}, especially when the booster EDFA is not present. Therefore, in this concluding study, the EDFA is set to constant-gain mode, so that the optical launch power depends on the input power into the EDFA. Unlike the previous study, now the link loss completely comes from the fiber channel, rather than the section before the EDFA.

Aside from the DSCM systems with either FFT encoding or the pre-mapping enabled, the system with the two algorithms implemented simultaneously is also evaluated. Relevant parameters for each algorithm are kept the same as the optimum values obtained from previous studies, including β, V_{RF}, and the clipping ratio.

The results are presented in Fig. 6.16, where one can find that the total gain from the two algorithms combined is 0.409 dB compared to the benchmark system without the two proposed algorithms. When there is no pre-mapping applied, the FFT encoding tolerates 0.295 dB less in terms of link loss than the bit-loading method. Whilst the encoded system and the uncoded system with bit-loading behave similarly with the nonlinear pre-mapping added. The pre-mapping provides more gain for the FFT-encoded system than the uncoded system, which are 0.703 dB and 0.448 dB, respectively. Such an effect can be explained by the fact that the low PAPR of the encoded system leads to a larger portion of samples being distributed at relatively higher levels. Therefore, the encoded signal is affected more by the

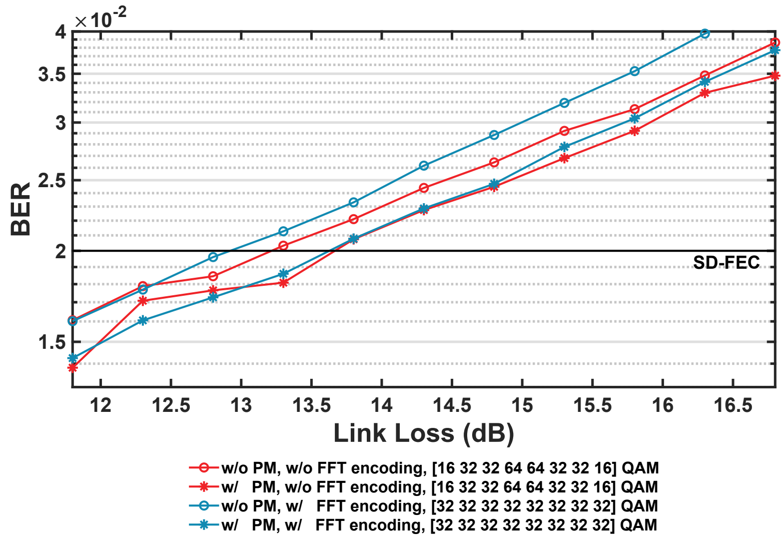

Figure 6.16: Dependence of measured BER on the link loss with either FFT encoding or the nonlinear pre-mapping, or two DSP blocks combined, compared with the unmodified DSCM system as the benchmark. The channel is a 43.2-km SSMF link.

device nonlinearity. The two algorithms are not only compatible with each other, but also generate extra gain when implemented together.

Re-characterization at lower noise level

In the previous experiments, we cannot perform a fair comparison by testing the systems with and without the FFT encoding. The reason is that the noise level at the SD-FEC threshold is too high for the side subcarriers if the same modulation format is kept for all the subcarriers. Therefore, we repeat the procedures with a lower noise level, assuming the systems operate with HD-FEC coding. Then a more comprehensive comparative study can be conducted by applying 3 different signals, namely DSCM with uniform 16QAM, DSCM with uniform 16QAM and FFT encoding, and DSCM with manual bit-loading. The total symbol rate is also modified from 72 GBd to 64 GBd. It is found in the experiment that a 16QAM subcarrier can be successfully recovered at every subcarrier. Specifically for the bit-

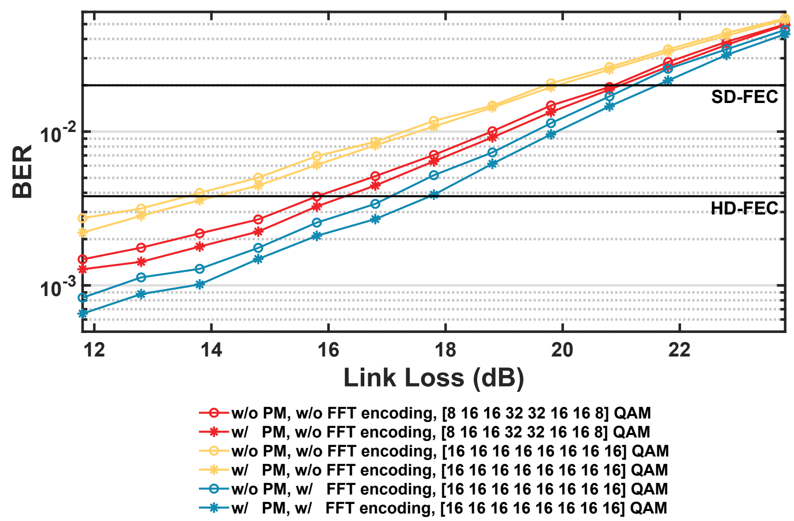

Figure 6.17: Dependence of measured BER on the link loss with various signal processing configurations over a 43.2-km SSMF link. The total symbol rate is updated from 72 GBd to 64 GBd, and the average spectral efficiency decreases from 5 to 4 bit/s/Hz.

loading, we choose [8 16 16 32 32 16 16 8] QAM for the subcarrier modulations to balance the BER of all 8 subcarriers. Meanwhile, the nonlinear pre-mapping is also evaluated, making a total of 6 configurations to be applied to the system. The parameters of the pre-mapping are kept the same as the previous test since the same DAC channels and RF amplifiers are used.

For all the systems, the DAC output swing is re-optimized at the HD-FEC threshold of 3.8e-3 BER. Then we captured the data of different systems under changing link losses. The BER trends are shown in Fig. 6.17. As anticipated, the DSCM system without pre-mapping, without FFT encoding, and without bit-loading performs the worst. Adding the pre-mapping provides a gain of 0.486 dB in terms of link loss. Whilst the bit-loading and the FFT encoding give similar gains to the DSCM system in the previous study, here the gain of the FFT encoding alone is 3.458 dB, larger than the gain of the manual bit-loading, 2.240 dB. The gain enhancement of the two algorithms combined is also observed in this study. When both algorithms are enabled, a 4.159 dB gain is achieved compared with the raw system. This value is larger than the addition of the gains by the two algorithms alone. Interestingly, although the parameters are not optimized at the SD-FEC threshold, the encoded system surpasses the manual bit-loading technique, which differs from our previous results. It shows that the performance gap is dependent on the signal features, such as modulation format and symbol rate.

6.5 Conclusion

We have uncovered some of the performance penalties when implementing a DSCM system on an imperfect optical transmitter. Moreover, employing a high-driving-voltage silicon-based MZM will further limit the performance of DSCM systems. To mitigate the performance degradation, we propose two transmitter DSP algorithms that can both be easily implemented. The first algorithm, FFT encoding, is shown capable of reducing the PAPR of the DSCM system by theory and simulation. While another DSP block named nonlinear pre-mapping is proposed to combat device nonlinearity in the transmitter. Both algorithms are evaluated in a C-band coherent transmission experimental setup with a silicon photonics IQ-MZM, at both SD-FEC and HD-FEC thresholds. With a 64 GBd, 4-bit/s/Hz DSCM signal, the gain achieved by the two algorithms combined reaches 4.159 dB compared with the raw system without any extra signal processing. Compared to the uncoded system with manual bit-loading, our proposed system still demonstrates a 1.919 dB gain in terms of link loss, using both algorithms. Moreover, we observe a gain enhancement effect of the two proposed algorithms, since the gain of the two DSP blocks combined, 4.159 dB is more than the addition of the two values of gain provided by each algorithm alone, which are 3.458 dB for the FFT encoding and 0.486 dB regarding the nonlinear pre-mapping, respectively. In summary, our proposed transmitter DSP designs facilitate the employment of the DSCM system on the CMOS-compatible silicon photonics transceiver, but not exclusively for the silicon platform since these algorithms work generally on any type of optical transmitter. Moreover, the PAPR reduction effect of the FFT encoding may also benefit long-haul optical communication systems with higher tolerance to fiber nonlinearity.

Chapter 7

Silicon photonics asymmetric self-coherent receiver

7.1 Motivation

As stated in Chapter 2, although coherent detection has been extensively employed in long-haul transmission and metro networks due to the high ESE and high receiver sensitivity, it is not favored in modern short-reach works because of its excessive cost and complexity. In comparison, IM/DD optical transceivers with lower power consumption are preferred in short reach.

However, the capacity-distance product of traditional IM/DD systems is inevitably limited by the power fading effect induced by CD [177]. To break such limitations, self-coherent detection (SCD) has been proposed to retrieve phase information with DSP while maintaining the simplicity and cost-effectiveness of DD [177–184]. Since the carrier is transmitted together with the signal, the SCD frees the receivers from the need for LO, while the beating between the carrier and signal enables the extraction of phase information.

Conventional SCD requires single-sideband (SSB) transmission, where only one side of the spectrum can be filled. For an SSB signal with an optical bandwidth B, the detection of such a signal requires an electrical bandwidth B. In comparison, the detection of a DSB signal with the same optical bandwidth B only requires $B/2$ electrical bandwidth, because the ESE of the DSB signal doubles compared to the SSB signal. Therefore, it is attractive for an SCD receiver to obtain the phase and reconstruct the field of a complex DSB signal due to higher efficiency in utilizing the electrical bandwidth of the receiver. In [185–187], carrier-assisted direct detection (CADD) is proposed to achieve such functionality. The system applies two BPDs and one single-ended PD to recover the fields of carrier-assisted DSB signals. Despite such a breakthrough in increasing ESE, the system design deviates from the simplicity of DD receivers due to the high hardware complexity. Aiming to simplify the receiver structure, the ASCD proposed in [188] only requires two single-ended PD for field reconstruction of complex DSB signals. It relies on an all-pass optical filter with a carefully designed phase response.

The photonic integration of optical transceivers is essential in practice, particularly for applications that face space limitations, such as high-density datacenter communications. With the advancement of various types of phase-diverse DD schemes, the community calls for realizing such systems on photonic integrated platforms, among which silicon photonics is a promising integration technology due to its high yield, high integration density, and low cost [189, 190]. In [191], a net 182-Gb/s silicon photonics CADD receiver was demonstrated with a net ESE per polarization of up to 5.2 b/s/Hz through an 80-km transmission. The previous capacity record is a net 258-Gb/s phase-diverse DD receiver [8] based on ASCD enabled by a Mach-Zehnder interferometer (MZI) as proposed in [192]. However, there has been no demonstration of integrated non-interferometric ASCD receivers, which is more suitable for multi-channel or colorless application as illustrated in [188].

Therefore in this chapter, we propose a design for silicon non-interferometric ASCD receivers for the very first time. The challenge is to find and design an on-chip all-pass optical filter with a desired phase response. We will introduce how we address this challenge in the following section.

7.2 Design and Simulation

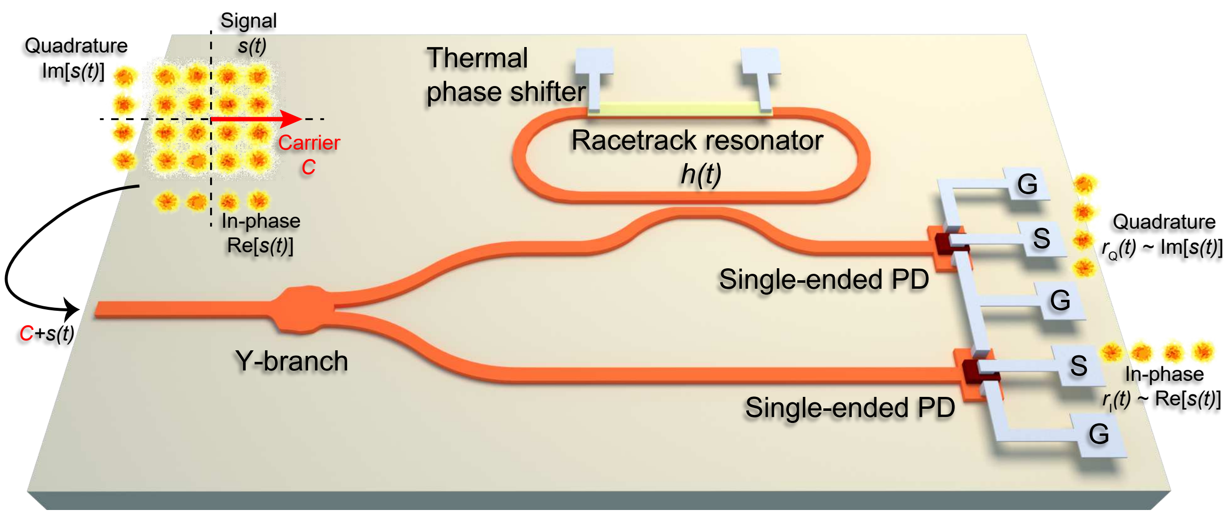

Figure 7.1: Schematic of the proposed integrated phase-diverse DD receiver.

The receiver schematic is shown in Figure 7.1. The proposed receiver consists of a Y-branch 3-dB power splitter, a racetrack resonator as the optical filter, and two integrated single-ended silicon-germanium PDs. The input optical signal is a carrier-assisted complex DSB signal. The PD in the lower reception path of the receiver recovers the in-phase component of the incident complex DSB signal, whereas the PD in the upper reception path having the optical filter recovers the quadrature component. Such signal recovery depends on the non-interferometric ASCD [188]. The photocurrents of PDs have the following expressions due to the square-law detection:

$$r_{\mathrm{I}}(t) = |C + s(t)|^2 + n_{\mathrm{I}}(t) = C^2 + 2C \cdot \mathrm{Re}[s(t))] + |s(t)|^2 + n_{\mathrm{I}}(t), \tag{7.1}$$

$$r_\mathrm{Q}(t) = |(C+s(t))*h(t)|^2+n_\mathrm{Q}(t) = |C*h(t)|^2+2\mathrm{Re}[\overline{C*h(t)}\cdot s(t)*h(t))]+|s(t)*h(t)|^2+n_\mathrm{Q}(t), \tag{7.2}$$

where $r_\mathrm{I}(t)$ is the received signal of the PD at the lower path without any filtering, and $r_\mathrm{Q}(t)$ is the received signal at the upper path with the optical filter. C and $s(t)$ are the transmitted carrier and the DSB complex signal. For simplicity, here we presume an in-phase carrier without loss of generality, which means C is real-valued. $n_\mathrm{I}(t)$ and $n_\mathrm{Q}(t)$ are the PD noises. $h(t)$ is the baseband impulse response of the optical filter. In Equation 7.1, the sequence captured by the lower PD consists of a DC component C^2, the desired in-phase component of the signal $2C \cdot \mathrm{Re}[s(t))]$, the signal-signal beating interference (SSBI) term $|s(t)|^2$, and the noise $n_\mathrm{I}(t)$. With a high enough carrier-to-signal power ratio (CSPR), the real part of the signal can be successfully extracted since the SSBI term becomes negligible. Note that the amplified spontaneous emission (ASE) noise is usually low in short-reach optical communication systems. Hence, the high optical signal-to-noise ratio (OSNR) makes a high CSPR acceptable. As for the quadrature component, Equation 7.2 gives the expression for the upper PD. Aside from the DC component, the SSBI term, and the noise, the carrier-signal beating term $2\mathrm{Re}[\overline{C*h(t)} \cdot s(t)*h(t))]$ differs from the lower path. The filter $h(t)$ is designed to cause different phase rotations for the carrier and the signal, so that part of the quadrature signal component is in-phase with the carrier and a linear term of the quadrature signal can be obtained from the carrier-signal beating. Therefore, the response of the upper path $h(t)$ needs to be optimized in order to retrieve the quadrature signal with high fidelity. Suppose the optical filter is expressed in the frequency domain as follows:

$$\mathcal{F}\{h(t)\} = H(f) = M(f) \cdot \mathrm{e}^{j\phi(f)}, \tag{7.3}$$

where $\phi(f)$ and $M(f)$ are the baseband phase and magnitude response of the optical filter. According to the working principle of ASCD, the system performance is determined only by the even part of $\phi(f)$ that is denoted as $\phi_\mathrm{e}(f)$, so that $\phi_\mathrm{e}(f) = \dfrac{\phi(f)+\phi(-f)}{2}$. It is revealed in [188] that the ideal response of the optical filter has the following expressions:

$$\phi_{\mathrm{e}}(f) = \begin{cases} \pi/2 + k\pi,\ f \neq 0, \\ 0,\ f = 0, \end{cases} \tag{7.4}$$

$$M(f) = 1, \tag{7.5}$$

where k is an arbitrary integer. It is inferred that the ideal optical filter is an all-pass filter with a $(\pi/2 + k\pi)$ notch in the phase response at $f = 0$.

The sharp edge of phase response makes it impractical to realize one of the ideal filters in practice. Note that the authors of [188] chose a tunable dispersion compensation module (TDCM) to build a CD optical filter as a proof of concept. The CD filter offers a near-all-pass magnitude response and a quadratic phase response. The phase increases in a monotonic manner from $f = 0$, so the frequency ranges where the phase approaches $\pi/2, \pi, 3\pi/2, ...$ can be loaded with complex DSB signals. However, with quadratic growth, the phase rotation speed increases as f grows larger, therefore multiple digital subcarriers are needed for high-symbol-rate transmission systems, adding complexity to transmitter DSP. More importantly, it is not feasible to create a large dispersion on integrated photonics platforms since it requires very long waveguides. According to [193], the experimentally obtained dispersion parameter of a 525 nm * 226 nm SOI strip waveguide ranges from 3700 to 4900 ps/(nm·km) in C-band. Supposing a dispersion parameter of 5000 ps/(nm · km), a 40 meters long waveguide is required to achieve a 200-ps/nm dispersion for the system. Even if such a long waveguide is fabricated, its excessive insertion loss will make it impractical for signal transmission.

Therefore, we propose to use an all-pass racetrack resonator as the optical filter. The phase response is mostly an odd function when the carrier frequency f_{c} is equivalent to the resonant frequency f_{r}, which makes the optical filter invalid. However, when the carrier is shifted from the f_{r} by $\Delta f = |f_{\mathrm{r}} - f_{\mathrm{c}}|$, the even component becomes non-zero. Here we model our resonator as displayed in Figure 7.2(a). The racetrack resonator consists of the coupler

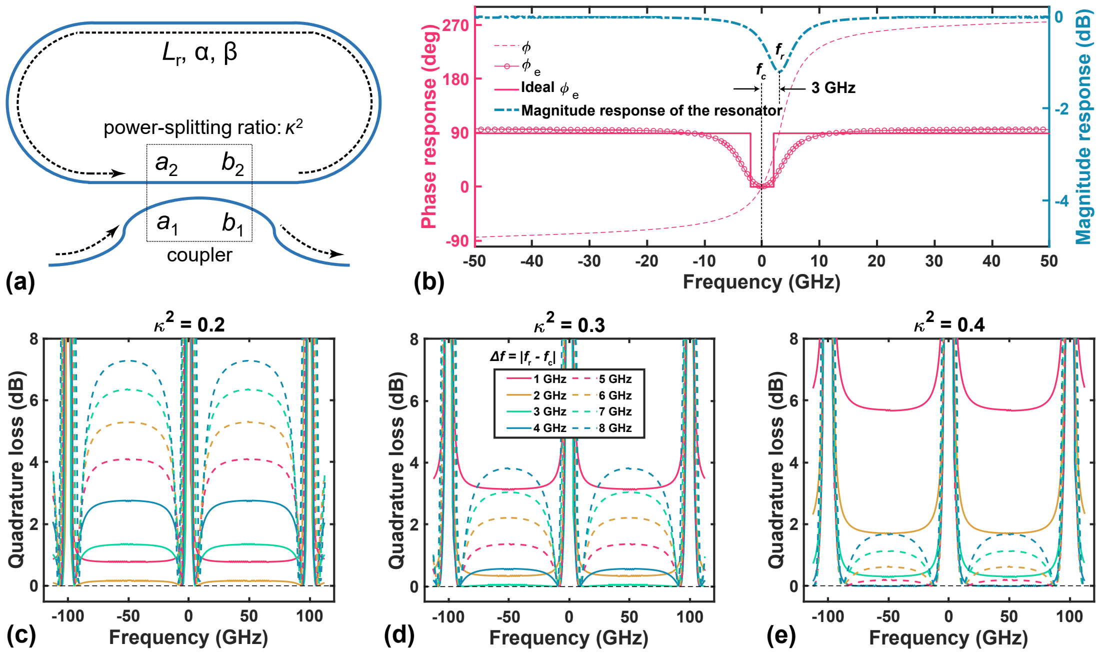

Figure 7.2: (a) Illustration of a racetrack resonator. (b) Optimized phase and amplitude response of the resonator with $\kappa^2 = 0.3$ and $\Delta f = 3$ GHz. (c-e) Dependence of quadrature loss on frequency shift Δf with (c) $\kappa^2 = 0.2$, (d) $\kappa^2 = 0.3$, and (e) $\kappa^2 = 0.4$. Note that (c), (d), and (e) share the same legend as displayed in (d).

with a power-splitting ratio of κ^2 and a racetrack waveguide with length L_r, power insertion loss α, and propagation constant β. Note that here κ is assumed to be real-valued rather than complex-valued without loss of generality. Then the coupler can be modeled with the following S-parameters:

$$\begin{bmatrix} b_1 \\ b_2 \end{bmatrix} = \begin{bmatrix} \sqrt{1-\kappa^2} & j\kappa \\ j\kappa & \sqrt{1-\kappa^2} \end{bmatrix} \begin{bmatrix} a_1 \\ a_2 \end{bmatrix}, \tag{7.6}$$

$$a_2 = \sqrt{\alpha} \mathrm{e}^{-j\beta L_\mathrm{r}} b_2, \tag{7.7}$$

Using the equations above, our desired transfer function b_1/a_1 can be calculated as follows:

$$\frac{b_1}{a_1} = \frac{\sqrt{1-\kappa^2} - \sqrt{\alpha}\mathrm{e}^{-j\beta L_\mathrm{r}}}{1 - \sqrt{\alpha(1-\kappa^2)}\mathrm{e}^{-j\beta L_\mathrm{r}}}, \tag{7.8}$$

We design the racetrack resonator with 100-GHz free spectral range (FSR), which is achieved by a 712.82 µm long racetrack formed by 500 nm * 220 nm SOI waveguides with oxide cladding. In Figure 7.2(b), a sub-optimal filter response is shown. With $\kappa^2 = 0.3$ and $\Delta f = 3$ GHz, the even component $\phi_\mathrm{e}(f)$ of the phase response fits well to the ideal response. Such resemblance guarantees the quasi-optimal performance of our receiver. Note that the ideal response in Figure 7.2(b) does not strictly follow Equation 7.4, since guard bands are needed to avoid the invalid frequency range around $f = 0$. Therefore, we add 2-GHz guard bands on each side of the spectrum. The amplitude response of the racetrack resonator is also shown to be low enough to be neglected.

To explain the impact of κ^2 and Δf on the receiver, here we first define the quadrature loss, $\mathrm{QL}(f)$, to evaluate the ability of the system to recover the quadrature component in the upper path, as a function of frequency.

$$\mathrm{QL}(f) = 20\log_{10}(\frac{1}{\sin\phi_\mathrm{e}(f)}), \tag{7.9}$$

In Figure 7.2(c), 7.2(d), and 7.2(e), the dependence of quadrature loss on Δf is given, with three different values of the power-splitting ratio κ^2. With $\kappa^2 = 0.2$ in Figure 7.2(c), the optimal Δf is around 2 GHz. The quadrature loss quickly drops as the frequency moves away from zero, therefore only a narrow guard band is needed. However, such a small κ^2 results in a low tolerance to frequency drifts, since the quadrature loss profile alters quickly as Δf changes. On the other hand, $\kappa^2 = 0.4$ provides high tolerance to frequency drifts as shown in Figure 7.2(e). However, the optimal quadrature loss profile at $\Delta f = 4$ GHz converges slowly to 0 dB, which means a wide guard band is required to maximize the performance. Hence, κ^2 $= 0.3$ and $\Delta f = 3$ GHz are selected since they balance the trade-off between the guard-band requirement and the tolerance of carrier frequency drifts. It is important to emphasize that the optimization of κ^2 in practice depends on the hardware parameters including the range of the laser frequency drifts and the cutoff frequencies of RF devices. $\kappa^2 = 0.3$ and $\Delta f = 3$ GHz are not the optimal pair of parameters in our experiments.

7.3 Experimental results

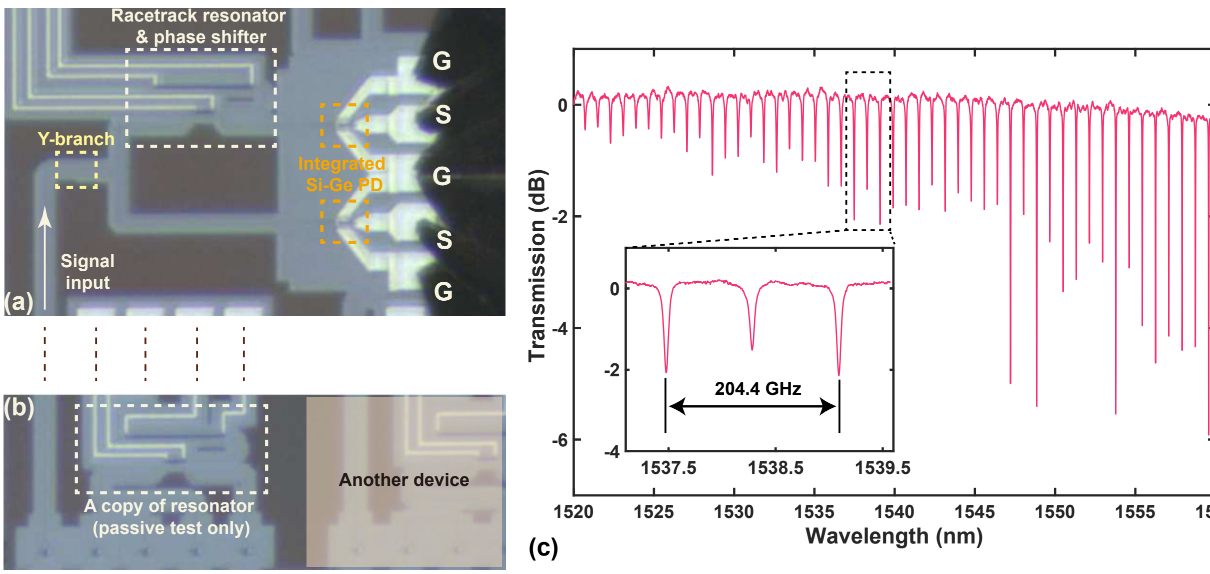

Figure 7.3: (a) Microscope image of the circuit under test. The PDs are probed by a 40-GHz GSGSG RF probe on the right-hand side. (b) Microscope image of the optical inputs/outputs and a copy of the resonator for passive measurement. (c) Measured transmission spectrum of the resonator only, from 1520 to 1560 nm.

The circuit is fabricated on the 220-nm SOI platform by AMF. For devices other than the resonator, we choose to use the 28G PD from the AMF process design kit (PDK) and the Y-branch from [194] in the circuit. The PD has 3-dB bandwidth of approximately 20 GHz, and the responsivity is about 0.9 A/W. The microscope image of the circuit is shown in Figure 7.3(a). Note that thermo-optic phase shifters are integrated on top of the resonator waveguide and the coupler to add tunability of resonant wavelengths and power-splitting ratio κ^2. However, both phase shifters are not used in the following experiments, because the wavelength of the laser in our setup can also be tuned, and the κ^2 of the fabricated coupler does not deviate too much from the designed value.

Before the transmission experiment, it is necessary to characterize the racetrack resonator itself as the key passive component. Therefore, a copy of the resonator is placed along each receiver circuit as demonstrated in Figure 7.3(b). 7.3(c) is the measured transmission spectrum of the racetrack resonator alone. The measured spacing between the two resonant frequencies is 204.4 GHz, slightly larger than the expected 200 GHz. Such a difference can be caused by fabrication errors, which lead to a deviated waveguide profile from simulation results. Nevertheless, it does not affect the following proof-of-concept experimental works. Notice that the transmission notches from 1520 nm to 1546 nm are all below 3 dB. Such a spectrum indicates that even the worst frequency points have less than 3 dB information loss, which guarantees that most of the signal power can be captured by the PD in the receiver.

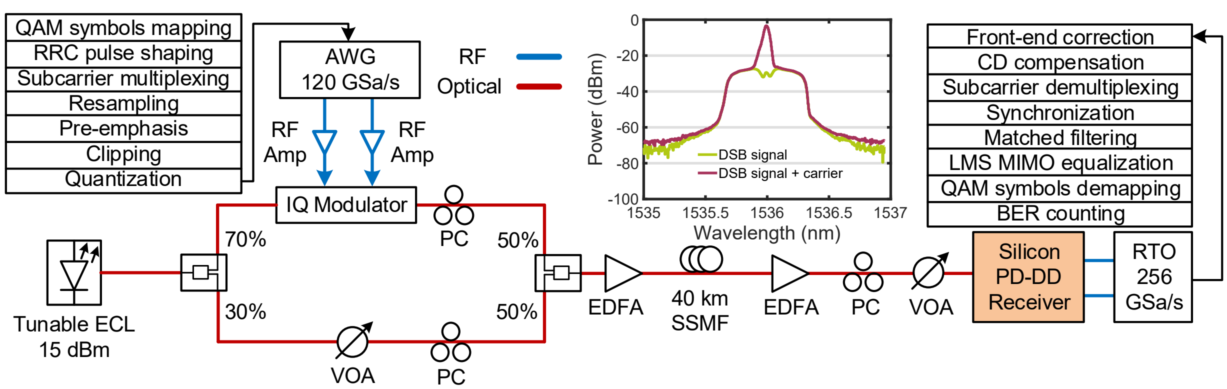

Figure 7.4: Experimental setup. The transmitter and the receiver DSP are completely compatible with conventional coherent systems. Inset shows the optical spectra of the transmitted DSB complex signals with a 0.05-nm wavelength resolution. PD-DD: phase-diverse direct detection.

The experimental setup for the transmission system is shown in Figure 7.4. A tunable C-band ECL is used as the continuous-wave (CW) optical source, operating at 15 dBm output power. Then the light is split by a 70/30 power splitter to generate the signal and the carrier, respectively. 70% of the light is then modulated by a 30-GHz Indium-phosphide (InP) IQ modulator driven by the amplified DSB complex signals from the 120 GSa/s arbitrary waveform generator (AWG). The RF amplifier used in the setup is the 55-GHz model, SHF S807 C. Meanwhile, the other 30% of the light passes through a VOA for the system to adjust the CSPR. Both paths are equipped with a PC for polarization matching before merging at the following 50/50 power splitter. The carrier-assisted DSB signal is then pre-amplified by an EDFA. After 40-km transmission through SSMF, the signal is amplified again by the receiver EDFA. As shown in Figure 7.3(b), vertical grating couplers (GC) are used as on-chip optical input/output ports. Since the GC is a polarization-sensitive device, the polarization state of the light needs to be adjusted by a PC to maximize the coupling efficiency to the chip. In practice, an edge coupler and an integrated endless adaptive polarization controller [195] can be utilized to achieve polarization insensitivity. A VOA is also inserted before the coupling for the characterization of ROP. The silicon phase-diverse DD receiver captures the received DSB signals and sends the in-phase and the quadrature components to two ADC channels on the 256 GSa/s RTO.

The DSP configuration is also shown in Figure 7.4. At the transmitter side, the bits are first mapped to QAM symbols, then shaped by an RRC filter with a roll-off factor of 0.05. Since guard bands are needed, two subcarriers are created and multiplexed with a frequency gap in between. Note that the frequency gap here equals twice the single-side guard band. Then the signal is resampled to the AWG sampling, followed by pre-emphasis filters to compensate for the band-limit effect of the RF amplifiers and the DAC channels in the AWG. Clipping and quantization are also executed to the signal before sending it to the AWG. At the receiver side, front-end correction and CD compensation are first conducted before demuxing the subcarriers. Then both subcarriers are synchronized with the transmitted signals, and pass through the matched RRC filters with the same roll-off factor. Next, a linear least-mean-square (LMS) real-valued equalizer is utilized to recover the symbols. To maximize system performance, here we apply a training-symbol-directed and MIMO equalizer using both subcarriers as inputs. Finally, the symbols are de-mapped to bits, and BER is calculated. Importantly, the DSP stacks at the transmitter and the receiver are completely compatible with conventional coherent transmission systems. Our proposed receiver design does not necessarily require SSBI cancellation or nonlinear equalization, and the two received sequences at the lower and the upper paths can be directly treated as in-phase and quadrature components. Our proposed design reduces the hardware complexity of the receiver without relying on heavy DSP.

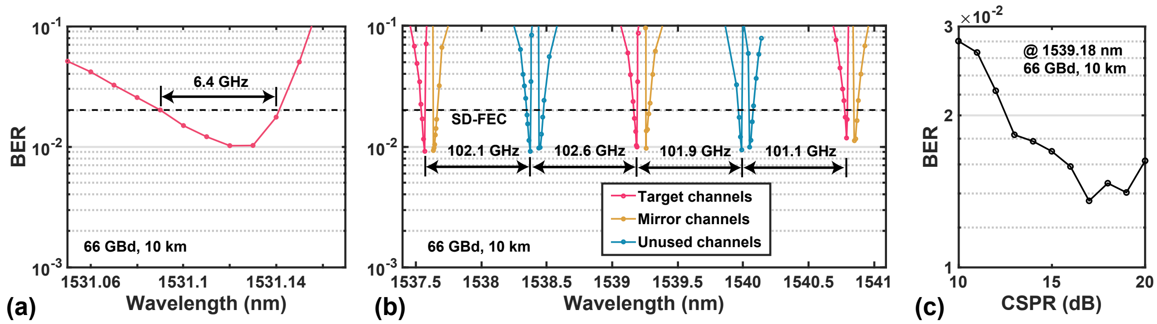

Figure 7.5: Experimental results with 16QAM 10-km 66-GBd transmission. (a) Dependence of BER on frequency in a single channel. (b) Dependence of BER on frequency including multiple channels. (c) Dependence of BER on CSPR.

We first characterize the receiver with 10-km fiber. A two-subcarrier 16QAM signal with a total symbol rate of 66 GBd is transmitted, and the CSPR is optimized to 17 dB as shown in Figure 7.5(c). The relatively high CSPR is due to the absence of SSBI estimation and cancellation. The guard band is optimized to be 5 GHz on each side. While the first EDFA at the transmitter side is removed for the 10-km test, the second EDFA is still indispensable to combat the high coupling loss to the chip. The output power of the second EDFA is optimized to 15 dBm. From Figure 7.2(c) it is revealed that the system performance is dependent on Δf. Hence, it is essential to characterize the sensitivity of the receiver circuit to frequency/wavelength drifts. In Figure 7.5(a), the wavelength of the CW source is swept from 1531.05 nm to 1531.17 nm with a step size of 0.01 nm, and the corresponding BERs are obtained. Considering a 20% SD-FEC with a pre-FEC BER of 2e-2, the system achieves a net 220 Gb/s transmission within a 6.4-GHz frequency range. Such tolerance relaxes the requirement for laser stabilization. Multiple-channel characterization is demonstrated in Figure 7.5(b), where the channel allocation is explained as well. A ~102-GHz periodicity is observed from the results, which corresponds to the periodic response of the resonator. Moreover, the channels exist in pairs due to the symmetry of the resonator response. In practice, only one of the two mirroring channels is needed. Also, instead of utilizing every channel with 100-GHz spacings, we only use the odd-number (or even-number) channels with 200-GHz channel spacing. The reason is that skipping the adjacent channels enables the current channel to make use of the ± 100-GHz spectrum rather than ± 50 GHz, as shown in Figure 7.2(c). Although doubling the FSR of the resonator have the same effect, it is not preferred since it will potentially double the guard band and reduce the ESE as well. It is worth mentioning that no active temperature control is adopted during the measurement, other than the air conditioner in the experimental lab.

Next, 40-km transmission is tested, where the first EDFA in Figure 7.4 is brought back with an optimal launch power of 5.2 dBm on the fiber. First, we evaluate our receiver performance considering a DWDM system in Figure 7.6(a), with a 66-GBd 16QAM signal. 14 channels are tested from 1527 nm to 1550 nm, and all the channels achieve a BER below 2e-2. As a result, net 220 Gb/s transmission with a 205-GHz-spacing 14-channel DWDM is successfully demonstrated. Furthermore, the channel spacing is stable around 205 GHz, which matches well with the passive characterization in Figure 7.3(c). Thus, the passive experimental result is enough to predict the channel spacing of the receiver in DWDM systems, and can be used as an indicator for optimization. Such results not only mean the system can operate at multiple wavelengths, but also enables the device-sharing structure proposed in [188] that further reduce the hardware complexity of the receiver. In Figure 7.6(b), the ROP of the receiver is swept at the channel of 1540.79 nm. It is shown that the

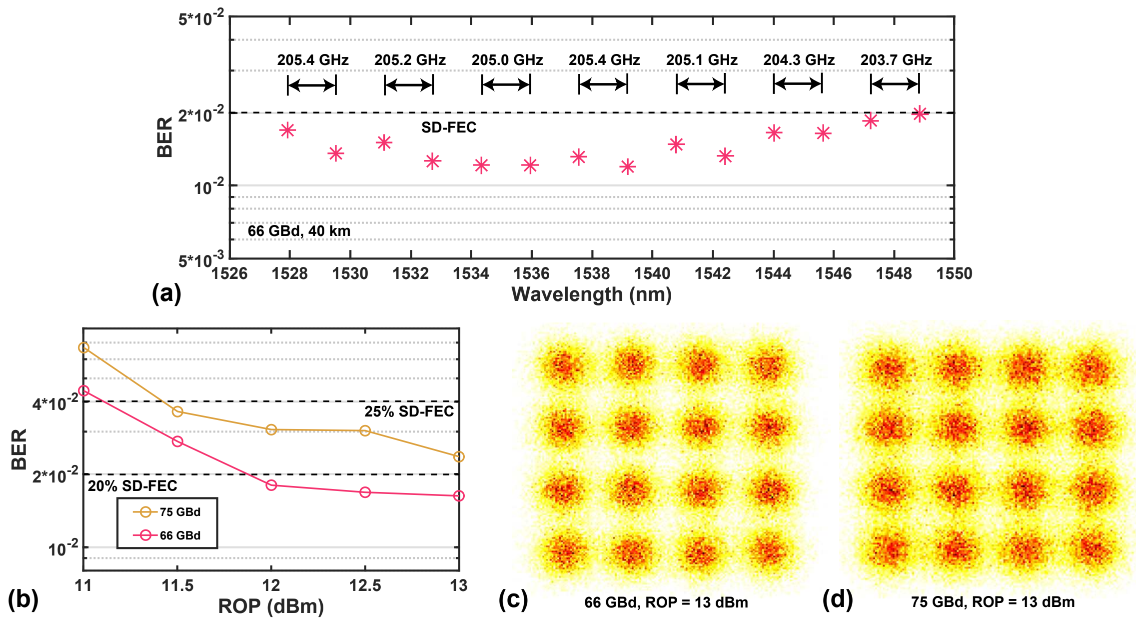

Figure 7.6: Experimental results with 16QAM 40-km transmission. (a) Available DWDM channels supporting net 220 Gb/s transmission from 1527 nm to 1550 nm. (b) Dependence of BER on ROP with 75 GBd and 66 GBd 16QAM signals. (c) Received constellation diagram of 66 GBd 16QAM signals at 13 dBm ROP. (d) Received constellation diagram of 75 GBd 16QAM signals at 13 dBm ROP.

BER of a 75 GBd signal is below the 25% SD-FEC threshold at 4e-2 with a >11.5 dBm ROP, resulting in a net bitrate of 240 Gb/s. The high required ROP is due to the coupling loss to the circuit, which is estimated to be 5.4 dB in the experiment. Note that the guard band is slightly adjusted to 4 GHz on each side for the 75 GBd signal. The received constellation diagrams of 66 GBd and 75 GBd 16QAM transmission at ROP = 13 dBm are given in Figure 7.6(c) and (d), respectively.

From Figure 7.2(c), it is inferred that when the optimized parameters and a large enough guard band are given, the intrinsic performance penalty of the receiver is negligible. This further increases the SNR of the receiver. Therefore, we increase the order of modulation format to 32QAM, to see if the proposed receiver supports such a high ESE. The results are

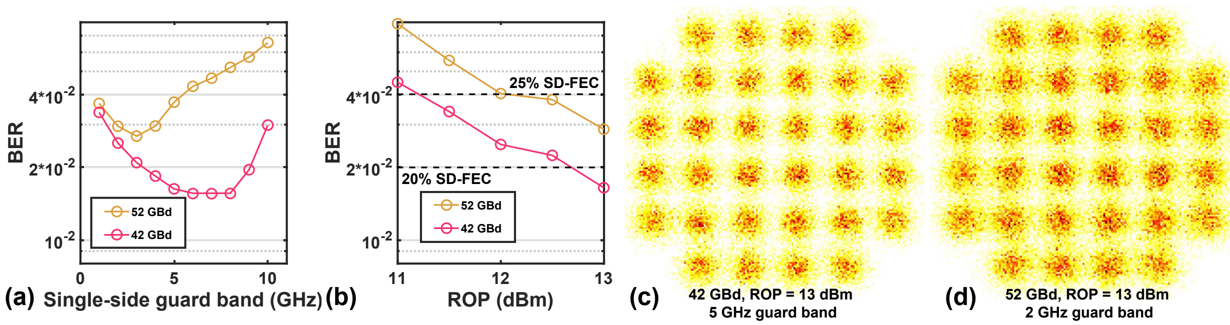

Figure 7.7: Experimental results of 32QAM 40-km transmission. Dependence of BER on (a) single-side guard band and (b) ROP with 52 GBd and 42 GBd 32QAM signals. Received constellation diagram of (c) 42 GBd 32QAM signals and (d) 52 GBd 32QAM at 13 dBm ROP, with different optimal guard bands.

shown in Figure 7.7. In Figure 7.7(a), the single-side guard band is scanned from 1 GHz to 10 GHz, and the optimal value for 42 GBd and 52 GBd 32QAM signals are 7 GHz and 3 GHz, respectively. When the guard band becomes too narrow, the signal spectrum will overlap with more non-ideal phase response near $f = 0$ as shown in Figure 7.2(b), causing imperfect optical field reconstruction of low-frequency components. On the other hand, if the guard band is too wide, the transmission performance will also be affected because of the RF bandwidth limitation of the system. The optimal guard band is the outcome of such a trade-off, and it depends on the symbol rate of the DSB signal. In this experiment, the 52 GBd signal is more sensitive to band extension than the 42 GBd signal since it covers more electrical spectrum. In Figure 7.7(b) where the ROP is swept, we apply guard bands of 5 GHz and 2 GHz rather than 7 GHz and 3 GHz for 52 GBd and 42 GBd transmission, in order to maximize the ESE with minimal influence on BER. At 13 dBm ROP, the 42 GBd system achieves a BER of 1.65e-2, which is below the 20% SD-FEC threshold of 2e-2. The result corresponds to a net 175 Gb/s transmission with a net ESE per polarization of 6.47 bit/s/Hz. As for 52 GBd transmission, a BER of 2.88e-2 is achieved at 13 dBm ROP, which is below the 25% SD-FEC threshold of 4e-2. This indicates a net 208 Gb/s transmission with a net ESE per polarization of 7.10 bit/s/Hz. Here, it is important to clarify that the single-side guard band is included when calculating the ESE.

We compare our results with the existing literature on integrated phase-diverse DD receivers in Table 7.1. Compared with its counterparts, our proposed receiver achieves a record net ESE of 7.10 bit/s/Hz per wavelength per polarization. Even with the general 20% SD-FEC at 2e-2, the 6.47 bit/s/Hz ESE is still higher than other integrated phase-diverse DD receivers, since our receiver can support modulation formats as high as 32QAM without largely reducing the symbol rate. Note that such results are achieved only by using all-linear equalization, without addressing the SSBI. This indicates that there is still space for the performance to be further optimized if a nonlinear Volterra equalizer is applied to combat SSBI or the SSBI is accurately estimated and eliminated.

Reference	Net ESE per λ per pol (bit/s/Hz)	Net bitrate (Gb/s)	Modulation format	FEC	Distance (km)	# of ADC channels	# of PDs
[191]	5.2	182	16QAM	25% SD @5.0e-2	80	3	5
[196]	4.6	162	16QAM	25% SD @4.0e-2	80	3	5
[8]	5.86	200	16QAM	20% SD @2.0e-2	40	2	2
[8]	5.31	258	16QAM	24% SD @4.5e-2	40	2	2
[197]	3.33	93.33	16QAM	20% SD @2.0e-2	80	1	1
[198]	3.87	130.71	Adaptive	7% HD @3.8e-3	2	2	2
[199]	3.39	224	16QAM	7% HD @3.8e-3	40	4	4
This work	7.10	208	32QAM	25% SD @4.0e-2	40	2	2
This work	6.47	175	32QAM	20% SD @2.0e-2	40	2	2
This work	5.53	240	16QAM	25% SD @4.0e-2	40	2	2
This work	5.55	220	16QAM	20% SD @2.0e-2	40	2	2

Table 7.1: Summary of experimental results of integrated phase-diverse DD receivers

7.4 Conclusion

We have proposed a novel silicon photonics phase-diverse DD receiver based on ASCD. This integrated receiver has a hardware-efficient architecture that only two PDs and two ADC channels are needed to recover a carrier-assisted DSB complex signal. An on-chip racetrack resonator is designed and optimized to function as the optical filter of ASCD. The resonator exhibits a near-ideal response that minimizes the performance penalty. In addition, DWDM system is enabled due to the periodic response of the resonator. As a result, the receiver achieves a net 240-Gb/s 16QAM 40-km transmission with a BER below the 4e-2 threshold of a 25% SD-FEC. To verify the compatibility with DWDM system, the receiver is tested in 14 channels with 205 GHz spacing from 1527 nm to 1550 nm, and all channels are proven to support a net 220-Gb/s 16QAM 40-km transmission with a 20% SD-FEC operating below 2e-2 BER. Furthermore, 32QAM transmission is attempted to maximize the ESE of the receiver and we successfully demonstrate a net 208-Gb/s 32QAM transmission with a record net ESE of 7.10 bit/s/Hz. In all experimental demonstrations, the DSP stacks at the transmitter and the receiver are standard DSP stacks for coherent transmission where all-linear equalization is used. No extra DSP block such as SSBI cancellation or nonlinear Volterra equalizer is needed to achieve such a high ESE. This work provides an alternative cost-effective solution besides traditional coherent and IM/DD systems for large-capacity optical interconnects such as datacenter communication and 5G fronthaul.

Chapter 8

Discussion and Conclusion

8.1 Discussion

Before drawing the conclusion, we would like to discuss how our academic findings demonstrated in this thesis would benefit the development of optical communication and optical transceivers.

The most obvious contribution of our work is providing additions to the library of device and circuit designs for integrated silicon photonic transceivers. On the device level, we have designed three novel silicon photonic devices to improve the performance from various aspects, including the IL, ER, crosstalk, and bandwidth. Devices with high performance are the basis of high-quality telecommunication services enabled by optical transceiver modules. Also, we have demonstrated the robustness of our designs to fabrication errors and/or temperature changes. These are the among the most important traits for the devices to be practically applied in real-world products. The same statement can be drawn for our system-level works.

One can see that the three devices we proposed share the same enabling structure, the SWG. The study of SWG boomed in the last decade due to the advancement of fabrication process. The capability to fabricate finer features is the key for the researchers to conduct measurement for fabricated SWG structures. Therefore, besides the direct contribution to the device library, our device works contribute to the on-going study of SWG and show the rich functionality of SWG on silicon. We have proposed several innovative ways of utilizing SWG in different structures. For example, in Chapter 3, we reveal that inserting a SWG slot into MMI would change the fundamental principle of MMI to TMI, therefore decreasing the required length of the coupling region. In Chapter 4, we propose to make use of not only the SWG, but all three different regimes of the gratings to achieve large bandwidth TM-mode polarizer. In Chapter 5, we propose to use curved SWG as the lateral cladding for the waveguide crossing. Unlike the usual straight SWG, the curved SWG is shown to function better to reduce the IL and crosstalk when the light pass through the crossing. It is hard now to stably fabricate SWG with commercial CMOS foundries due its high requirement on minimum feature sizes. Nevertheless, the significant development and improvement of fabrication process in the past years tells us that one day, SWG could be commercially available, and our researches would be part of the foundation laid for SWG-based high-performance devices and circuits on silicon.

While devices are the basis for PICs, how to efficiently arrange and utilize the devices on the circuit or system level is also an important topic. Therefore in the second part of the thesis, we focus on the system level works on silicon platform. It is important to notice that for most of the existing works, they either study on the device level or the system level, making the designs of devices and systems very independent. Therefore, a very important perspective in the second part of this thesis is that we look at the transceiver from multiple levels simultaneously. We conduct system-level researches, but also from the perspective of devices. In Chapter 6, we study how the parameters of integrated modulators affect the quality of transmission systems, so that we provide insights for designers when designing silicon photonic transmitter circuits for DSCM transmission. In Chapter 7, the success of on-chip ASCD demonstration relies on the design of the racetrack resonator itself. It is very interesting to how the resonator parameters affects the recovery of DSB complex-valued signals. We are glad to show the advantages of that such a multi-layer and comprehensive methodology in the design of silicon PICs for high-speed optical interconnects.

Last but not least, we would like to discuss the extendibility of this thesis. The originality of the works in this thesis guarantees the potentials for future works following each chapter. We summarize some of the topics in the future work section as follows.

8.2 Future works

Based on the research demonstrated in this thesis, there exist possible topics and directions for further exploration optimization and/or exploration in these areas. In this final section, we explain several ideas of future works.

8.2.1 Devices

- The SWG-slot design can be extended to dual-polarization MMI on a 340-nm SOI platform. By carefully designing the parameters, the SWG slot could have the same effect on both TE and TM modes, which is easier to achieve on 340-nm high SOI waveguides. This leads to a polarization-insensitive design of 1310/1550 nm diplexer.

- From the simulation results of the broadband TM polarizer in Chapter 4, we observe that device cannot function well within part of the E-band. The cause of the PER notch in the E-band remains unclear. By bandgap analysis, it is shown that the location of the notch (1372 nm - 1410 nm) is covered by the TE0 bandgap. However, the reflection within this range is already weakened as reported by Fig. 4.4(b). We may consider it as a transitional regime between Bragg reflection and diffraction. Analyzing and eliminating the notch can be the future works for this TM-pass polarizer design.

- For the broadband silicon photonic crossing, the device can be further optimized by independently optimize the parameters of each grating ring. Advanced optimization algorithms can be applied. Also the current design suffers from relatively high reflection that disables the cascade of multiple crossings. Although decreasing the period of SWG will solve the issue, it is at the cost of reduced minimum feature size, which has higher requirements for the fabrication process. Therefore, other methods is desired without affecting the minimum feature size to limit the reflection.

8.2.2 Circuits and systems

- The nonlinear pre-mapping technique proposed in Chapter 6 is completely feedforward. In this work, no estimation of transmitter nonlinearity is conducted since it is hard to do when the nonlinearity is applied on a subcarrier-multiplexed signal rather than a single-carrier signal. This way, the algorithm needs to be optimized every time when a new system is built. The low-pass filtering effect of RF amplifiers and DAC channels further complicates the originally memoryless nonlinear effect at the transmitter. Therefore a nonlinearity error estimation algorithm specific for DSCM is desired. Methods to compensate for nonlinearity with ISI can be another topic to work on in the future.

- As shown in Chapter 7, the silicon ASCD receiver we propose is based on ring or racetrack resonators. This naturally causes the device to be temperature-sensitive which prevents the circuit to be applied in practice. Although we have characterized our fabricated receiver in terms of maximum tolerated wavelength shift, it is not large enough. The next topic related to this work could be to optimize or re-design the waveguide to make the device less sensitive to temperature change.

8.3 Conclusion

In this thesis, we introduce integrated silicon photonic transceivers and their role and value in modern communication infrastructure. The ever-increasing demand for data transmission constantly calls for innovation and evolution in integrated photonic transceivers to achieve high-capacity, low-cost, and energy-effective circuits and systems. Therefore, we propose several advanced designs of devices, circuits, and systems for improvement in various aspects. In each work, we develop the theories, run detailed simulations, and conduct experiments to prove the designs.

For device-level research, we focus on how to effectively utilize SWG in passive silicon photonic devices to achieve low loss, low crosstalk, high extinction ratio, and/or broad bandwidth. In Chapter 2, we propose to insert a SWG slot in the middle of an MMI coupler functioning as a 1310/1550 nm wavelength diplexer. Such a structure not only reduce the needed coupling length by index engineering and converting the MMI to a TMI, but also improves the IL and ER bandwidths at both wavelengths. In Chapter 3, we propose a broadband all-silicon TM polarizer. We carefully design the gratings to utilize different regimes of Bragg gratings for both TE and TM modes, extending the calculated operational bandwidth to 343 nm. In Chapter 4, we propose an ultra-broadband single-mode waveguide crossing on silicon that covers all the communication bands from 1260 nm to 1675 nm with low loss and low crosstalk. This is achieved by a novel curved SWG lateral cladding around the intersection point that reduces the index contrast for all wavelengths.

Moving from the scope of devices to circuits and systems, we propose systematic solutions to increase the capacity and reduce the power consumption and complexity of silicon photonic transmitters and receivers. In Chapter 6, we develop two low-complexity DSP techniques to improve the power budget of a coherent DSCM transmission system on a silicon photonic transmitter. In a 64GBd 8-subcarrier transmission experiment, the two algorithms combined increase the power budget by 4.159 dB at the HD-FEC threshold. In

Chapter 7, we demonstrate for the first time, a silicon photonic ASCD receiver that can recover the phase information of optical signals with simple direct detection. Using traditional all-linear coherent DSP, the fabricated receiver achieves a record 7.10 bit/s/Hz per wavelength and per polarization through 40 km SSMF.

In conclusion, this thesis provides ideas, concepts, methodology, and results that will pave the way for developing high-speed and energy-effective silicon photonic integrated optical transceivers in the future.

Bibliography

[1] J. Zhang, X. Li, Y. Hu, M. S. Alam, and D. V. Plant, "Spectrally Efficient Integrated Silicon Photonic Phase-Diverse DD Receiver with Near-Ideal Phase Response for C-Band DWDM Transmission," *Laser & Photonics Reviews*, vol. 18, no. 3, p. 2300623, 2024.

[2] J. Zhang, L. Xu, D. Mao, Y. D'Mello, Z. Wei, W. Li, and D. V. Plant, "Temperature-insensitive and low-loss single-mode silicon waveguide crossing covering all optical communication bands enabled by curved anisotropic metamaterial," *Nanophotonics*, vol. 12, no. 21, pp. 4095–4107, 2023.

[3] J. Zhang, E. Berikaa, R. Gutiérrez-Castrejón, M. S. Alam, F. Cavaliere, S. Lessard, Z. Wei, W. Li, and D. V. Plant, "PAPR Reduction and Nonlinearity Mitigation of Optical Digital Subcarrier Multiplexing Systems With a Silicon Photonics Transmitter," *Journal of Lightwave Technology*, vol. 41, no. 22, pp. 6957–6969, 2023.

[4] J. Zhang, L. Xu, D. Mao, Z. Xing, Y. D'Mello, M. Jacques, Y. Wang, S. Lessard, and D. V. Plant, "High-extinction-ratio and compact 1310/1550 nm wavelength diplexer on SOI platform based on an SWG-structured two-mode interference coupler," *IEEE Photonics Journal*, vol. 14, no. 2, pp. 1–6, 2022.

[5] J. Zhang, L. Xu, D. Mao, Y. D'Mello, W. Li, S. Lessard, and D. V. Plant, "All-silicon multi-band TM-pass polarizer on a 220 nm SOI enabled by multiplexing grating regimes," *Optics Express*, vol. 30, no. 1, pp. 326–335, 2022.

[6] J. Zhang, W. Li, Z. Wei, and D. V. Plant, "Enhanced broadband silicon waveguide crossing based on pso-processed swg cladding," in *IEEE Silicon Photonics Conference*, pp. ThP–12, IEEE, 2024.

[7] W. Li, L. Xu, Z. Wei, J. Zhang, D. Mao, Y. D'Mello, and D. V. Plant, "Silicon photonic broadband polarization-insensitive switch based on polarization-mode diversity conversion," *Optics Letters*, vol. 48, no. 17, pp. 4661–4664, 2023.

[8] Y. Hu, X. Li, D. Mao, M. S. Alam, E. Berikaa, J. Zhang, S. Bernal, A. Samani, M. E. Mousa-Pasandi, M. O'Sullivan, *et al.*, "Silicon photonic phase-diverse receiver enabling transmission of $>$ net 250 Gbps/λ over 40 km for high-speed and low-cost short-reach optical communications," *Journal of Lightwave Technology*, vol. 41, no. 12, pp. 3680–3687, 2023.

[9] Z. Wei, J. Zhang, W. Li, and D. V. Plant, "Active Learning-aided CNN-based Entropytunable Automatic Modulation Identification for Rate-flexible Coherent Optical System," *Journal of Lightwave Technology*, vol. 41, no. 14, pp. 4598–4608, 2023.

[10] Z. Wei, J. Zhang, W. Li, and D. V. Plant, "400-Gbps/80-km rate-flexible PCS-64-QAM WDM-CPON with pseudo-m-QAM chaotic physical layer encryption," *Journal of Lightwave Technology*, vol. 41, no. 8, pp. 2413–2424, 2023.

[11] W. Li, L. Xu, J. Zhang, D. Mao, Y. D'Mello, Z. Wei, and D. V. Plant, "Broadband polarization-insensitive thermo-optic switches on a 220-nm silicon-on-insulator platform," *IEEE Photonics Journal*, vol. 14, no. 6, pp. 1–7, 2022.

[12] Z. Wei, J. Zhang, W. Li, and D. V. Plant, "Time-variant entropy regulated multiple access for flexible coherent PON," *Optics Letters*, vol. 47, no. 19, pp. 5148–5151, 2022.

[13] D. Mao, Y. Wang, L. Xu, J. Zhang, E. El-Fiky, M. S. Alam, Y. D'Mello, S. Lessard, and D. V. Plant, "CMOS-compatible and temperature insensitive C-band wavelength (de-) multiplexer," *IEEE Photonics Technology Letters*, vol. 34, no. 14, pp. 769–772, 2022.

[14] D. Mao, Y. Wang, L. Xu, E. El-Fiky, M. Jacques, J. Zhang, M. S. Alam, A. Kumar, Y. D'Mello, and D. V. Plant, "Adiabatic coupler with nonlinearly tapered mode-evolution region," *IEEE Photonics Technology Letters*, vol. 33, no. 16, pp. 840–843, 2021.

[15] X. Li, M. O'Sullivan, Z. Xing, M. S. Alam, T. Hoang, M. Xiang, M. Zhu, J. Zhang, E. Elfiky, and D. V. Plant, "Asymmetric direct detection of orthogonal offset carriers assisted polarization multiplexed single-sideband signals," *Optics Express*, vol. 28, no. 3, pp. 3226–3236, 2020.

[16] D. Mao, Y. Wang, E. El-Fiky, L. Xu, A. Kumar, M. Jaques, A. Samani, O. Carpentier, S. Bernal, M. S. Alam, *et al.*, "Adiabatic coupler with design-intended splitting ratio," *Journal of Lightwave Technology*, vol. 37, no. 24, pp. 6147–6155, 2019.

[17] L. Xu, Y. Wang, D. Mao, J. Zhang, Z. Xing, E. El-Fiky, M. G. Saber, A. Kumar, Y. D'Mello, M. Jacques, *et al.*, "Ultra-broadband and compact two-mode multiplexer based on subwavelength-grating-slot-assisted adiabatic coupler for the silicon-on-insulator platform," *Journal of Lightwave Technology*, vol. 37, no. 23, pp. 5790–5800, 2019.

[18] J. Zhang, Z. Wei, S. Misak, A. Wissing, J. Liu, H. Andrade, A. Maharry, G. Gilardi, R. Kumar, G.-L. Su, A. Liu, Y. Akulova, J. F. Buckwalter, A. A. M. Saleh, L. Coldren,

C. L. Schow, and D. V. Plant, "First demonstration of 200-G coherent PON at O-band with heterogeneously-integrated SiP Tx and Rx with lasers," in *Optical Fiber Communication Conference*, pp. Th4C–1, Optica Publishing Group, 2024.

[19] S. Misak, A. Wissing, J. Zhang, Z. Wei, J. Liu, H. Andrade, A. Maharry, G. Gilardi, R. Kumar, G.-L. Su, A. Liu, Y. Akulova, J. F. Buckwalter, A. A. M. Saleh, L. Coldren, D. V. Plant, and C. L. Schow, "400 Gbps/λ DP-16QAM O-band link with SiP TX and RX PICs using only heterogeneously integrated lasers and SOAs for optical gain," in *Optical Fiber Communication Conference*, pp. Th4C–5, Optica Publishing Group, 2024.

[20] C. St-Arnault, S. Bernal, E. Berikaa, Z. Wei, R. Gutierrez-Castrejon, J. Zhang, M. S. Alam, A. Nikic, B. Krueger, F. Pittala, and D. V. Plant, "Net 1.6 Tbps (4x400Gbps/λ) O-Band IM/DD transmission over 2 km using uncooled DFB lasers on the LAN-WDM grid and sub-1V drive TFLN modulators," in *Optical Fiber Communication Conference*, pp. Th4C–6, Optica Publishing Group, 2024.

[21] Y. Hu, M. E. Mousa-Pasandi, R. Gutiérrez-Castrejón, M. O'Sullivan, F. Kong, B. Buscaino, J. Zhang, S. Bernal, C. St-Arnault, and D. V. Plant, "Digital vibration detection and localization using carrier laser phase noise retrieval in a conventional coherent transponder," in *Optical Fiber Communication Conference*, pp. W1B–6, Optica Publishing Group, 2024.

[22] L. Xu, W. Li, J. Zhang, D. Mao, M. S. Alam, Y. D'Mello, S. Bernal, Z. Wei, and D. V. Plant, "Broadband High-Performance 2$\times$ 2 MMI 3-dB Coupler Enabled by SWG Lateral Cladding for the Silicon-on-Insulator Platform," in *2023 Optical Fiber Communications Conference and Exhibition (OFC)*, pp. 1–3, IEEE, 2023.

[23] Z. Wei, J. Zhang, W. Li, and D. V. Plant, "TDMA Frame Design and Demonstration of Encrypted Coherent Fronthaul with Flexible and Monitored Rate," in *CLEO: Science and Innovations*, pp. SF2M–4, Optica Publishing Group, 2023.

[24] W. Li, L. Xu, Z. Wei, D. Mao, J. Zhang, Y. D'Mello, and D. V. Plant, "2× 2 Broadband Thermo-optic Polarization-insensitive Switch on the SOI Platform," in *CLEO: Science and Innovations*, pp. STu3J–5, Optica Publishing Group, 2023.

[25] Y. Hu, X. Li, D. Mao, M. S. Alam, E. Berikaa, J. Zhang, A. Samani, M. E. Mousa-Pasandi, M. O'Sullivan, C. Laperle, *et al.*, "Transmission of Net 200 Gbps/λ over 40 km of SMF Using an Integrated SiP Phase-Diverse Receiver," in *European Conference and Exhibition on Optical Communication*, pp. Th3B–6, Optica Publishing Group, 2022.

[26] L. Xu, D. Mao, J. Zhang, Y. Wang, Z. Xing, M. S. Alam, M. Jacques, Y. D'Mello, S. Bernal, and D. V. Plant, "Broadband polarization beam splitters based on mmi couplers with internal photonic crystals fabricated using 193 nm photolithography," in *2021 Optical Fiber Communications Conference and Exhibition (OFC)*, pp. 1–3, IEEE, 2021.

[27] D. Mao, Y. Wang, L. Xu, E. El-Fiky, M. Jacques, J. Zhang, Y. D'Mello, S. Lessard, and D. V. Plant, "Nonlinearly tapered 3-dB adiabatic coupler," in *2020 IEEE Photonics Conference (IPC)*, pp. 1–2, IEEE, 2020.

[28] L. Xu, Y. Wang, D. Mao, J. Zhang, M. S. Alam, Z. Xing, M. Jacques, Y. D'Mello, S. Bernal, S. Lessard, *et al.*, "Broadband 2× 2 adiabatic 3-dB coupler with inversely-tapered mode-evolution region for the silicon-on-insulator platform," in *2020 IEEE Photonics Conference (IPC)*, pp. 1–2, IEEE, 2020.

[29] I. Redpath, “Open optical networks - a practical guide for open line adoption for csps,” white paper, Omdia, https://www.cisco.com/c/dam/en/us/products/collateral/optical-networking/white-paper-sp-open-optical-networks.pdf, November 2022.

[30] “Silicon photonics in pluggable optics,” white paper, Cisco, https://www.cisco.com/c/en/us/products/collateral/interfaces-modules/transceiver-modules/silicon-photonics-wp.html, December 2021.

[31] S. Y. Siew, B. Li, F. Gao, H. Y. Zheng, W. Zhang, P. Guo, S. W. Xie, A. Song, B. Dong, L. W. Luo, *et al.*, “Review of silicon photonics technology and platform development,” *Journal of Lightwave Technology*, vol. 39, no. 13, pp. 4374–4389, 2021.

[32] “De-cix annual report 2021,” tech. rep., DE-CIX Group AG, June 2022.

[33] D. Thomson, A. Zilkie, J. E. Bowers, T. Komljenovic, G. T. Reed, L. Vivien, D. Marris-Morini, E. Cassan, L. Virot, J.-M. Fédéli, *et al.*, “Roadmap on silicon photonics,” *Journal of Optics*, vol. 18, no. 7, p. 073003, 2016.

[34] C. Dhote, A. Singh, and S. Kumar, “Silicon photonics sensors for biophotonic applications—a review,” *IEEE Sensors Journal*, vol. 22, no. 19, pp. 18228–18239, 2022.

[35] H. Hashemi, “A review of silicon photonics lidar,” in *2022 IEEE Custom Integrated Circuits Conference (CICC)*, pp. 1–8, IEEE, 2022.

[36] B. Wu, Y. Yu, J. Xiong, and X. Zhang, “Silicon integrated interferometric optical gyroscope,” *Scientific Reports*, vol. 8, no. 1, p. 8766, 2018.

[37] H. Li, “Refractive index of silicon and germanium and its wavelength and temperature derivatives,” *Journal of Physical and Chemical Reference Data*, vol. 9, no. 3, pp. 561–658, 1980.

[38] I. H. Malitson, “Interspecimen comparison of the refractive index of fused silica,” *Josa*, vol. 55, no. 10, pp. 1205–1209, 1965.

[39] H. Fukuda, K. Yamada, T. Tsuchizawa, T. Watanabe, H. Shinojima, and S.-i. Itabashi, “Ultrasmall polarization splitter based on silicon wire waveguides,” *Optics Express*, vol. 14, no. 25, pp. 12401–12408, 2006.

[40] D. Dai, Z. Wang, and J. E. Bowers, “Ultrashort broadband polarization beam splitter based on an asymmetrical directional coupler,” *Optics Letters*, vol. 36, no. 13, pp. 2590–2592, 2011.

[41] D. Dai and J. E. Bowers, “Novel ultra-short and ultra-broadband polarization beam splitter based on a bent directional coupler,” *Optics Express*, vol. 19, no. 19, pp. 18614–18620, 2011.

[42] H. Xu and Y. Shi, “On-chip silicon te-pass polarizer based on asymmetrical directional couplers,” *IEEE Photonics Technology Letters*, vol. 29, no. 11, pp. 861–864, 2017.

[43] L. B. Soldano and E. C. M. Pennings, “Optical multi-mode interference devices based on self-imaging: principles and applications,” *Journal of Lightwave Technology*, vol. 13, no. 4, pp. 615–627, 1995.

[44] Q. Yi, G. Cheng, Z. Yan, Q. Li, F. Xu, Y. Zou, T. Li, Y. Sun, Y. Zou, Y. Yu, *et al.*, “Silicon MMI-based power splitter for multi-band operation at the 1.55 and 2 μm wave bands,” *Optics Letters*, vol. 48, no. 5, pp. 1335–1338, 2023.

[45] M. Yin, W. Yang, Y. Li, X. Wang, and H. Li, “CMOS-compatible and fabrication-tolerant MMI-based polarization beam splitter,” *Optics Communications*, vol. 335, pp. 48–52, 2015.

[46] J. Xiao, X. Liu, and X. Sun, “Design of an ultracompact MMI wavelength demultiplexer in slot waveguide structures,” *Optics Express*, vol. 15, no. 13, pp. 8300–8308, 2007.

[47] R. Halir, G. Roelkens, A. Ortega-Moñux, and J. Wangüemert-Pérez, "High-performance 90 hybrid based on a silicon-on-insulator multimode interference coupler," *Optics Letters*, vol. 36, no. 2, pp. 178–180, 2011.

[48] D. Patel, S. Ghosh, M. Chagnon, A. Samani, V. Veerasubramanian, M. Osman, and D. V. Plant, "Design, analysis, and transmission system performance of a 41 GHz silicon photonic modulator," *Optics Express*, vol. 23, no. 11, pp. 14263–14287, 2015.

[49] E. Berikaa, M. S. Alam, A. Samani, E. El-Fiky, Y. Hu, S. Lessard, and D. V. Plant, "Silicon photonic single-segment IQ modulator for net 1 Tbps/λ transmission using all-electronic equalization," *Journal of Lightwave Technology*, 2022.

[50] L. Zhang, Y. Li, J.-Y. Yang, M. Song, R. G. Beausoleil, and A. E. Willner, "Silicon-based microring resonator modulators for intensity modulation," *IEEE Journal of Selected Topics in Quantum Electronics*, vol. 16, no. 1, pp. 149–158, 2009.

[51] Z. Zheng, A. Geravand, S. Levasseur, L. A. Rusch, and W. Shi, "Silicon microring modulator achieving 1 tb/s net rate with coherent detection," in *49th European Conference on Optical Communications (ECOC 2023)*, vol. 2023, pp. 1714–1717, IET, 2023.

[52] G. Chen, Y. Yu, Y. Shi, N. Li, W. Luo, L. Cao, A. J. Danner, A.-Q. Liu, and X. Zhang, "High-speed photodetectors on silicon photonics platform for optical interconnect," *Laser & Photonics Reviews*, vol. 16, no. 12, p. 2200117, 2022.

[53] S. J. Savory, "Digital coherent optical receivers: Algorithms and subsystems," *IEEE Journal of selected topics in quantum electronics*, vol. 16, no. 5, pp. 1164–1179, 2010.

[54] J. Xiao, X. Liu, and X. Sun, "Design of an ultracompact MMI wavelength demultiplexer in slot waveguide structures," *Optics Express*, vol. 15, no. 13, pp. 8300–8308, 2007.

[55] Y. Shi, S. Anand, and S. He, “A polarization-insensitive 1310/1550-nm demultiplexer based on sandwiched multimode interference waveguides,” *IEEE Photonics Technology Letters*, vol. 19, no. 22, pp. 1789–1791, 2007.

[56] J. Chen, P. Liu, and Y. Shi, “An on-chip silicon compact triplexer based on cascaded tilted multimode interference couplers,” *Optics Communications*, vol. 410, pp. 483–487, 2018.

[57] Y. Shi, S. Anand, and S. He, “Design of a polarization insensitive triplexer using directional couplers based on submicron silicon rib waveguides,” *Journal of Lightwave Technology*, vol. 27, no. 11, pp. 1443–1447, 2009.

[58] H. Xu and Y. Shi, “On-chip silicon triplexer based on asymmetrical directional couplers,” *IEEE Photonics Technology Letters*, vol. 29, no. 15, pp. 1265–1268, 2017.

[59] J. Chen, “A broadband wavelength demultiplexer assisted by SWG-based directional couplers,” *Optik*, vol. 202, p. 163602, 2020.

[60] G. Roelkens, D. Van Thourhout, and R. Baets, “Silicon-on-insulator ultra-compact duplexer based on a diffractive grating structure,” *Optics Express*, vol. 15, no. 16, pp. 10091–10096, 2007.

[61] C. R. Doerr, L. Chen, M. S. Rasras, Y.-K. Chen, J. S. Weiner, and M. P. Earnshaw, “Diplexer With Integrated Filters and Photodetector in Ge–Si Using $\Gamma - X$ and $\Gamma - M$ Directions in a Grating Coupler,” *IEEE Photonics Technology Letters*, vol. 21, no. 22, pp. 1698–1700, 2009.

[62] A. Y. Piggott, J. Lu, T. M. Babinec, K. G. Lagoudakis, J. Petykiewicz, and J. Vučković, “Inverse design and implementation of a wavelength demultiplexing grating coupler,” *Scientific Reports*, vol. 4, p. 7210, 2014.

[63] A. Y. Piggott, J. Lu, K. G. Lagoudakis, J. Petykiewicz, T. M. Babinec, and J. Vučković, "Inverse design and demonstration of a compact and broadband on-chip wavelength demultiplexer," *Nature Photonics*, vol. 9, no. 6, pp. 374–377, 2015.

[64] Y. Ma, P. Magill, T. Baehr-Jones, and M. Hochberg, "Design and optimization of a novel silicon-on-insulator wavelength diplexer," *Optics Express*, vol. 22, no. 18, pp. 21521–21528, 2014.

[65] J. Chen, Y. Zhang, and Y. Shi, "An on-chip triplexer based on silicon Bragg grating-assisted multimode interference couplers," *IEEE Photonics Technology Letters*, vol. 29, no. 1, pp. 63–65, 2016.

[66] L. Xu, Y. Wang, D. Mao, E. El-Fiky, Z. Xing, A. Kumar, M. G. Saber, M. Jacques, and D. V. Plant, "Broadband 1310/1550 nm wavelength demultiplexer based on a multimode interference coupler with tapered internal photonic crystal for the silicon-on-insulator platform," *Optics Letters*, vol. 44, no. 7, pp. 1770–1773, 2019.

[67] L. Liu, Q. Deng, and Z. Zhou, "An ultra-compact wavelength diplexer engineered by subwavelength grating," *IEEE Photonics Technology Letters*, vol. 29, no. 22, pp. 1927–1930, 2017.

[68] R. Halir, P. J. Bock, P. Cheben, A. Ortega-Moñux, C. Alonso-Ramos, J. H. Schmid, J. Lapointe, D. Xu, J. G. Wangüemert-Pérez, and Í. Molina-Fernández, "Waveguide sub-wavelength structures: a review of principles and applications," *Laser & Photonics Reviews*, vol. 9, no. 1, pp. 25–49, 2015.

[69] L. Xu, Y. Wang, A. Kumar, E. El-Fiky, D. Mao, H. Tamazin, M. Jacques, Z. Xing, M. G. Saber, and D. V. Plant, "Compact high-performance adiabatic 3-dB coupler enabled by subwavelength grating slot in the silicon-on-insulator platform," *Optics Express*, vol. 26, no. 23, pp. 29873–29885, 2018.

[70] V. Donzella, A. Sherwali, J. Flueckiger, S. M. Grist, S. T. Fard, and L. Chrostowski, "Design and fabrication of SOI micro-ring resonators based on sub-wavelength grating waveguides," *Optics Express*, vol. 23, no. 4, pp. 4791–4803, 2015.

[71] L. Xu, Y. Wang, A. Kumar, D. Patel, E. El-Fiky, Z. Xing, R. Li, and D. V. Plant, "Polarization beam splitter based on MMI coupler with SWG birefringence engineering on SOI," *IEEE Photonics Technology Letters*, vol. 30, no. 4, pp. 403–406, 2018.

[72] P. J. Bock, P. Cheben, J. H. Schmid, J. Lapointe, A. Delâge, D.-X. Xu, S. Janz, A. Densmore, and T. J. Hall, "Subwavelength grating crossings for silicon wire waveguides," *Optics Express*, 2010.

[73] F. Wang, X. Xu, C. Sun, and J. Zhao, "Ultracompact 1310/1550 nm wavelength demultiplexer based on subwavelength grating-assisted multimode interference coupler," *Optical Engineering*, vol. 60, no. 8, p. 087104, 2021.

[74] M. Bachmann, P. A. Besse, and H. Melchior, "General self-imaging properties in n× n multimode interference couplers including phase relations," *Applied optics*, vol. 33, no. 18, pp. 3905–3911, 1994.

[75] B.-K. Yang, S.-Y. Shin, and D. Zhang, "Ultrashort polarization splitter using two-mode interference in silicon photonic wires," *IEEE Photonics Technology Letters*, vol. 21, no. 7, pp. 432–434, 2009.

[76] S.M.Rytov, "Electromagnetic Properties of a Finely Stratified Medium," *Soviet Physics JETP*, vol. 2, no. 3, pp. 466–475, 1956.

[77] Y. Wang, W. Shi, X. Wang, Z. Lu, M. Caverley, R. Bojko, L. Chrostowski, and N. A. F. Jaeger, "Design of broadband subwavelength grating couplers with low back reflection," *Optics Letters*, vol. 40, no. 20, pp. 4647–4650, 2015.

[78] Y. Wang, L. Xu, A. Kumar, Y. D'mello, D. Patel, Z. Xing, R. Li, M. G. Saber, E. El-Fiky, and D. V. Plant, "Compact single-etched sub-wavelength grating couplers for O-band application," *Optics Express*, vol. 25, no. 24, pp. 30582–30590, 2017.

[79] D. Dai, "Silicon polarization beam splitter based on an asymmetrical evanescent coupling system with three optical waveguides," *Journal of Lightwave Technology*, vol. 30, no. 20, pp. 3281–3287, 2012.

[80] Y. Zhang, Y. He, J. Wu, X. Jiang, R. Liu, C. Qiu, X. Jiang, J. Yang, C. Tremblay, and Y. Su, "High-extinction-ratio silicon polarization beam splitter with tolerance to waveguide width and coupling length variations," *Optics Express*, vol. 24, no. 6, pp. 6586–6593, 2016.

[81] H. Xu, D. Dai, and Y. Shi, "Ultra-broadband and ultra-compact on-chip silicon polarization beam splitter by using hetero-anisotropic metamaterials," *Laser & Photonics Reviews*, vol. 13, no. 4, p. 1800349, 2019.

[82] J. R. Ong, T. Y. Ang, E. Sahin, B. Pawlina, G. Chen, D. Tan, S. T. Lim, and C. E. Png, "Broadband silicon polarization beam splitter with a high extinction ratio using a triple-bent-waveguide directional coupler," *Optics Letters*, vol. 42, no. 21, pp. 4450–4453, 2017.

[83] Z. Lu, Y. Wang, F. Zhang, N. A. Jaeger, and L. Chrostowski, "Wideband silicon photonic polarization beamsplitter based on point-symmetric cascaded broadband couplers," *Optics Express*, vol. 23, no. 23, pp. 29413–29422, 2015.

[84] Y. Tian, J. Qiu, C. Liu, S. Tian, Z. Huang, and J. Wu, "Compact polarization beam splitter with a high extinction ratio over S+C+L band," *Optics Express*, vol. 27, no. 2, pp. 999–1009, 2019.

[85] L. Xu, Y. Wang, A. Kumar, D. Patel, E. El-Fiky, Z. Xing, R. Li, and D. V. Plant, "Polarization beam splitter based on MMI coupler with SWG birefringence engineering on SOI," *IEEE Photonics Technology Letters*, vol. 30, no. 4, pp. 403–406, 2018.

[86] Y. D'Mello, E. El-Fiky, J. Skoric, A. Kumar, M. Hui, Y. Wang, L. Guenin, D. Patel, and D. V. Plant, "Compact, angled polarization splitter: Characterization of broadband performance and fabrication tolerance," *IEEE Photonics Journal*, vol. 10, no. 6, pp. 1–12, 2018.

[87] H. Xu and Y. Shi, "Ultra-broadband silicon polarization splitter-rotator based on the multi-mode waveguide," *Optics Express*, vol. 25, no. 15, pp. 18485–18491, 2017.

[88] D. Dai and J. E. Bowers, "Novel concept for ultracompact polarization splitter-rotator based on silicon nanowires," *Optics Express*, vol. 19, no. 11, pp. 10940–10949, 2011.

[89] Y. Zhang, Y. He, X. Jiang, B. Liu, C. Qiu, Y. Su, and R. A. Soref, "Ultra-compact and highly efficient silicon polarization splitter and rotator," *Apl Photonics*, vol. 1, no. 9, p. 091304, 2016.

[90] Y. Xu and J. Xiao, "Design of a compact and integrated TM-rotated/TE-through polarization beam splitter for silicon-based slot waveguides," *Applied Optics*, vol. 55, no. 3, pp. 611–618, 2016.

[91] Y. Xu and J. Xiao, "Ultracompact and high efficient silicon-based polarization splitter-rotator using a partially-etched subwavelength grating coupler," *Scientific reports*, vol. 6, no. 1, pp. 1–11, 2016.

[92] D. Guo and T. Chu, "Broadband and low-crosstalk polarization splitter-rotator with optimized tapers," *OSA Continuum*, vol. 1, no. 3, pp. 841–850, 2018.

[93] M. Ma, A. H. Park, Y. Wang, H. Shoman, F. Zhang, N. A. Jaeger, and L. Chrostowski, "Sub-wavelength grating-assisted polarization splitter-rotators for silicon-on-insulator platforms," *Optics Express*, vol. 27, no. 13, pp. 17581–17591, 2019.

[94] N. Abadía, M. G. Saber, F. Bello, A. Samani, E. El-Fiky, Y. Wang, J. F. Donegan, and D. V. Plant, "CMOS-compatible multi-band plasmonic TE-pass polarizer," *Optics Express*, vol. 26, no. 23, pp. 30292–30304, 2018.

[95] T. K. Ng, M. Z. M. Khan, A. Al-Jabr, and B. S. Ooi, "Analysis of CMOS compatible Cu-based TM-pass optical polarizer," *IEEE Photonics Technology Letters*, vol. 24, no. 9, pp. 724–726, 2012.

[96] B. Bai, L. Pei, J. Zheng, T. Ning, and J. Li, "Compact and high extinction ratio TM-pass polarizer utilizing hollow hybrid plasmonic waveguide," *Optics Communications*, vol. 445, pp. 182–186, 2019.

[97] B. Wang, S. Blaize, and R. Salas-Montiel, "Nanoscale plasmonic TM-pass polarizer integrated on silicon photonics," *Nanoscale*, vol. 11, no. 43, pp. 20685–20692, 2019.

[98] W. Hao, J. Wang, and L. Chen, "Plasmonic metasurfaces enabled ultra-compact broadband waveguide TM-Pass polarizer," *Annalen der Physik*, vol. 533, no. 1, p. 2000422, 2021.

[99] M. G. Saber, N. Abadía, and D. V. Plant, "CMOS compatible all-silicon TM pass polarizer based on highly doped silicon waveguide," *Optics Express*, vol. 26, no. 16, pp. 20878–20887, 2018.

[100] M. G. Saber, D. V. Plant, and N. Abadía, "Broadband all-silicon hybrid plasmonic TM-pass polarizer using bend waveguides," *AIP Advances*, vol. 11, no. 4, p. 45219, 2021.

[101] X. Guan, P. Chen, S. Chen, P. Xu, Y. Shi, and D. Dai, “Low-loss ultracompact transverse-magnetic-pass polarizer with a silicon subwavelength grating waveguide,” *Optics Letters*, vol. 39, no. 15, pp. 4514–4517, 2014.

[102] Y. Xiong, D.-X. Xu, J. H. Schmid, P. Cheben, and N. Y. Winnie, “High extinction ratio and broadband silicon TE-pass polarizer using subwavelength grating index engineering,” *IEEE Photonics Journal*, vol. 7, no. 5, pp. 1–7, 2015.

[103] H. Zafar, M. Odeh, A. Khilo, and M. S. Dahlem, “Low-loss broadband silicon TM-pass polarizer based on periodically structured waveguides,” *IEEE Photonics Technology Letters*, vol. 32, no. 17, pp. 1029–1032, 2020.

[104] D. W. Kim, M. H. Lee, Y. Kim, and K. H. Kim, “Ultracompact transverse magnetic mode-pass filter based on one-dimensional photonic crystals with subwavelength structures,” *Optics Express*, vol. 24, no. 19, pp. 21560–21565, 2016.

[105] Y. He, Y. Zhang, R. Zhang, L. Sun, and Y. Su, “Ultra-compact silicon TM-pass polarizer with a photonic crystal nanobeam structure,” in *Optical Fiber Communication Conference*, pp. W2A–8, Optical Society of America, 2020.

[106] N. L. Kazanskiy and M. A. Butt, “One-dimensional photonic crystal waveguide based on SOI platform for transverse magnetic polarization-maintaining devices,” *Photonics Letters of Poland*, vol. 12, no. 3, pp. 85–87, 2020.

[107] C. Prakash and M. Sen, “Optimization of silicon-photonic crystal (PhC) waveguide for a compact and high extinction ratio TM-pass polarization filter,” *Journal of Applied Physics*, vol. 127, no. 2, p. 23101, 2020.

[108] Y. D’Mello, O. Reshef, S. Bernal, E. El-fiky, Y. Wang, M. Jacques, and D. V. Plant, “Integration of periodic, sub-wavelength structures in silicon-on-insulator photonic device design,” *IET Optoelectronics*, vol. 14, no. 3, pp. 125–135, 2020.

[109] H. Xu, D. Dai, and Y. Shi, "Anisotropic metamaterial-assisted all-silicon polarizer with 415-nm bandwidth," *Photonics Research*, vol. 7, no. 12, pp. 1432–1439, 2019.

[110] W. Liu, D. Dai, and Y. Shi, "High-performance all-silicon polarizer with 415 nm bandwidth," *Optics Letters*, vol. 46, no. 6, pp. 1321–1324, 2021.

[111] Y. Wang and Y. Lu, "Broadband. High-Extinction-Ratio, and Low-Excess-Loss Polarizer Based on Horizontal Slot Silicon Bragg Grating," in *2019 24th OptoElectronics and Communications Conference (OECC) and 2019 International Conference on Photonics in Switching and Computing (PSC)*, pp. 1–3, IEEE, 2019.

[112] W. Zhou, Y. Tong, X. Sun, and H. K. Tsang, "Ultra-broadband hyperuniform disordered silicon photonic polarizers," *IEEE Journal of Selected Topics in Quantum Electronics*, vol. 26, no. 2, pp. 1–9, 2019.

[113] W. Liu, D. Dai, and Y. Shi, "All-silicon on-chip polarizer with $>$ 415 nm working bandwidth," in *2021 19th International Conference on Optical Communications and Networks (ICOCN)*, pp. 1–2, IEEE, 2021.

[114] Y. Wang, X. Wang, J. Flueckiger, H. Yun, W. Shi, R. Bojko, N. A. Jaeger, and L. Chrostowski, "Focusing sub-wavelength grating couplers with low back reflections for rapid prototyping of silicon photonic circuits," *Optics Express*, vol. 22, no. 17, pp. 20652–20662, 2014.

[115] Y. Wang, W. Shi, X. Wang, Z. Lu, M. Caverley, R. Bojko, L. Chrostowski, and N. A. Jaeger, "Design of broadband subwavelength grating couplers with low back reflection," *Optics Letters*, vol. 40, no. 20, pp. 4647–4650, 2015.

[116] Y. Wang, L. Xu, A. Kumar, Y. D'mello, D. Patel, Z. Xing, R. Li, M. G. Saber, E. El-Fiky, and D. V. Plant, "Compact single-etched sub-wavelength grating couplers for O-band application," *Optics Express*, vol. 25, no. 24, pp. 30582–30590, 2017.

[117] L. Chen and Y.-k. Chen, “Compact, low-loss and low-power 8×8 broadband silicon optical switch,” *Optics Express*, vol. 20, no. 17, p. 18977, 2012.

[118] L. Qiao, W. Tang, and T. Chu, “32 × 32 Silicon Electro-Optic Switch With Built-in Monitors and Balanced-Status Units,” *Scientific Reports*, vol. 7, no. 1, pp. 1–7, 2017.

[119] R. Ji, L. Yang, L. Zhang, Y. Tian, J. Ding, H. Chen, Y. Lu, P. Zhou, and W. Zhu, “Five-port optical router for photonic networks-on-chip,” *Optics Express*, vol. 19, no. 21, p. 20258, 2011.

[120] G. Fan, R. Orobtchouk, B. Han, J. M. Fedelin, X. Liu, and Z. Zhen, “The basic building block of λ-router with multimode-interference waveguide crossings on silicon-on-insulator technology,” *Journal of Lightwave Technology*, vol. 30, no. 16, pp. 2633–2636, 2012.

[121] R. Sun, M. Beals, A. Pomerene, J. Cheng, C.-y. Hong, L. Kimerling, and J. Michel, “Impedance matching vertical optical waveguide couplers for dense high index contrast circuits,” *Optics Express*, vol. 16, no. 16, p. 11682, 2008.

[122] A. Tsarev, “Silicon wire waveguide crossing with negligible loss and crosstalk,” *2012 11th International Conference on Actual Problems of Electronic Instrument Engineering, APEIE 2012 - Proceedings*, vol. 19, no. 15, pp. 48–50, 2012.

[123] A. M. Jones, C. T. DeRose, A. L. Lentine, D. C. Trotter, A. L. Starbuck, and R. A. Norwood, “Ultra-low crosstalk, CMOS compatible waveguide crossings for densely integrated photonic interconnection networks,” *Optics Express*, vol. 21, no. 10, p. 12002, 2013.

[124] H. Chen and A. W. Poon, “Low-loss multimode-interference-based crossings for silicon wire waveguides,” *IEEE Photonics Technology Letters*, vol. 18, no. 21, pp. 2260–2262, 2006.

[125] Y. Xu, J. Wang, J. Xiao, and X. Sun, "Design of a compact silicon-based slot–waveguide crossing," *Applied Optics*, vol. 52, no. 16, pp. 3737–3744, 2013.

[126] J. Chen and Y. Shi, "Polarization-insensitive silicon waveguide crossing based on multimode interference couplers," *Optics Letters*, vol. 43, no. 24, p. 5961, 2018.

[127] Y. Zhang, S. Yang, A. E. J. Lim, G. Q. Lo, C. Galland, T. Baehr-Jones, and M. Hochberg, "A CMOS-compatible, low-loss, and low-crosstalk silicon waveguide crossing," *IEEE Photonics Technology Letters*, vol. 25, no. 5, pp. 422–425, 2013.

[128] Y. Ma, Y. Zhang, S. Yang, A. Novack, R. Ding, A. E.-J. Lim, G.-Q. Lo, T. Baehr-Jones, and M. Hochberg, "Ultralow loss single layer submicron silicon waveguide crossing for SOI optical interconnect," *Optics Express*, vol. 21, no. 24, p. 29374, 2013.

[129] G. B. Hoffman, C. Dallo, A. Starbuck, D. Hood, A. Pomerene, D. Trotter, and C. T. DeRose, "Improved broadband performance of an adjoint shape optimized waveguide crossing using a Levenberg-Marquardt update," *Optics Express*, vol. 27, no. 17, p. 24765, 2019.

[130] P. Dumais, D. Goodwill, D. Celo, J. Jiang, and E. Bernier, "Three-mode synthesis of slab gaussian beam in ultra-low-loss in-plane nanophotonic silicon waveguide crossing," in *2017 IEEE 14th International Conference on Group IV Photonics (GFP)*, pp. 97–98, IEEE, 2017.

[131] L. Han, X. Ruan, W. Tang, and T. Chu, "Ultralow-loss waveguide crossing for photonic integrated circuits by using inverted tapers," *Optics Express*, vol. 30, no. 5, pp. 6738–6745, 2022.

[132] H. Xu, D. Dai, and Y. Shi, "Ultra-Broadband and Ultra-Compact On-Chip Silicon Polarization Beam Splitter by Using Hetero-Anisotropic Metamaterials," *Laser and Photonics Reviews*, vol. 13, no. 4, p. 1800349, 2019.

[133] H. Zafar, Y. Zhai, J. E. Villegas, F. Ravaux, K. L. Kennedy, M. F. Pereira, M. Rasras, A. Shamim, and D. H. Anjum, “Compact broadband (O, E, S, C, L & U bands) silicon TE-pass polarizer based on ridge waveguide adiabatic S-bends,” *Optics Express*, vol. 30, no. 6, pp. 10087–10095, 2022.

[134] H. Xu and Y. Shi, “Subwavelength-grating-assisted silicon polarization rotator covering all optical communication bands,” *Optics Express*, vol. 27, no. 4, p. 5588, 2019.

[135] Y. Zhang, X. Hu, D. Chen, L. Wang, M. Li, P. Feng, X. Xiao, and S. Yu, “Ultra-broadband, Low Loss and Ultra-Compact 3dB Power Splitter Based on Y-Branch with Step Waveguide,” in *OECC/PSC 2019 - 24th OptoElectronics and Communications Conference/International Conference Photonics in Switching and Computing 2019*, pp. 1–3, IEEE, 2019.

[136] X. Guo, Z. Wang, Y. Zhang, Y. Liu, Z. Zhang, J. Xu, S. Xiao, Q. Song, and K. Xu, “Ultra-broadband multimode waveguide crossing via subwavelength transmitarray with bound state,” *Laser & Photonics Reviews*, p. 2200674, 2023.

[137] W. Bogaerts, P. Dumon, D. V. Thourhout, and R. Baets, “Low-loss, low-cross-talk crossings for silicon-on-insulator nanophotonic waveguides,” *Optics Letters*, vol. 32, no. 19, p. 2801, 2007.

[138] P. J. Bock, P. Cheben, J. H. Schmid, J. Lapointe, A. Delâge, S. Janz, G. C. Aers, D.-X. Xu, A. Densmore, and T. J. Hall, “Subwavelength grating periodic structures in silicon-on-insulator: a new type of microphotonic waveguide,” *Optics Express*, vol. 18, no. 19, pp. 20251–20262, 2010.

[139] R. Halir, A. Ortega-Monux, D. Benedikovic, G. Z. Mashanovich, J. G. Wangüemert-Pérez, J. H. Schmid, I. Molina-Fernandez, and P. Cheben, “Subwavelength-grating

metamaterial structures for silicon photonic devices," *Proceedings of the IEEE*, vol. 106, no. 12, pp. 2144–2157, 2018.

[140] L. Sun, Y. Zhang, Y. He, H. Wang, and Y. Su, "Subwavelength structured silicon waveguides and photonic devices," *Nanophotonics*, vol. 9, no. 6, pp. 1321–1340, 2020.

[141] Y. Meng, Y. Chen, L. Lu, Y. Ding, A. Cusano, J. A. Fan, Q. Hu, K. Wang, Z. Xie, Z. Liu, *et al.*, "Optical meta-waveguides for integrated photonics and beyond," *Light: Science & Applications*, vol. 10, no. 1, p. 235, 2021.

[142] J. Flueckiger, S. Schmidt, V. Donzella, A. Sherwali, D. M. Ratner, L. Chrostowski, and K. C. Cheung, "Sub-wavelength grating for enhanced ring resonator biosensor," *Optics Express*, vol. 24, no. 14, pp. 15672–15686, 2016.

[143] W. Liu, Y. Ma, Y. Chang, B. Dong, J. Wei, Z. Ren, and C. Lee, "Suspended silicon waveguide platform with subwavelength grating metamaterial cladding for long-wave infrared sensing applications," *Nanophotonics*, vol. 10, no. 7, pp. 1861–1870, 2021.

[144] W. Liu, Y. Ma, X. Liu, J. Zhou, C. Xu, B. Dong, and C. Lee, "Larger-than-unity external optical field confinement enabled by metamaterial-assisted comb waveguide for ultrasensitive long-wave infrared gas spectroscopy," *Nano Letters*, vol. 22, no. 15, pp. 6112–6120, 2022.

[145] J. Zhou, Z. Zhang, B. Dong, Z. Ren, W. Liu, and C. Lee, "Midinfrared spectroscopic analysis of aqueous mixtures using artificial-intelligence-enhanced metamaterial waveguide sensing platform," *ACS nano*, vol. 17, no. 1, pp. 711–724, 2022.

[146] Y. Zhang, A. Hosseini, X. Xu, D. Kwong, and R. T. Chen, "Ultralow-loss silicon waveguide crossing using Bloch modes in index-engineered cascaded multimode-interference couplers," *Optics Letters*, vol. 38, no. 18, p. 3608, 2013.

[147] W. Zhao, X. Yi, Y. Peng, L. Zhang, H. Chen, and D. Dai, “Silicon Multimode Waveguide Crossing Based on Anisotropic Subwavelength Gratings,” *Laser and Photonics Reviews*, vol. 16, p. 2100623, mar 2022.

[148] X. Yin, T. Zhang, L. Chen, and X. Li, “Ultra-compact te-pass polarizer with graphene multilayer embedded in a silicon slot waveguide,” *Optics Letters*, vol. 40, no. 8, pp. 1733–1736, 2015.

[149] X. Yin, X. Ke, L. Chen, T. Zhang, J. Li, Z. Zhu, and X. Li, “Ultra-broadband te-pass polarizer using a cascade of multiple few-layer graphene embedded silicon waveguides,” *Journal of Lightwave Technology*, vol. 34, no. 13, pp. 3181–3187, 2016.

[150] T. Zhang, X. Ke, X. Yin, L. Chen, and X. Li, “Graphene-assisted ultra-compact polarization splitter and rotator with an extended bandwidth,” *Scientific Reports*, vol. 7, no. 1, p. 12169, 2017.

[151] Y. D’Mello, O. Reshef, S. Bernal, E. El-fiky, Y. Wang, M. Jacques, and D. V. Plant, “Integration of periodic, sub-wavelength structures in silicon-on-insulator photonic device design,” *IET Optoelectronics*, vol. 14, no. 3, pp. 125–135, 2020.

[152] C. Gu and P. Yeh, “Form birefringence dispersion in periodic layered media,” *Optics Letters*, vol. 21, no. 7, pp. 504–506, 1996.

[153] M. Qiu, Q. Zhuge, M. Chagnon, Y. Gao, X. Xu, M. Morsy-Osman, and D. V. Plant, “Digital subcarrier multiplexing for fiber nonlinearity mitigation in coherent optical communication systems,” *Optics Express*, vol. 22, no. 15, pp. 18770–18777, 2014.

[154] P. Poggiolini, A. Nespola, Y. Jiang, G. Bosco, A. Carena, L. Bertignono, S. M. Bilal, S. Abrate, and F. Forghieri, “Analytical and experimental results on system maximum reach increase through symbol rate optimization,” *Journal of Lightwave Technology*, vol. 34, no. 8, pp. 1872–1885, 2016.

[155] T. Rahman, D. Rafique, B. Spinnler, A. Napoli, M. Bohn, A. Koonen, C. M. Okonkwo, and H. De Waardt, "Digital subcarrier multiplexed hybrid qam for data-rate flexibility and roadm filtering tolerance," in *Optical Fiber Communication Conference*, pp. Tu3K–5, Optica Publishing Group, 2016.

[156] M. Xiang, Q. Zhuge, X. Zhou, M. Qiu, F. Zhang, T. M. Hoang, M. Y. Sowailem, M. Tang, D. Liu, S. Fu, *et al.*, "Filtering tolerant digital subcarrier multiplexing system with flexible bit and power loading," in *2017 Optical Fiber Communications Conference and Exhibition (OFC)*, pp. 1–3, IEEE, 2017.

[157] H. Sun, M. Torbatian, M. Karimi, R. Maher, S. Thomson, M. Tehrani, Y. Gao, A. Kumpera, G. Soliman, A. Kakkar, *et al.*, "800G DSP ASIC design using probabilistic shaping and digital sub-carrier multiplexing," *Journal of Lightwave Technology*, vol. 38, no. 17, pp. 4744–4756, 2020.

[158] D. Krause, A. Awadalla, A. S. Karar, H. Sun, and K.-T. Wu, "Design considerations for a digital subcarrier coherent optical modem," in *2017 Optical Fiber Communications Conference and Exhibition (OFC)*, pp. 1–3, IEEE, 2017.

[159] D. Che and X. Chen, "Achievable rate comparison between probabilistically-shaped single-carrier and entropy-loaded multi-carrier signaling in a bandwidth-limited 1-Tb/s coherent system," in *2021 Optical Fiber Communications Conference and Exhibition (OFC)*, pp. 1–3, IEEE, 2021.

[160] D. Welch, A. Napoli, J. Bäck, S. Buggaveeti, C. Castro, A. Chase, X. Chen, V. Dominic, T. Duthel, T. A. Eriksson, *et al.*, "Digital subcarrier multiplexing: Enabling software-configurable optical networks," *Journal of Lightwave Technology*, vol. 41, no. 4, pp. 1175–1191, 2022.

[161] L. Velasco, S. Barzegar, D. Sequeira, A. Ferrari, N. Costa, V. Curri, J. Pedro, A. Napoli, and M. Ruiz, "Autonomous and energy efficient lightpath operation based on digital subcarrier multiplexing," *IEEE Journal on Selected Areas in Communications*, vol. 39, no. 9, pp. 2864–2877, 2021.

[162] S. H. Han and J. H. Lee, "An overview of peak-to-average power ratio reduction techniques for multicarrier transmission," *IEEE wireless communications*, vol. 12, no. 2, pp. 56–65, 2005.

[163] W. Shieh and Y. Tang, "Ultrahigh-speed signal transmission over nonlinear and dispersive fiber optic channel: the multicarrier advantage," *IEEE Photonics Journal*, vol. 2, no. 3, pp. 276–283, 2010.

[164] R. Li, D. Patel, E. El-Fiky, A. Samani, Z. Xing, M. Morsy-Osman, and D. V. Plant, "High-speed low-chirp PAM-4 transmission based on push-pull silicon photonic microring modulators," *Optics Express*, vol. 25, no. 12, pp. 13222–13229, 2017.

[165] M. Li, L. Wang, X. Li, X. Xiao, and S. Yu, "Silicon intensity Mach-Zehnder modulator for single lane 100 Gb/s applications," *Photonics Research*, vol. 6, no. 2, pp. 109–116, 2018.

[166] O. Jafari, W. Shi, and S. LaRochelle, "Mach-Zehnder silicon photonic modulator assisted by phase-shifted bragg gratings," *IEEE Photonics Technology Letters*, vol. 32, no. 8, pp. 445–448, 2020.

[167] P. Gou, L. Zhao, K. Wang, W. Zhou, and J. Yu, "Nonlinear look-up table predistortion and chromatic dispersion precompensation for IM/DD PAM-4 transmission," *IEEE Photonics Journal*, vol. 9, no. 5, pp. 1–7, 2017.

[168] J. Zhang, J. Yu, and H.-C. Chien, "EML-based IM/DD 400G (4× 112.5-Gbit/s) PAM-4 over 80 km SSMF based on linear pre-equalization and nonlinear LUT pre-distortion

for inter-DCI applications," in *Optical Fiber Communication Conference*, pp. W4I–4, Optical Society of America, 2017.

[169] W. Shieh, Y. Tang, and B. S. Krongold, "DFT-spread OFDM for optical communications," in *Digest of the 9th International Conference on Optical Internet (COIN 2010)*, pp. 1–3, IEEE, 2010.

[170] Y. Tang, W. Shieh, and B. S. Krongold, "DFT-spread OFDM for fiber nonlinearity mitigation," *IEEE Photonics Technology Letters*, vol. 22, no. 16, pp. 1250–1252, 2010.

[171] F. Wang and X. Wang, "Coherent optical DFT-spread OFDM," *Advances in Optical Technologies*, vol. 2011, 2011.

[172] Q. Yang, Z. He, Z. Yang, S. Yu, X. Yi, and W. Shieh, "Coherent optical DFT-spread OFDM transmission using orthogonal band multiplexing," *Optics Express*, vol. 20, no. 3, pp. 2379–2385, 2012.

[173] C. Wu, H. Zhang, and W. Xu, "On visible light communication using LED array with DFT-spread OFDM," in *2014 IEEE International Conference on Communications (ICC)*, pp. 3325–3330, IEEE, 2014.

[174] M. Chen, X. Xiao, Z. R. Huang, J. Yu, F. Li, Q. Chen, and L. Chen, "Experimental demonstration of an IFFT/FFT size efficient DFT-spread OFDM for short reach optical transmission systems," *Journal of Lightwave Technology*, vol. 34, no. 9, pp. 2100–2105, 2016.

[175] Z.-Y. Wu, Y.-L. Gao, Z.-K. Wang, C. You, C. Yang, C. Luo, and J. Wang, "Optimized DFT-spread OFDM based visible light communications with multiple lighting sources," *Optics Express*, vol. 25, no. 22, pp. 26468–26482, 2017.

[176] E. Berikaa, M. S. Alam, A. Samani, S. Lessard, and D. V. Plant, "Net 1 Tbps/λ transmission over 80 km of SSMF using a single segment SiP IQM with all-electronic

equalization," in *Optical Fiber Communication Conference*, pp. Th4A–5, Optica Publishing Group, 2022.

[177] D. Che, Q. Hu, and W. Shieh, "Linearization of direct detection optical channels using self-coherent subsystems," *Journal of Lightwave Technology*, vol. 34, no. 2, pp. 516–524, 2016.

[178] S. Randel, D. Pilori, S. Chandrasekhar, G. Raybon, and P. Winzer, "100-gb/s discrete-multitone transmission over 80-km ssmf using single-sideband modulation with novel interference-cancellation scheme," in *2015 European Conference on Optical Communication (ECOC)*, pp. 1–3, IEEE, 2015.

[179] X. Liu, S. Chandrasekhar, and A. Leven, "Digital self-coherent detection," *Optics Express*, vol. 16, no. 2, pp. 792–803, 2008.

[180] D. Che, C. Sun, and W. Shieh, "Optical field recovery in stokes space," *Journal of Lightwave Technology*, vol. 37, no. 2, pp. 451–460, 2018.

[181] S. T. Le, K. Schuh, M. Chagnon, F. Buchali, R. Dischler, V. Aref, H. Buelow, and K. M. Engenhardt, "1.72-tb/s virtual-carrier-assisted direct-detection transmission over 200 km," *Journal of Lightwave Technology*, vol. 36, no. 6, pp. 1347–1353, 2018.

[182] A. Mecozzi, C. Antonelli, and M. Shtaif, "Kramers–kronig coherent receiver," *Optica*, vol. 3, no. 11, pp. 1220–1227, 2016.

[183] Z. Li, M. S. Erkılınç, K. Shi, E. Sillekens, L. Galdino, B. C. Thomsen, P. Bayvel, and R. I. Killey, "Ssbi mitigation and the kramers–kronig scheme in single-sideband direct-detection transmission with receiver-based electronic dispersion compensation," *Journal of Lightwave Technology*, vol. 35, no. 10, pp. 1887–1893, 2017.

[184] Z. Xing, A. Samani, M. Xiang, E. El-Fiky, T. M. Hoang, D. Patel, R. Li, M. Qiu, M. G. Saber, M. Morsy-Osman, *et al.*, "100 gb/s pam4 transmission system for datacenter

interconnects using a sip me-mzm based dac-less transmitter and a vsb self-coherent receiver," *Optics Express*, vol. 26, no. 18, pp. 23969–23979, 2018.

[185] W. Shieh, C. Sun, and H. Ji, "Carrier-assisted differential detection," *Light: Science & Applications*, vol. 9, no. 1, p. 18, 2020.

[186] H. Ji, M. Sun, C. Sun, and W. Shieh, "Carrier assisted differential detection with a generalized transfer function," *Optics Express*, vol. 28, no. 24, pp. 35946–35959, 2020.

[187] C. Sun, T. Ji, H. Ji, Z. Xu, and W. Shieh, "Experimental demonstration of complex-valued dsb signal field recovery via direct detection," *IEEE Photonics Technology Letters*, vol. 32, no. 10, pp. 585–588, 2020.

[188] X. Li, M. O'Sullivan, Z. Xing, M. S. Alam, M. E. Mousa-Pasandi, and D. V. Plant, "Asymmetric self-coherent detection," *Optics Express*, vol. 29, no. 16, pp. 25412–25427, 2021.

[189] C. R. Doerr, "Silicon photonic integration in telecommunications," *Frontiers in Physics*, vol. 3, p. 37, 2015.

[190] S. Y. Siew, B. Li, F. Gao, H. Y. Zheng, W. Zhang, P. Guo, S. W. Xie, A. Song, B. Dong, L. W. Luo, *et al.*, "Review of silicon photonics technology and platform development," *Journal of Lightwave Technology*, vol. 39, no. 13, pp. 4374–4389, 2021.

[191] J. Li, Z. Wang, H. Ji, X. Li, H. Chen, R. R. Unnithan, W. Shieh, and Y. Su, "Silicon photonic carrier-assisted differential detection receiver with high electrical spectral efficiency for short-reach interconnects," *Journal of Lightwave Technology*, vol. 41, no. 3, pp. 919–925, 2023.

[192] X. Li, M. O'Sullivan, Z. Xing, M. E. Mousa-Pasandi, and D. V. Plant, "Asymmetric self-coherent detection based on mach-zehnder interferometers," *Journal of Lightwave Technology*, vol. 40, no. 7, pp. 2023–2032, 2021.

[193] E. Dulkeith, F. Xia, L. Schares, W. M. Green, and Y. A. Vlasov, "Group index and group velocity dispersion in silicon-on-insulator photonic wires," *Optics Express*, vol. 14, no. 9, pp. 3853–3863, 2006.

[194] Y. Zhang, S. Yang, A. E.-J. Lim, G.-Q. Lo, C. Galland, T. Baehr-Jones, and M. Hochberg, "A compact and low loss y-junction for submicron silicon waveguide," *Optics Express*, vol. 21, no. 1, pp. 1310–1316, 2013.

[195] X. Wang, Y. Zeng, R. Liao, C. Zhao, H. Wu, and M. Tang, "Mach-Zehnder interferometer based endlessly adaptive polarization controller on silicon-photonic platform," in *2021 Optical Fiber Communications Conference and Exhibition (OFC)*, pp. 1–3, IEEE, 2021.

[196] J. Li, Z. Wang, H. Ji, X. Li, H. Chen, R. R. Unnithan, W. Shieh, and Y. Su, "High electrical spectral efficiency silicon photonic receiver with carrier-assisted differential detection," in *Optical Fiber Communication Conference*, pp. Th4B–6, Optica Publishing Group, 2022.

[197] Y. Tong, Q. Zhang, X. Wu, C. Shu, and H. K. Tsang, "112 Gb/s 16-QAM OFDM for 80-km data center interconnects using silicon Photonic integrated circuits and Kramers–Kronig detection," *Journal of Lightwave Technology*, vol. 37, no. 14, pp. 3532–3538, 2019.

[198] Y. Hong, K. Li, C. Lacava, S. Liu, D. J. Thomson, F. Meng, X. Ruan, F. Zhang, G. T. Reed, and P. Petropoulos, "High-speed DD transmission using a silicon receiver co-integrated with a 28-nm CMOS gain-tunable fully-differential TIA," *Journal of Lightwave Technology*, vol. 39, no. 4, pp. 1138–1147, 2020.

[199] S. Zhang, L. Lu, L. Fan, B. Chen, T. Zhang, T. Zuo, L. Liu, J. Tang, L. Zeng, P. Chen, *et al.*, "224-Gb/s 16QAM SV-DD transmission using pilot-assisted polarization

recovery with integrated receiver," in *Optical Fiber Communication Conference*, pp. W7F–4, Optica Publishing Group, 2021.